2019

Reconfigurable Reflectarray Antennas with Bandwidth Enhancement for High Gain, Beam-Steering Applications

Michael Trampler
University of Central Florida

RECONFIGURABLE REFLECTARRAY ANTENNAS WITH BANDWIDTH ENHANCEMENT FOR HIGH GAIN, BEAM-STEERING APPLICATIONS

by

MICHAEL E. TRAMPLER
B.S. University of Central Florida, 2012
M.S. University of Central Florida, 2015

A dissertation submitted in partial fulfilment of the requirements
for the degree of Doctor of Philosophy
in the Department of Electrical & Computer Engineering
in the College of Engineering and Computer Science
at the University of Central Florida
Orlando, Florida

Summer Term
2019

Major Professor: Xun Gong

ABSTRACT

Reconfigurable reflectarrays are a class of antennas that combine the advantages of traditional parabolic antennas and phased array antennas. Chapter 1 discusses the basic operational theory of reflectarrays and their design. A review of previous research and the current status is also presented. Furthermore the inherent advantages and disadvantages of the reflectarray topography are presented.

In chapter 2, a BST-integrated reflectarray operating at K_a band is presented. Due to the monolithic integration of the tuning element, this design is then extended to V band where a novel interdigital gap configuration is utilized. Finally to overcome loss and phase limitations of the single resonant design, a BST-integrated, dual-resonance unit cell operating at K_a band is designed. While the losses are still high, a 360^o phase range is demonstrated.

In chapter 3, the operational theory of dual-resonant array elements is introduced utilizing Q theory. An equivalent circuit is developed and used to demonstrate design tradeoffs. Using this theory the design procedure of a varactor tuned dual-resonant unit cell operating at X-band is presented. Detailed analysis of the design is performed by full-wave simulations and verified via measurements.

In chapter 4, the array performance of the dual-resonance unit cell is analyzed. The effects of varying angles of incidence on the array element are studied using Floquet simulations. The beam scanning, cross-polarization and bandwidth performance of a 7×7 element reflectarray is analyzed using full-wave simulations and verified via measurements.

In chapter 5 a loss analysis of the dual-resonant reflectarray element is performed. Major sources of loss are identified utilizing full-wave simulations before an equivalent circuit is utilized to optimize

the loss performance while maintaining a full phase range and improved bandwidth performance. Finally the dual-resonance unit cell is modified to support two linear polarizations.

Overall, the operational and design theory of dual resonant reflectarray unit cells using Q theory is developed. A valuable equivalent circuit is developed and used to aid in array element design as well as optimize the loss and bandwidth performance. The proposed theoretical models provide valuable physical insight through the use of Q theory to greatly aid in reflectarray design.

Dedicated to my loving parents Kurt & Lisa Trampler

ACKNOWLEDGMENTS

First and foremost I would like to thank my parents, who have always supported and motivated me. I would also like to thank my advisor, Dr. Xun Gong whose guidance and support were critical in the advancement of my understanding and the direction of my research. My research would not have been successful without the contributions from my good friends Dr. Kalyan K. Karnati, Mr. Ricardo Lovato and Dr. Wei Ouyang.

I would like to thank my committee members Dr. Parveen Wahid, Dr. Linwood Jones, Dr. Kenle Chen and Dr. Stephen Kuebler for their support and advice. During my progress as a graduate student I benefited greatly from my frequent discussions with Dr. Kalyan K. Karnati, Dr. Tianjao Lin, Dr. Mahmoud Shiraz, Mr. Ricardo Lovato, Dr. Wei Ouyang and Mr. Junyi Huang.

In addition, I would like to thank the funding support from the National Science Foundation Grants ECCS-1231976 and ECCS-1443942

TABLE OF CONTENTS

LIST OF FIGURES

LIST OF TABLES

CHAPTER 1: INTRODUCTION

1.1 Motivation

The new standards for 5G communications require very high gain antennas that support beam-scanning functionality to satiate the need for high data rates and spatial diversity in noisy environments. Furthermore, these antennas need to be inexpensive to fabricate and deploy for widespread implementation. The applications for such antennas range from terrestrial base station applications to extraterrestrial satellite communications [1], [2] and radar [3]. Traditionally, these roles would be filled by phased arrays [4] and parabolic antennas [5].

Parabolic antennas utilize a shaped metallic reflector to gather an incident plane wave and focus it into a feed antenna located at the focal point of the reflector. Thus, basic parabolic reflectors are a relatively low cost wideband, high gain antenna implementation. However, the deployment of parabolic antennas can be quite difficult especially in satellite applications. Parabolic reflectors become very bulky as they scale with size due to the specific curvature required to realize a desired radiation pattern. Additionally, they are incapable of even moderate scan angles using electrically steered beams [6]. Functional beam-scanning requires the mechanical rotation of the reflector and feed horn, greatly increasing the complexity of the mounting structure and significantly limiting the scanning speed.

Phased array antennas are typically planar and easily deployable; they can provide high speed electronic beam-scanning and beam-shaping. However, phased arrays require phase shifters in the feeding network or utilize T/R modules to enable this beam-scanning. T/R modules are costly, power hungry, and generate significant heat while phase shifters introduce high losses [7] and in the case of discrete phase shifters, quantization phase error [8].

Reflectarray antennas are viewed as a viable option for highly efficient, high gain, applications requiring beam-scanning due to the unique combination of parabolic and phased array antennas [9]–[11]. Reflectarrays, like parabolic antennas utilize quasi-optical excitation of an aperture. However, reflectarray apertures are planar and consist of multiple array elements, each capable of introducing a specific phase shift. The phase shift of each element enables the electronic steering of the beam without a lossy and costly feed network utilized in phased arrays.

1.2 Fundamentals of Reflectarray Antennas

In this section some history on the development of the reflectarray, their operating theory, and their key performance parameters will be discussed. Several reflectarray archetypes will be presented along with their advantages and disadvantages. The practical design principles of reflectarray apertures and array elements will be discussed and the state of the art technologies and designs will be presented.

1.2.1 Reflectarray Principles of Operation

The first reflectarray design was proposed by Berry, Malech, and Kennedy in 1963 [12]. The prototype utilized shorted waveguide elements of varying lengths. When illuminated by a feed horn, the energy was coupled into the waveguides and reflected by the shorts, re-radiating the energy with a phase shift corresponding to the length of the waveguide. However, the waveguides themselves were bulky and quite heavy, making the design impractical. Research into reflectarrays lulled until the introduction of microstrip antenna technology [13]. The low weight, low profile, and inexpensive fabrication of microstrip antennas made them ideal for reflectarray design. The first microstrip reflectarrays used patches of different sizes [14], cross-dipoles, rings of different resonant lengths

[15], [16], and patches loaded with stubs of varying length [17]. While these examples focused on linearly polarized designs significant work was also made to design circularly polarized reflectarrays. In [18], [19], identical square microstrip patches were individually designed to be circularly polarized using two stubs of different length. The required reflected phase was achieved by rotating the patches.

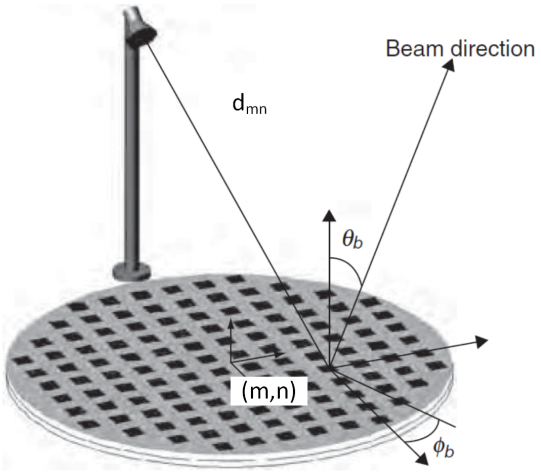

Figure 1.1: Typical Geometry of a printed reflectarray antenna. Re-printed from [20]

A schematic of an offset fed reflectarray is shown in Fig. 1.1. The reflectarray consists of an array of elements on a dielectric substrate with a ground plane. Each element (m, n) is illuminated by the offset feed horn which is separated by a distance (d_{mn}). The energy from the feed is coupled into each element and is then re-radiated with the specific phase shift required to form a plane wave in a desired direction. From array theory [4], we know that the phase shift required on a given an array aperture to point the beam to a specific direction (θ_b, ϕ_b) is calculated as 1.1 where (m, n) are the coordinates of the element and k_o is the propagation constant in a vacuum.

$$\Phi_R(m,n) = -k_o sin(\theta_b) cos(\phi_b) m - k_o sin(\theta_b) sin(\phi_b) n \tag{1.1}$$

However, in reflectarray design, each element is not fed identically and there is a phase shift be-

tween each of them that arises from the differential spatial distance of each element from the feed. The phase of the wave reflected by each element can be written as 1.2 where $\Phi_E(m,n)$ is the individual element's reflected phase.

$$\Phi_R(m,n) = -k_o d_{mm} + \Phi_E(m,n) \tag{1.2}$$

Combining 1.1 and 1.2 we can solve for the required element phase $\Phi_E(m,n)$ as 1.3.

$$\Phi_E(m,n) = k_o d(m,n) + k_o sin(\theta_b) cos(\phi_b) m - k_o sin(\theta_b) sin(\phi_b) n \tag{1.3}$$

From 1.3 it can be seen that it is necessary for each radiating element to have a phase range of 360^o or greater to prevent phase errors across the reflectarray aperture.

1.2.2 Types of Reflectarray Antennas

1.2.2.1 Passive Designs

Passive reflectarrays are not capable of beam-scanning and typically they will have very high efficiencies, low element loss, and wider bandwidths than reconfigurable designs. Array elements are designed such that some physical parameter, whether it be the length of a delay line [21] or the resonant length of a patch [14], can be varied to realize a specific reflection phase. Each element is designed around this parameter to realize the correct reflected phase from 1.3. Most passive reflectarray designs have peak element losses significantly less than 0.5 dB and overall efficiencies greater than 60%.

1.2.2.2 Reconfigurable Designs

Reconfigurable reflectarrays have garnered significant interest in recent years due to desirability of electronic beam-scanning. The most common approach to implement reconfigurability is to introduce an electronic load to the same array elements used in passive designs. By loading the array element with switched true-time delay (TTD) lines, discrete phase states can be realized [22], [23]. Alternatively continuously variable loads such as varactors or PIN diodes can be integrated into resonator-type unit cells [24]–[26]. While these unit cells are capable of quickly adjusting their phase response thus enabling beam-scanning, the tuning elements introduce significant loss and the phase range is typically limited to much less than 360^o. As such, significant work is focused on optimizing the loading mechanism and placement of these elements to minimize loss and maximize phase range.

1.2.2.3 Shaped and Multi-Beam Designs

While most passive and reconfigurable reflectarray designs radiate a single main beam, also known as a pencil beam, they can also be designed to cover a specific region. Shaped beams can be realized using phased arrays through the use of array element amplitude and phase contouring. However, in reflectarray design the magnitude of the reflected wave from each reflectarray element cannot be actively controlled. Additionally, the loss of each element will vary as the reflected phase is changed, while the intensity of the incident wave is wholly dependent on the feed horn design and placement. However, it is still possible to synthesize shaped beams using only the reflected phase. This method is based on the intersection approach [27]–[29].

Additionally, reflectarrays can also be designed for multi-beam applications with single or multiple feeds [30]. In [29], a dual-polarization reflectarray was designed with two independent beams with

orthogonal polarization; this reflectarray was used to replace a conventional reflector in a satellite application. The H-polarization formed a contour beam for specific European coverage while the V-polarization formed a pencil beam.

1.3 Reflectarray Design Challenges

1.3.1 Bandwidth Limitations

Reflectarray antennas traditionally have very small bandwidths as compared to parabolic reflector antennas. Parabolic reflectors are inherently wideband as the phase delay required to focus the beam is caused by a physical distance between the feed and the reflector. As such, when the frequency varies, the physical distance compensates for the necessary phase shifts. However, resonator based reflectarrays will experience increasing phase errors from each array element as the frequency varies from the design frequency. TTD array elements and multi-resonant elements have been used to provide linear phase responses, increasing reflectarray bandwidth performance at the cost of design and fabrication complexity.

1.3.2 Feed-Image Lobe

The feed-image lobe concept applies to reflectarrays with offset feeds. The issue occurs when energy incident on the aperture is reflected in the specular direction, as shown in Fig. 1.2. The issue of the image lobe was presented in [31] and it was hypothesized that the image lobe was due to scattering from the ground plane; the array elements are spaced widely enough such that there are large areas where the ground plane is not occluded by an array element. A triangular lattice was used to maximize the area covered by elements, however only a minimal improvement in the image lobe was observed [31]. Conversely in [32], [33] it was found that the image lobe was due

in part to phase errors from specific elements, especially those in the Fresnel zone boundaries. As will be discussed, the infinite array assumption that is used in most reflectarray designs breaks down around the Fresnel zone as the phase wraps through 360^o.

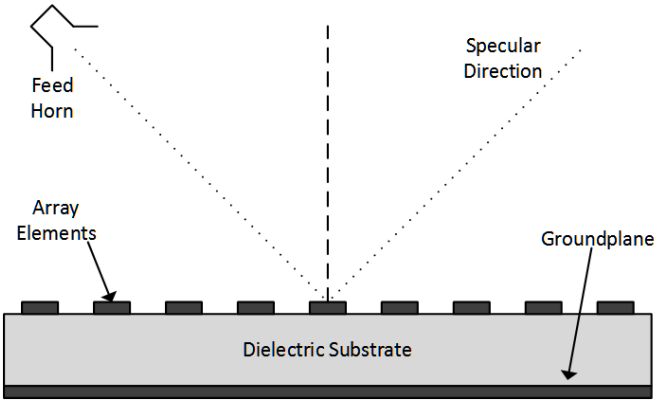

Figure 1.2: Cross-section of an offset-fed reflectarray showing the incident wave and angle of specular reflection

1.3.3 Beam Squint in Offset-Fed Reflectarrays

Beam squint describes the phenomenon where a frequency-dependent reduction in gain appears where the main beam deviates from the desired beam and is observed in offset-fed reflector and reflectarray antennas alike. The beam squint becomes more pronounced as the frequency deviates further from the center frequency. A numerical analysis was used in [34] to find the source of beam squinting in reflectarrays. It was shown that for all frequencies aside from the center frequency, the aperture phase distribution will have a slope that is different from that which is required to point the main beam in the desired direction. While a complete solution to beam squint was not proposed in [34] it was found that it could be reduced by designing the main beam in the specular direction.

1.3.4 Sources of Phase Error

The phase response of each reflectarray element is of critical importance to the operation of the array. As such any sources of phase error should be identified and carefully studied. Fabrication tolerances will have a direct and obvious effect on the performance of the array. Several resonator designs, especially those designed to maximize phase range will be more sensitive to fabrication errors. Another obvious source of error comes from a lack of phase range, single-resonance elements will typically have less than 360^o phase range; to avoid this issue true-time delay and multi-resonant elements can be used. However, if the phase range is less than 360^o the array will inevitably suffer from phase errors.

Another source of phase error comes from angle of incidence assumptions. The angle of incidence is defined as the angle between the incident wave and the normal direction of the antenna aperture. In center-fed reflectarrays this angle is 0^o at the center of the array and increases for elements closer to the edge of the array. Using an off-set feed or moving the feed close to the aperture for a smaller *f/D* will increase this angle. Typically the reflection phase of a given array element is extracted via normal incidence approximation and Floquet modes must be used to study these effects [35] in arrays with significant angles of incidence. Finally, a significant source of error comes from the use of infinite array approximations when designing and simulating passive reflectarray elements. Array elements are typically designed under the assumption that the element is in an infinite array of identical elements. In conventional reflectarrays the required phase changes gradually in each Fresnel zone. Thus, the variable dimension that is used to control the reflected phase is very similar between neighboring elements. However, when the zone is complete, the required phase changes by 360^o and the element dimension makes a step change between the maximum and minimum dimensions which breaks the periodic approximation, resulting in some error in the predicted phase response.

1.4 Feed Antenna Design and Aperture Efficiency

Reflectarray design can be broadly broken down into two categories: the design of the array element and that of the feed horn. The aperture efficiency is dependent on the radiation pattern of the feed and its position in relation to the aperture [36]. The spillover efficiency is a measure of the ratio between the energy captured by the aperture and the energy radiated by the feed. As the feed is moved closer to the aperture or as its gain is increased, the spillover efficiency increases proportionally. The illumination efficiency is a measure of how evenly excited each element on the aperture is. As the feed is moved further away from the aperture or as the feed gain is reduced, the illumination efficiency similarly increases. In general the aperture efficiency is determined by the directivity of the feed antenna and the ratio of the distance between the aperture (f) and the aperture size (D).

Another issue to consider is feed blockage which occurs when the feed horn or positioning structure obscures or interferes with the reflectarray radiation pattern. A significant issue with relatively small reflectarrays, feed blockage can be minimized by offsetting the feed at an angle to the normal vector of the aperture. If the feed horn is offset too far, the aperture efficiency will suffer, however offset angles up to 30^o can be used without significant degradation. Offsetting the feed also increases the angle of incidence seen by each array element, especially those at the edges of the array. While some elements are not sensitive to the angle of incidence, special care needs to be taken to ensure the array performance does not degrade from to unexpected phase errors due to the offset feed.

1.5 True-Time Delay Array Elements

The bandwidth of reflectarrays is limited by two key parameters [9]: the bandwidth of the antenna elements [37] and the differential spatial phase delay from the feed [38]. The bandwidth will not be limited by the differential spatial distances unless the array is very electrically large [9]. This can be compensated for by using array elements that utilize true-time delays (TTDs) to provide the phase delay [21], [39], [40]. In [40], an open-ended transmission line was placed under a microstrip patch antenna and a slot was cut in the ground plane. The incident wave would couple into the patch, through the slot, and into the transmission line. The energy would then travel the length of the transmission line, reflect from the discontinuity in the line, and couple back into the patch before being re-radiated with a phase shift; the desired phase shift is achieved by varying the length of the delay line. Due to the fact that the phase shift is caused by a physical delay, the phase shift has a linear relationship with frequency. This phase shift compensates for the electrical spacing between the elements at different frequencies. However, this technique significantly increases the fabrication complexity, and the transmission line adds additional dissipative losses. Another TTD technique was proposed in [17] using identical patches with variable-length stubs. Like the aperture coupled design, energy couples from the patch into the stubs and is reflected back to the patch after a designed delay. However, it was found that the stubs added significant dissipative losses and degraded the cross-polarization performance. From this discussion it can be seen that array elements with a smooth and mostly linear phase response will have improved bandwidth performance. It should also be noted that the coupling of the incident wave into the delay line in both of these designs has a certain bandwidth. Thus, the bandwidth of elements designed with this technique is limited.

1.6 Resonant Array Elements

Reflectarray designs based on the use of a resonant element depend on the fact that the reflected phase changes about its resonant frequency [41]. Controlling the reflection phase by altering the resonant dimension was presented in [14], [15]. When the array element is over-coupled, the phase response exhibits an S-curve. By changing the resonant frequency of the array element, the reflected phase at the reflectarray operating frequency is varied. Considering the ease of this technique when compared to the complicated design and fabrication required for aperture coupled array elements [40], resonant array element designs are very common. These reflectarray elements typically use passive tuning mechanisms and are commonly used for fixed-beam applications. The lack of active tuning mechanisms makes the fabrication of these arrays particularly inexpensive.

Several resonant structures have been used to realize functional reflectarray elements including printed dipoles of variable lengths [15] and microstrip patches of variable lengths [14]. The benefit of these techniques over the stub and aperture coupled approach is in the reduction of dissipative losses and reduced cross-polarization levels. However, this approach also limits the phase ranges achievable and introduce non-linear phase variations about the resonant frequency which limit the bandwidth performance.

To overcome the bandwidth limitations inherent in reflectarrays, multi-layer structures were proposed in [42], [43]. In both of these designs the unit cell was designed using multiple concentric resonating elements on bonded substrates. While both of these reflectarrays showed improvements in the bandwidth, they presented significant drawbacks: the reflectarrays became more bulky, the design became much more complex due to the strong mutual coupling between the resonators of each element, and the multi-layer design increased fabrication costs.

To avoid the multi-layer issues demonstrated in [42], [43], another technique was developed in

which multiple resonating elements are coupled together on the same planar surface. Square and circular-shape rings were used in [44] while in [45] cross/loop elements with variable loop lengths were used. [46] demonstrated a significant improvement in the fractional gain bandwidth performance through the use of a rectangular ring and square patch design on a single layer.

1.7 *Q* Factor Analysis Technique

The use of *Q* factors in the analysis of resonance based reflectarray unit cells was presented in [41]. In this paper a passive reflectarray's phase slope, phase range, and loss performance is evaluated through the use of quality factors. It was shown that the ratio of the radiation *Q* to the parallel combination of the conductor and dielectric *Q* factors ($Q_c//Q_d = Q_o$) will determine the loss and phase slope of the reflected wave at the resonant frequency of the element. When the radiation Q_{rad} is greater than Q_o the phase of the reflected wave around the resonant frequency is discontinuous, which isn't useful in passive reflectarray designs, and in general should be avoided in reconfigurable designs as well. When $Q_{rad} = Q_o$ all of the energy coupled into the unit cell is dissipated in the unit cell and the loss is infinite. When $Q_{rad} < Q_o$ the phase response is continuous about the resonant frequency and desirable phase shifts are achievable.

Q factor theory not only describes the phase response, it also predicts the loss of a unit cell. The closer the values of $Q_{rad}\&Q_o$ become, the greater the loss of the resonance. However, the phase slope and therefore phase range also increases as these two values become more similar. As such there is always a trade off between phase range and loss performance.

1.8 Active Tuning Technologies

In order to enable beam-scanning in reflectarray designs, the reflected phase of each array element has to be actively tunable. In general, the tuning mechanisms can be broken down into two significant categories: discrete and continuous tuning. Discrete tuning technologies typically have smaller losses than continuously tuned elements, the implementation of the control circuit is simpler, and they are typically more reliable. However, discrete tuning introduces phase quantization error, especially in single-bit designs. This error reduces reflectarray directivity [23] and increases side lobe levels [47]. Multi-bit designs can be used to reduce the phase quantization error. However, they introduce higher losses and complicate the biasing networks. In practice, analog phase control tends to be less reliable and introduces complications into the control circuit. However, analog phase control is capable of avoiding phase quantization errors, making reconfigurable elements with large continuous phase ranges highly desirable.

A multitude of tunable components and techniques to integrate them into microstrip antenna elements have been proposed. Each integration technique and each tuning technology have advantages and disadvantages. In general it is desirable to achieve lower phase-sensitivities with larger phase ranges while maintaining low losses. Several reflectarray tuning technologies have been used including RF MEMS [22], [48]–[50], PIN diodes [51], [52], liquid crystal (LC) materials [24], [53], complex oxide-thin films [54]–[57], graphene [58], micro-fluidically pumped liquids [59], varactors [25], [26], [60], [61] and micro-motors [62], [63].

1.8.1 Discrete/Digital Tuning Technologies

While MEMS devices can be designed to operate as a RF switch or a variable capacitor, MEMS capacitors are especially fragile. As such most MEMS devices used in reflectarray design are

discrete switches. MEMS devices have high Q factors at *mm*-wave frequencies, making them attractive for reflectarray applications. Unfortunately, due to the mechanical nature of the tuning mechanism, the switching speeds are significantly slower than other tuning technologies. In [50] an aperture in a patch element's ground plane was loaded with MEMS switches. While multiple switches were used in order to realize multibit tuning, only 150^o phase range was measured. [22] demonstrated an adaptation of the aperture coupled passive reflectarray design in which MEMS switches were loaded onto the open-ended transmission line under the ground plane. The switches were used to vary the effective length of the transmission line.

PIN diodes offer a reliable RF switch with reasonable linearity performance. However, they consume significant biasing power and have degraded *Q* factors above *X* band. The integration of monolithic PIN diodes into an array element was first demonstrated in [51]. Similar to [22], the aperture coupled passive design was modified in [52] utilizing PIN diodes.

1.8.2 Continuous/Analog Tuning Technologies

Nematic liquid crystal materials operate by changing their relative permittivity when an electrostatic field is applied across them. Array elements have been designed by placing LC material between the resonating element and the ground plane; when the liquid crystal is biased the array element resonant frequency shifts. While the operating principle is simple, the fabrication techniques are complicated and the losses of LC are very high at *mm*-wave frequencies and below. Additionally, LC has a slow tuning speed which degrades as the ambient temperature is lowered. Array elements were demonstrated at *X* band in [24] however, the losses were very high. In [64] a multi-resonant array element was shown at *X* band with acceptable losses. However the element was not fabricated using LC. Instead, the LC was substituted with dielectric substrates with varying dielectric constants. If LC had been used the losses would have been much higher.

Complex oxide materials such as Barium Strontium Titanate (BST) have been utilized in reconfigurable reflectarray designs due to their negligible DC power consumption, fast switching speeds, and monolithic integration capability [54]–[56]. While BST films require high biasing voltages on the order of 35 V/μm, they use very small biasing currents on the order of pico-amps. BST has nanosecond switching speeds, making them suitable for beam-scanning radar and multiple-beam applications.

Varactors are a mature technology and high performance models are commercially available. They offer wide capacitive tuning ranges and high quality factors at low frequencies. Unfortunately they tend to suffer from higher losses and non-linearity issues above *X* band. However, their great performance makes them a desirable tuning device for reflectarray design at *X* band and below. In [25], a varactor was placed between a microstrip patch and the ground place to enable reconfigurability. In [26] printed dipoles were loaded with varactors and in [60], a slotted patch loaded with a varactor was designed. In [61] a $\lambda/2$ microstrip patch was bisected, forming two $\lambda/4$ patches. These patches were connected with varactors and a phase range of 320^o was measured.

CHAPTER 2: MONOLITHICALLY-BST-INTEGRATED BEAMSTEERABLE REFLECTARRAY ANTENNAS

2.1 Introduction to BST-Integrated K_a-Band Reflectarrays

BST is a ferroelectric ceramic oxide material whose inherent characteristics make it very desirable for reconfigurable reflectarray applications. When integrated into microstrip patch antennas BST has been used as a distributed varactor, enabling reconfigurability in reflectarray unit cells [65]. BST has a high dielectric constant, negligible DC power consumption, is capable of very quick tuning speeds, and monolithic integration [54], [55], [57], [66]–[69]. In this chapter a 9×5 BST-integrated reflectarray operating at K_a-band is presented. The advantages and limitations of this array are discussed. Then a BST loaded array element operating at *V*-band with a novel interdigital gap configuration is presented. Finally a BST loaded dual-resonance array element operating at K_a-band is demonstrated in simulations. The limitations of BST, in particular the limited tuning range and large loss tangent are then discussed.

While BST has many desirable qualities for reflectarray design, perhaps the most beneficial is the ability to monolithically integrate it into microstrip patch antennas. By cutting a gap through the middle of a traditional $\lambda/2$ microstrip patch and depositing BST in it, a varactor loaded array element is realized without the need for interconnections. This allows BST loaded reflectarrays to operate at much higher frequencies than arrays loaded with discrete tuning elements. Similarly Nematic liquid crystal (LC) loaded elements are also monolithically integrated and have been shown to work above 100 GHz [70]. However, compared to BST, LC suffers from very high losses at *mm*-wave frequencies and much slower switching speeds. Research has been applied to reduce the losses and increase the switching speeds of LC with limited success [71].

2.1.1 *Array Element Analysis*

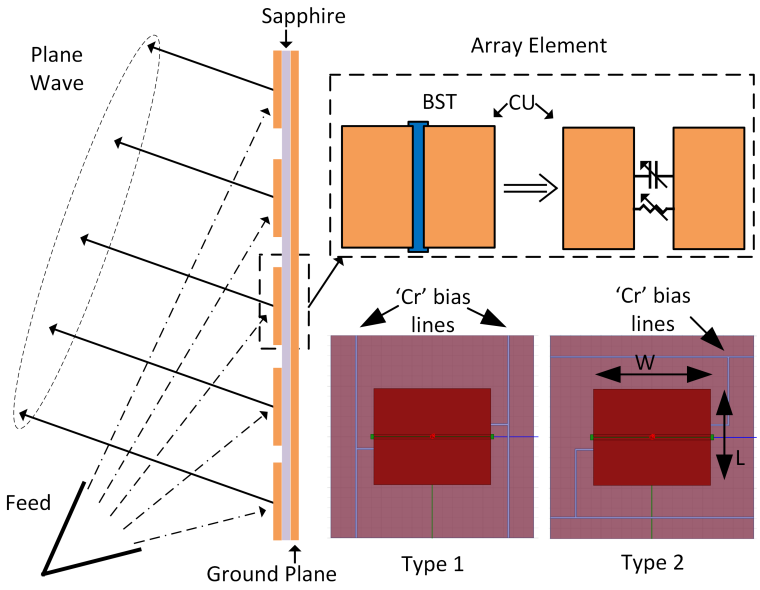

Figure 2.1: Schematic of a reflectarray consisting of the proposed BST-integrated patch elements and two unique biasing schemes. Re-printed from [72]

The array element presented in Fig. 2.1 consists of two $\lambda/4$ microstrip patch antennas separated by a 10 μm gap. The gap is loaded with BST which has been shown to have a dielectric constant of 275 - 500 at K_a band [72]. The BST in the gap forms a distributed capacitor and when a DC biasing voltage is applied across the gap the paraelectric behavior causes the permittivity of the BST to vary, enabling reconfigurability in the array element. This array element design was previously demonstrated in [65], however the inter-element spacing was designed for the dimensions of a K_a-band waveguide and the array performance and angle of incidence effects weren't studied.

The array element is designed to operate at 31.6 GHz and the inter-element spacing is set to be $a = b = 0.42 * \lambda_o$ (4 mm) using a parallel-plate TEM waveguide in simulations to extract the array element's performance under normal incidence. The dimensions of the patch are set to 2.3 *mm (W)* and *1.9 mm (L)*. While the gap between the two $\lambda/4$ patches is 10 μm the BST that is placed in the

gap is purposefully made 20 μm wider to ensure good electrical connections between the copper and BST and to increase acceptable fabrication tolerances. The reflection magnitude and phase response of the array element under normal incidence was extracted and the peak loss is 7.18 dB with a phase range of 240^o.

2.1.2 Array Design

This array element is used to design a 9×5 reflectarray using a column biasing scheme. As such each column of 5 elements is biased using the same voltage. This design choice was made for two reasons, firstly enabling individual biasing of each element would require that vias be drilled in the substrate. However, the substrate is sapphire which makes drilling vias difficult and requires advanced micro fabrication equipment. Secondly, BST requires a biasing voltage of 35 $V/\mu m$ necessitating 350 V to fully tune each array element. To achieve this high voltage commercially off the shelf (COS) DC-DC converters are used, however, they are very costly. As such, the column biasing scheme not only reduces the required number of DC-DC converters by a factor of 5 it also avoids the need for advanced micro fabrication equipment. Unfortunately this column biasing scheme also ensures that there will be phase errors along the column as each array element is biased the same.

The required reflected phase for each element with coordinates (m, n) to point the beam to (θ_b, ϕ_b) is defined by 1.3. Note that from this equation, individual biasing for each element is required. However, with the column biasing network the beam scanning is limited to $\phi_b = 90^o$ and 1.3 is reduced to:

$$\Phi_{des}(n) = k_o * d_n - k_o(n * sin(\theta_b)) \tag{2.1}$$

The phase error along each column isn't considered in 2.1. To reduce these errors a large ***f/D*** is used. This reduces the difference in the physical distance between the feed and the elements in

each column, reducing the phase error when all elements have the same reflected phase. However, this also decreases the aperture efficiency significantly, reducing the gain of the reflectarray.

2.1.3 Fabrication and Measurements

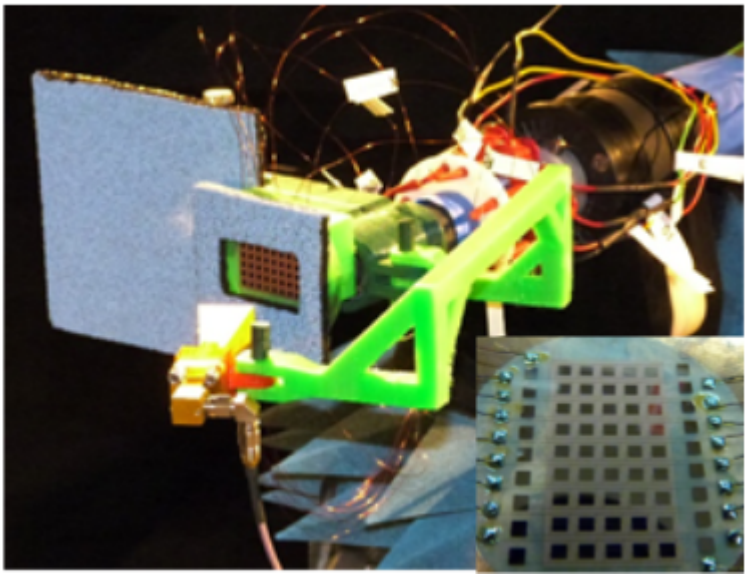

Figure 2.2: Fabricated 5×9 reflectarray using the BST-integrated capacitively loaded patches, and the array measurement setup showing the feed, supporting structures and biasing. Re-printed from [72]

The array is fabricated on a 175μm-thick sapphire substrate in a cleanroom. First the BST is deposited on the wafer using RF magnetron sputtering using a system pressure of 20 mTorr with a consistent gas flow of Ar and O_2. Then the excess BST is etched using photolithography and a 2% HF solution. After which the BST is annealed in a 900^o oven for 12 hours with a constant O_2 gas flow. After the annealing, the BST is crystalline and the biasing network is deposited using the liftoff process before the copper microstrip patches and biasing pads are deposited using electron beam (E-beam) deposition and liftoff. Finally the biasing wires are soldered and the array is mounted in a custom mounting structure as shown in Fig. 2.2. The antenna mounting structure was designed and fabricated using a fused, deposited material (FDM) 3-D printer.

Fig. 2.3 demonstrates continuous beam-scanning from 0^o to $+25^o$ at 31.6 GHz. An increase in the

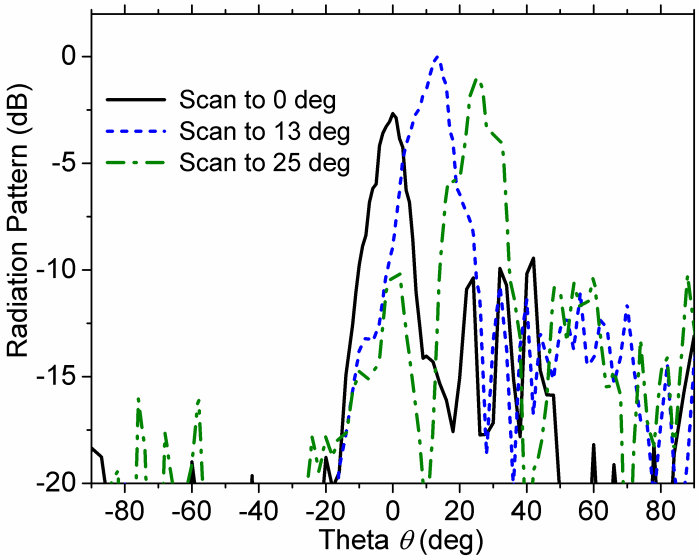

Figure 2.3: Measured radiation patterns showing scanning on E-plane up to 25^o. Re-printed from [72]

gain is observed when scanned to 13^o. This is due to the image lobe being present because of the phase errors caused by the column biasing. Likewise the sidelobe levels are very high, due in large part to the limited phase range of the array element and the biasing scheme.

2.1.4 BST-Integrated Array: Discussion

The presented 5×9 beam-scanning reflectarray is capable of continuously scanning in the E-plane between $0^o - 25^o$. The boresight gain is 8.3 dBi with a 4% 3-dB gain bandwidth. While this reflectarray suffers from the limited phase range and high loss of the array elements it demonstrates that BST-tuned reflectarrays are realistic at K_a band. Next as an extension of this work, the feasibility of the split $\lambda/2$ microstrip patch element at *V* band will be investigated.

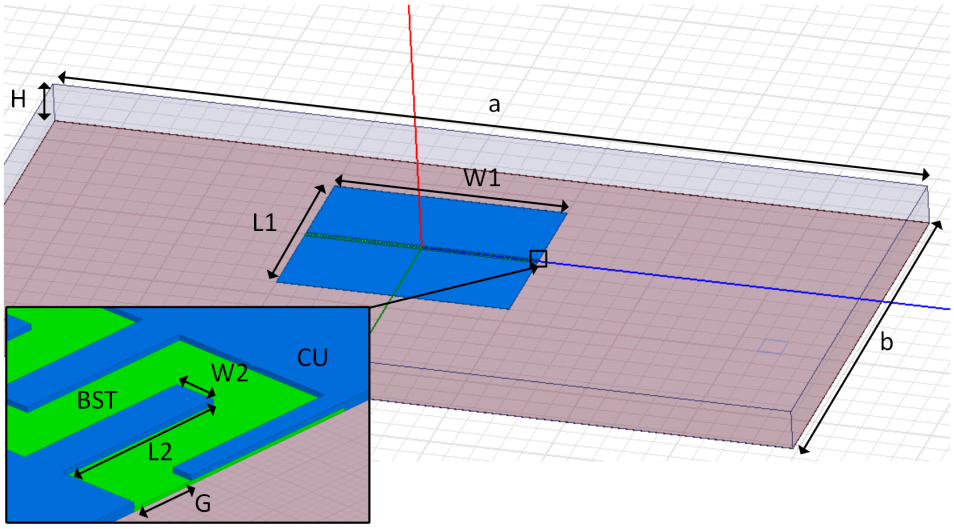

Figure 2.4: Microstrip patch element with BST tunable interdigitated capacitor

2.2 A BST-Integrated *V*-band Patch Element with Inter-digital Gap Configuration

In this section, a *V*-band tunable reflectarray array element using an inter-digital gap loading structure is presented. Reconfigurability is achieved by loading the antenna element with BST thin film along the IDC gap. The effects of substrate thickness and patch width on the reflection properties are investigated using full-wave simulations. A unit cell design demonstrating an overall phase range of 216.3^o and a maximum loss of 6.7 dB at 59.28 GHz is realized. The presented design benefits from the monolithic integration of BST with the patch element and allows for high frequency operation without parasitic losses.

2.2.1 Design & Simulation Setup

A rectangular microstrip patch antenna with a meandering gap made to resemble the fingers of an interdigitated capacitor was shown in [73]. In this study, a similar element integrated with BST for electronic reconfigurability is chosen as the unit cell as shown in Fig. 2.4 where the dimensions are as follows: $L_1 \times W_1 = 0.975 \times 1mm^2, L_2 \times W_2 = 20 \times 5\mu m^2, H = 80\mu m, a \times b =$

$3.7592 \times 1.8796mm^2$. A meandering gap 7.5 μm wide is made along the width of the patch, the fingers are 20 μm long and 5 μm wide. A thin layer of BST film is defined within the gap, which acts as a tunable capacitor, whose permittivity and loss tangent are varied by applying a DC voltage. The patch is made of copper and sapphire ($\epsilon_r = 10, tan\delta < 0.0005$) is chosen as the substrate. Substrate thicknesses of 100 μm and 80 μm and patch widths of 1 mm and 2 mm are simulated to optimize the unit cell. A BST relative permittivity range of 250 - 500 and a loss tangent range of 0.02 - 0.16 is chosen.

A metallic waveguide supporting TE_{10} mode is used to characterize the reflectarray element. This setup accounts for mutual coupling by simulating an infinite array of identical elements with a fixed inter-spacing equal to the cross-sectional dimensions of the standard V-band waveguide (a = 3.7592 mm and b = 1.8796 mm).

2.2.2 Simulation Results

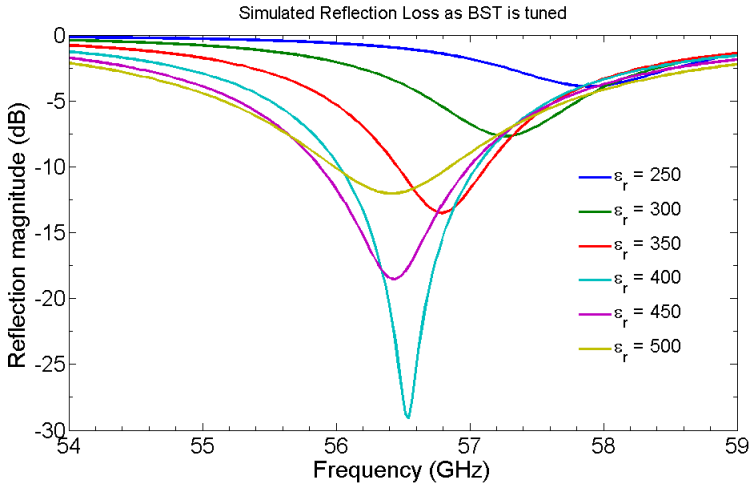

Figure 2.5: Reflection magnitude versus frequency for varying BST relative permittivity values

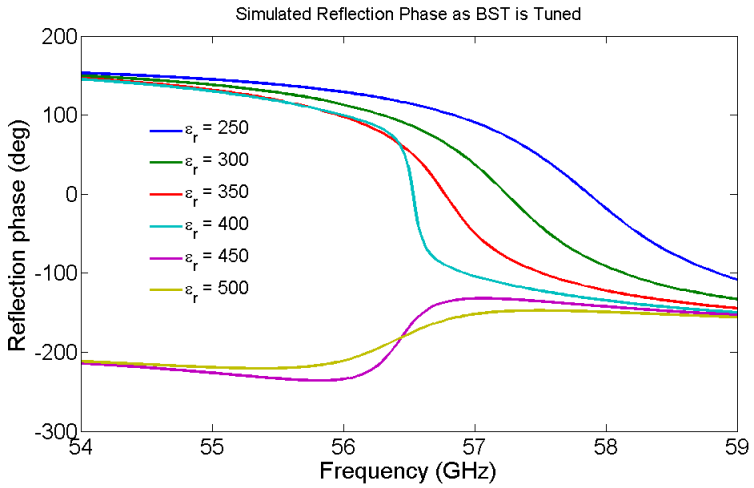

Figure 2.6: Reflection phase versus frequency for varying BST relative permittivity values

Fig. 2.5 shows the variation of the reflection magnitude with respect to frequency across the BST relative permittivity range for 80 μm substrate thickness and 2 mm patch width. It is observed that the resonant frequency varies from 56.42 GHz to 57.89 GHz which corresponds to 2.61% frequency tuning. Fig. 2.6 shows the phase response of the unit cell with respect to the frequency. The patch is under-coupled when the relative permittivity ranges from 450 to 500 and over-coupled for lower values. As expected the loss of the patch increases with the dielectric constant in the over-coupled region, reaches maximum at the critically-coupled condition and decreases in the under-coupled region [74].

It should be noted that while the unit cell transitions from under-coupled to the over-coupled condition, the phase range above the resonant frequency is still continuous. This indicates that so long as the operating frequency is higher than the frequency at which a reconfigurable unit cell becomes critically coupled it is still possible to successfully use an array element that is under-coupled for a portion of its tuning range. While doing so will maximize the available phase range it also maximizes the peak element loss and renders frequencies below the critically coupled frequency unusable.

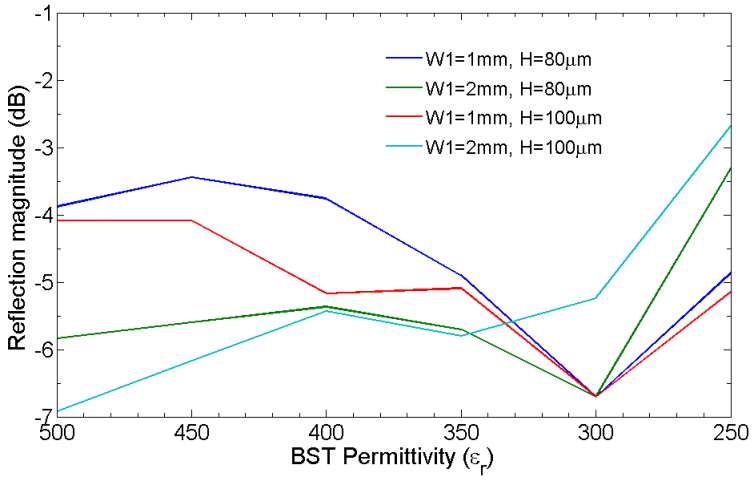

Figure 2.7: Reflection magnitude versus BST permittivity at their respective operation frequencies

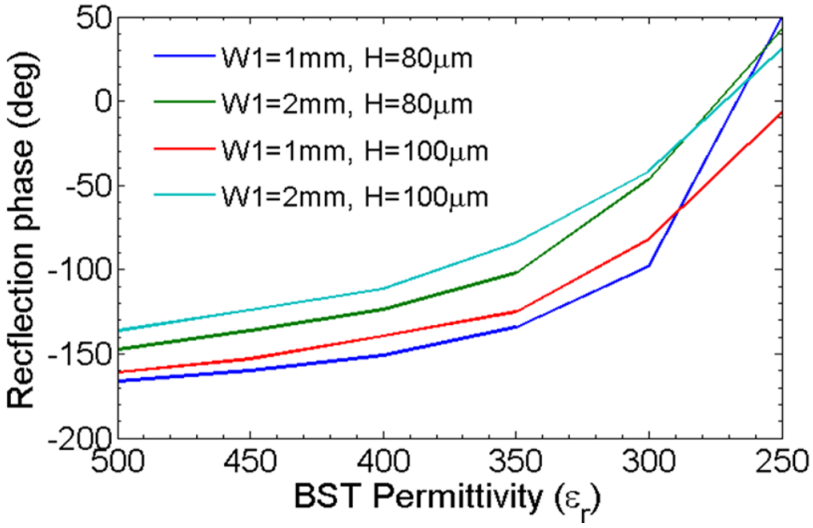

Figure 2.8: Reflection phase versus BST permittivity at their respective operation frequencies

The substrate thickness and patch width affect the phase range and loss performance. Fig. 2.7 shows the reflection magnitude and phase response of the unit cell with respect to BST relative permittivity for four cases, accounting for variations in patch width and substrate thickness. The operational frequency of the patch is chosen such that the phase range is maximized while maintaining a maximum loss of 7 dB. It is important to note that the operational frequency changes

as the width and thickness are varied. In Fig. 2.7, due to the under-coupled condition for high dielectric constants, lower losses are observed for smaller patch widths and substrate thicknesses. From Fig. 2.8 it clearly seen that a maximum phase range was observed for h = 80 μm and W_1 = 1 mm case. Overall, a phase range of 216^o with a maximum loss of 6.7 dB was observed for the optimal case.

2.2.3 Fabrication and Measurements

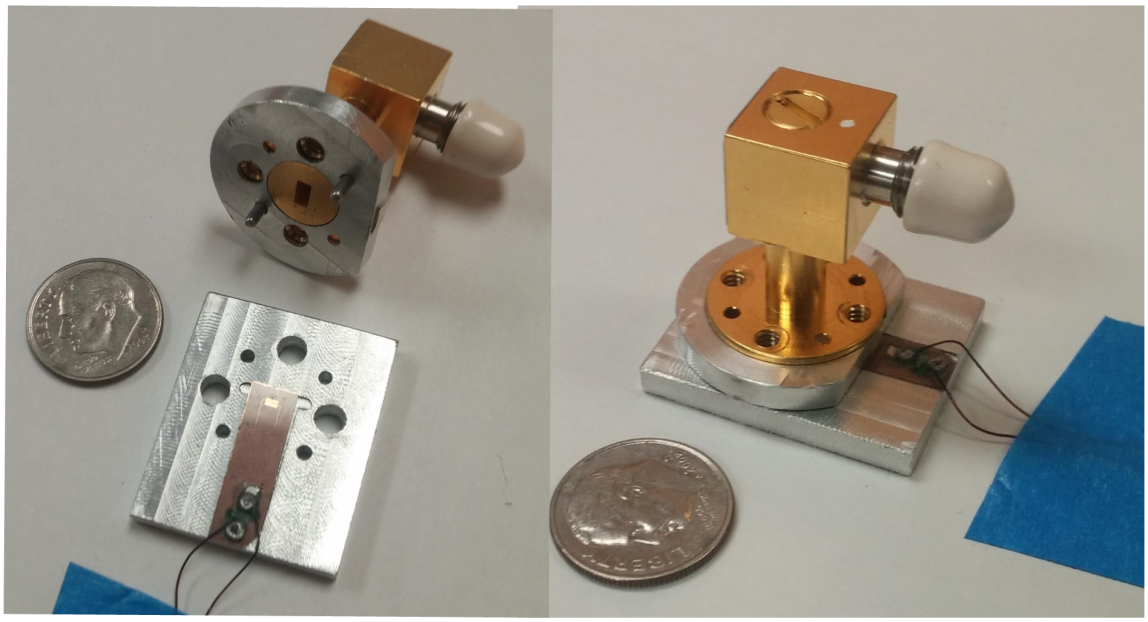

Figure 2.9: Reflection phase versus BST permittivity at their respective operation frequencies

The proposed 1 mm wide unit cell was fabricated on an 80μm thick sapphire substrate. Special preparation was required for the substrate before fabrication of the unit cell could begin. Due to its extreme thinness, the substrate possessed a natural tendency to bow and bend. To remove the flex inherent in the substrate it was necessary to place the cleaned wafer face up into a programmable furnace where the wafer was heat treated at 1000^o C for 10 hours, and then allowed to cool slowly in the furnace for 3 more hours. This treatment resulted in the flat surface required for micro

fabrication. Following the heat treating, BST was deposited using RF magnetron sputtering. After this the BST was patterned with photolithography and etched with a 2% HF solution. Next the microstrip patch was defined via photolithography and copper was deposited with electron beam evaporation before using lift off. The biasing lines were designed using highly resistive chromium and fabricated similarly to the copper layer. Finally the unit cell was diced from the wafer, biasing wires were soldered, and the unit cell was placed in a V-band waveguide as shown in Fig. 2.9 for measurements.

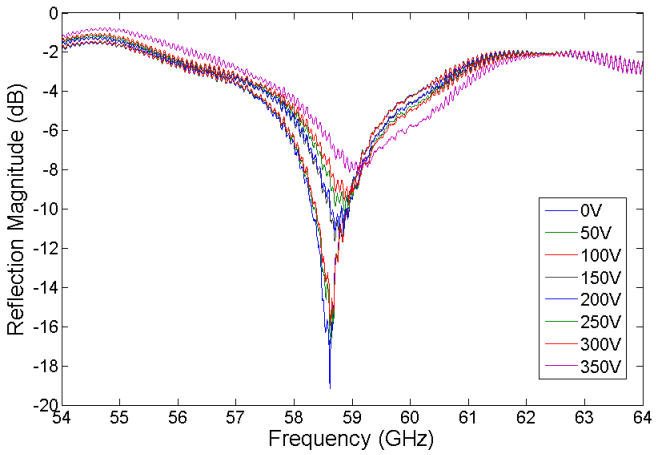

Figure 2.10: Reflection phase versus BST permittivity at their respective operation frequencies

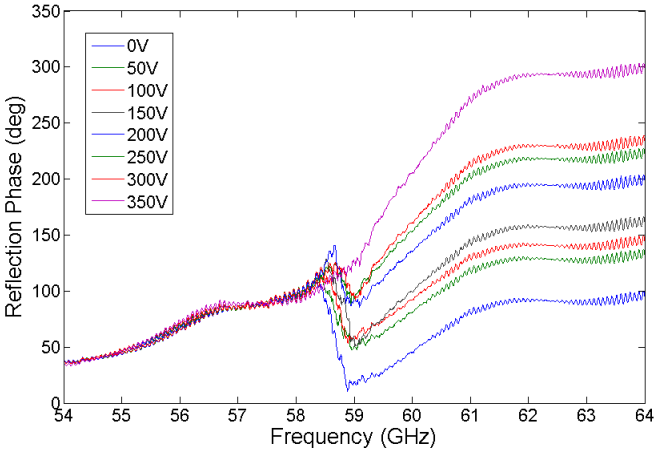

Figure 2.11: Reflection phase versus BST permittivity at their respective operation frequencies

Figures 2.10 and 2.11 show the measured reflection magnitude and phase respectively of the *V*-band unit cell. While the frequency of critical coupling is higher than expected, at 59 GHz instead of 57 GHz, the unit cell is under-coupled with no biasing voltage and becomes over-coupled as the biasing voltage is increased as expected.

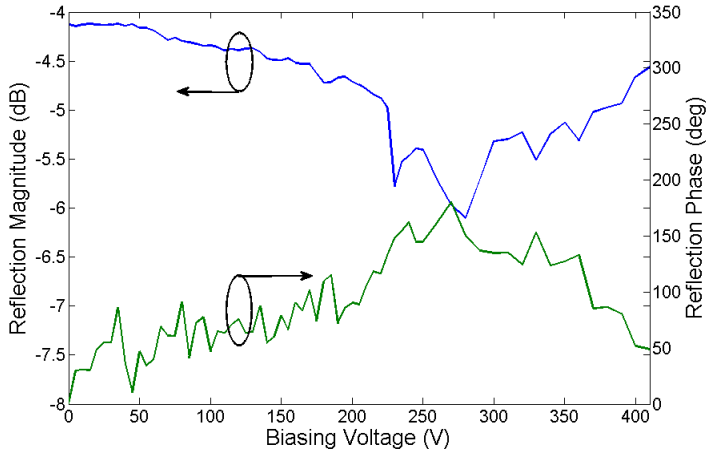

Figure 2.12: Reflection phase versus BST permittivity at their respective operation frequencies

Figure 2.12 shows the loss and phase performance at 60 GHz as the biasing voltage is adjusted from 0 to 400 V. The peak and average loss is 6 and 5.1 dB respectively while the phase range is 193^o. This represents a slightly better loss with a lower phase range than expected, which makes sense given the frequency deviation from the designed frequency. The higher resonant frequency increases the electrical thickness of the substrate, which will result in a more over-coupled resonance, reducing loss and phase slope. The reduced phase slope contributes to the decreased phase range.

2.2.4 V-band Patch with IDC Gap: Discussion

A tunable microstrip reflectarray unit cell operating at 59.28 GHz capable of providing 216^o phase range with a maximum loss of 6.7 dB is demonstrated. This design offers a planar element, and leverages BST technology to provide continuous electronic reconfigurability. The proposed design uses monolithic fabrication to enable a very high operational frequency. These factors combined with a very compact profile make this design attractive to space based communication systems. Unfortunately the element loss is quite high and the phase range is significantly less than 360^o. To rectify these issues a BST-integrated dual-resonance design will be investigated in the next section.

2.3 Dual-Resonance, BST-Integrated K_a-band Reflectarray Element

In this section, a K_a-band tunable dual resonance reflectarray element, its design methodology, limitations, and design tradeoffs are presented. Reconfigurability is achieved by loading the antenna element with BST thin film. The effects of limited frequency tuning, coupling conditions, and inherent loss is investigated using full-wave simulations. A unit cell design demonstrating an overall phase range of 360^o and an average loss of 8.25 dB at 30.97 GHz is realized.

2.3.1 Introduction to Dual Resonance Reflectarray Designs

Reflectarray design relies on the appropriate phase response of each element which is chosen to compensate for the different spatial lengths from the feed to each element in order to achieve constructive interference in the desired direction. The goal of any reflectarray element design is to achieve at least 360^o of phase range with as little loss as possible; this is especially challenging when designing single-resonance microstrip elements. In [75] a reflectarray demonstrating a 1-dB bandwidth of 15.9% is realized using a non-tunable dual resonance double-cross element to

increase the phase-swing and phase-linearity of the array elements.

Many technologies have been used to design phase-agile reflectarray elements such as Nematic liquid crystal (LC) [70], and thin-film BST [76]. LC and BST can be continuously tuned; BST typically possesses a tuning range of approximately 1.81:1 [76] and LC usually demonstrates a tuning range of less than 1.5:1 [70].

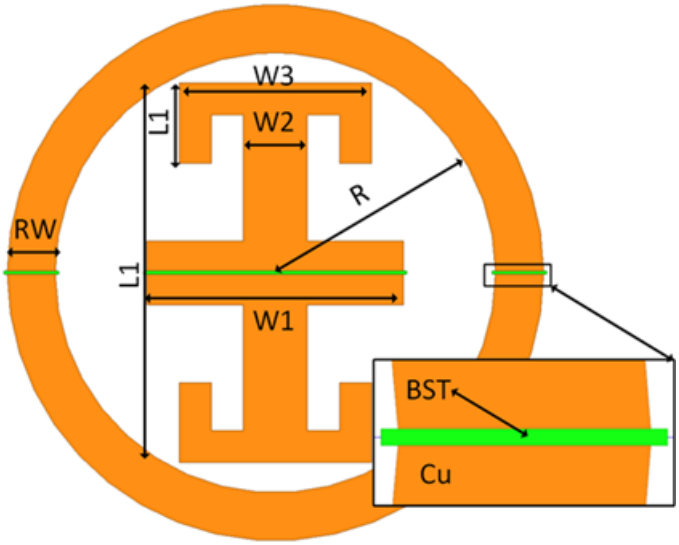

Figure 2.13: Dual resonant element with BST tunable capacitor.

In this section the design process of dual resonance, phase-agile reflectarray elements with a phase range of 360^o is presented. In Fig. 2.13 a dual resonance reflectarray element is presented with the following dimensions: $L_1 = 1.18mm, W_1 = 0.8mm, L_2 = 250\mu m, W_2 = 200\mu m, W_3 = 400\mu m, RW = 150\mu m, R = 0.69mm$. This element is used as an example of a working design operating at K_a-band for the purposes of this discussion. The limitations of the tuning technology and the design constraints this creates is then investigated.

2.3.2 *Dual Resonance Theory*

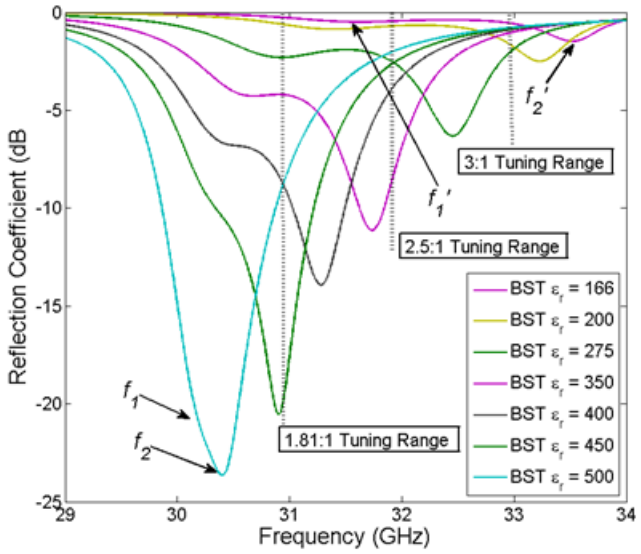

Figure 2.14: Loss performance of the dual resonant element. The tuned and non-tuned frequencies, and the three operating frequencies corresponding to 360^o phase range at the three tuning ranges are marked.

Dual resonance reflectarray elements all share the same core operating characteristics regardless of whether the desired reflection phase is achieved through physical tuning as in [75] or electrically phase-agile elements as in [76]. Regardless of the tuning method, the desired phase response is realized by sweeping the resonant frequency of each resonance. For this discussion the initial resonant frequencies are labeled f_1, f_2 and the tuned frequencies are labeled f_1', f_2' as shown in Fig. 2.14. To achieve a phase range of at least 360^o f_1' must be greater than f_2 and both resonances must be over-coupled [41] across the tuning range. If the coupling conditions of the two resonances are maintained, the frequency range between f_1' and f_2 will have a maximum phase range of at least 360^o.

When designing a non-tunable reflectarray element these requirements are not difficult to realize as the frequency tuning range is driven by physical dimensions and is essentially infinite. In this

case, the frequency separation between f_1 and f_2 can be as large as desired which allows for both resonances to be very over-coupled, limiting the loss of the element. This is true of the design presented in [75] as the element presented resonates at 59.05 GHz and 85.5 GHz in its non-tuned state. However, when designing phase-agile reflectarray elements the frequency tuning range, $f_1' - f_1$ is limited. This limits the acceptable frequency separation between the two resonances $f_2 - f_1$ which puts constraints on the acceptable coupling levels of these resonances.

Three key factors need to be considered when designing a phase-agile reflectarray element: the frequency tuning range of each resonance, the frequency separation of each resonance, and the coupling of each resonance. The frequency tuning range of each resonance will determine the maximum frequency separation between both resonances and is the main limiting factor of the loss performance of the element across the tuning range. The maximum acceptable frequency separation will determine the coupling condition of each resonance; as each resonance is made more over-coupled, the loss decreases [41]. However, as the frequency separation is reduced, the resonances must move closer to critical coupling which creates significantly more loss. From this it can be seen that an increase in the frequency tuning range will result in a decrease in the total loss of the reflectarray element.

2.3.3 Simulation Results

The dual resonance reflectarray element shown in Fig. 2.13 consists of an internal cross structure modified with a mushroom cap for minimization and an external ring structure, both of which are loaded with BST. The element is designed on a 510-μm-thick sapphire substrate and simulated in a K_a-band waveguide to simulate the element being surrounded by an infinite array of identical elements. A BST relative permittivity range of 500 - 275 is known to be accurate and represents a 1.81:1 tuning range however for the sake of this discussion ranges of 2.5:1 and 3:1 are also

investigated and the loss performance is compared.

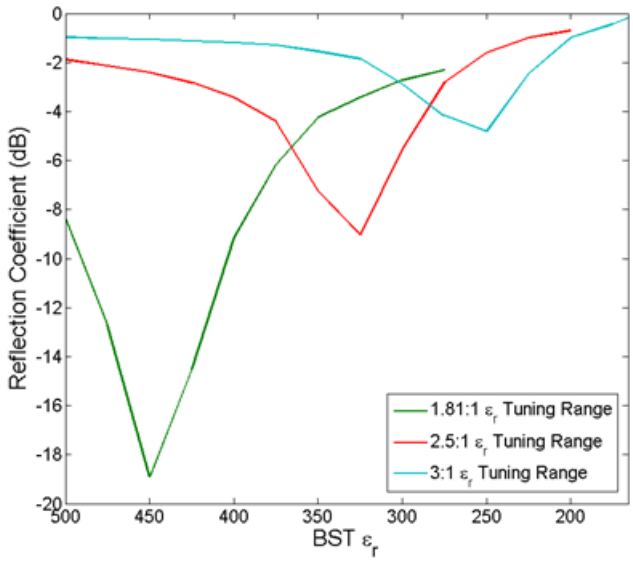

Figure 2.15: Loss performance at operating frequencies that provide 360^o phase range for the three chosen BST tuning ranges. These frequencies are 30.97 GHz, 31.98 GHz, and 32.7 GHz.

Fig. 2.14 shows the reflection coefficient for this unit cell as the dielectric constant is tuned from 500-166 covering all three proposed tuning ranges. Also, three separate operating frequencies are marked indicating the frequency at which 360^o of phase range is realized with all three BST tuning ranges. Fig. 2.15 shows the loss at the three marked frequencies as the BST is tuned. The maximum and average loss when considering a 1.81:1 tuning ratio is 18.9 dB and 8.25 dB, respectively. However, when considering a 3:1 ratio the maximum and average loss are reduced to 4.8 dB and 1.72 dB, respectively.

2.3.4 BST-Integrated Dual-Resonance Element: Discussion

The design process and constraints of a phase-agile dual resonance reflectarray element with a 360^o phase range is presented. The effects of a limited frequency tuning range and the optimal

design methodology given a specific frequency tuning range are discussed. A working reflectarray element design displaying 360^o of continuous phase range is presented; however, due to a 2.75% frequency tuning range the loss of this element is very high. Methods of reducing the loss are discussed and hinge on an enhanced frequency tuning range. Future work includes different BST loading mechanisms to increase the frequency tuning range and the application of this design methodology to elements using different tuning technologies. In the next chapter a dual-resonant reflectarray design loaded with varactors is presented. While varactors have increased losses at *mm*-wave frequencies, they have acceptable losses at *X* band and lower frequencies. Varactors also offer significantly larger tuning ranges than BST which will greatly improve the performance of the dual-resonance design presented here.

CHAPTER 3: PHASE-AGILE DUAL-RESONANCE REFLECTARRAY ELEMENT

To overcome the loss and phase range issues presented in the previous chapter a single-layer, dual-resonance, tunable reflectarray unit cell operating at *X* band is presented in this chapter. The unit cell is composed of a cross element and a ring element, both capacitively loaded with varactors, enabling re-configurability. The larger capacitive tuning range of the varactors allows for this design to achieve greater than 360^o of phase range while demonstrating much lower losses than the previous BST tuned element. An equivalent circuit is developed and verified to demonstrate the dual-resonant operational theory and aid in the design of the dual-resonant unit cell. The equivalent circuit is used to demonstrate the underlying physics of dual-resonant reflectarray antennas and provides a systematic design procedure. The proposed design is evaluated using both full-wave simulations and measurements. The effects of external and mutual coupling, and frequency tuning range on the loss and fractional bandwidth of the unit cell are presented. A continuous phase range of 375^o with a peak and average loss of 4.78 and 3.09 dB at 10.0 GHz, respectively, is measured. The presented analysis provides guidelines for optimizing the unit cell performance required for high-efficiency beam-scanning reflectarray antennas.

3.1 Introduction

Microstrip reflectarrays combine the desirable attributes of traditional arrays and reflector antennas: high gain, planar design, low fabrication costs, and spatial feeding [12], while avoiding their disadvantages. Traditional arrays use lossy and costly beamforming networks which are avoided by the spatial feeding in reflectarrays. In addition, the reflectarray's planar design makes the fabrication much more cost effective than the non-planar design of reflector antennas.

It is desirable for highly directive antennas to be capable of beam steering, which while possible with reflector antennas is difficult. Reflector antennas can steer the beam by physically moving the aperture, or by using a mechanically or electronically steered feed [6]. However, mechanically rotating the aperture drastically complicates its mounting structure and provides very slow scanning, while the use of beam-steering feeds is limited to small scan angles or requires an oversized reflector. Phased arrays can introduce phase shifters in the feeding network or use T/R modules to enable beam steering. Nevertheless, T/R modules are costly, power hungry, and generate significant heat while phase shifters introduce high losses [7] and in the case of discrete phase shifters, phase error [8].

The realization of a beam-steerable reflectarray requires that the reflection phase of each antenna element be controllable. Several techniques have been used to implement phase agility in reflectarray antenna elements such as loading the unit cells with tuning elements in the dielectric, the ground plane, or on the patch element itself [25], [50], [77], as well as aperture-coupling patch elements to a transmission line loaded with tuning elements [78]. Many technologies have been used to realize these tuning elements: PIN diodes [79], Micro-Electro-Mechanical Systems (MEMS) [80], nematic liquid crystal (LC) [64], graphene [81], Barium Strontium Titanate (BST) [82], and varactors [83].

In general, reflectarray phase control can be organized into two groups, discrete and analog. Discrete tuning is desirable for several reasons: discrete devices such as PIN diodes [52] and MEMS switches [84] typically have lower losses; the implementation of the control circuit is simpler; and they are typically more reliable. However, discrete tuning introduces phase quantization error, especially in single-bit designs. This error reduces reflectarray directivity [23] and increases side lobe levels [47]. While multi-bit designs reduce this error, they also introduce higher losses and complicate the biasing networks. In practice, analog phase control tends to be less reliable and introduces complications in the control circuit. However, analog phase control is capable of

avoiding quantization errors, making reconfigurable elements with large continuous tuning ranges worth investigation. Graphene, LC, and BST offer continuous tuning [85]–[87]. However, both graphene and LC exhibit high losses at sub-millimeter wave frequencies [88], [89]. BST has been shown to be capable of high power handling and very quick tuning speeds. However, it introduces significant loss for reflectarray antennas due to its limited tuning range [72]. In this chapter, semiconductor varactors are chosen for the tuning elements since they can operate at X band with very large tuning ranges and good loss performance [83]. It should be noted that the Q-factor-based design theory presented herein is similarly applicable to discrete tuning.

When designing reflectarrays, the loss and phase performance of the array elements are critical. It is desirable to have array elements that exhibit at least 360^oreflection phase range with both low losses and low phase slopes. Non-tunable, dual-resonant unit cells have been demonstrated in [90] and [46] in which the two resonances have been coupled together to provide a phase range in excess of 360^o. A phase-agile dual-resonance reflectarray element is highly desirable for beam-steerable reflectarray antennas due to its increased phase range. However, its design is complicated since both resonances need to be tuned appropriately to ensure the mutual coupling between them does not significantly vary over the frequency tuning range. In [91], a BST-loaded dual-resonant reflectarray element was proposed with greater than 360^ophase range at Ka band. Losses were still very high largely due to the limited tuning ratio of 1.81:1 from the BST dielectric constant. In [92] a dual-resonant reflectarray element loaded with six varactors was presented at C band. However, discussion on the operating theory was limited.

In this chapter, an equivalent circuit is developed and used to demonstrate the underlying physics behind the operation of phase-agile dual-resonant reflectarray elements. Q-factor theory is used to contrast the inherent design tradeoffs, providing a method to optimize unit cell performance which is applicable to many disparate designs. This theory is used to guide the design of a single linearly-polarized, electronically-reconfigurable dual-resonant reflectarray unit cell loaded with varactors

and operating at X band. The design and optimization of the biasing network are discussed, and the fabrication and measurement of the array unit cell are presented.

3.2 Operational Theory

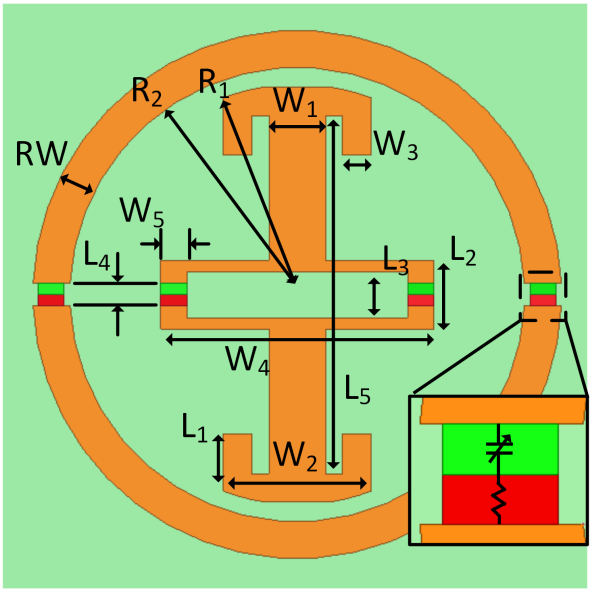

Figure 3.1: Configuration of the cross/ring dual-resonant reflectarray unit cell.

The dual-resonant unit cell shown in Fig. 3.1 consists of a cross structure placed inside a ring structure, both of which are loaded with two varactors. The dimensions are as follows: *RW = 325 μm, R1 = 1.83 mm, R2 = 2 mm, W1 = 500 μm, W2 = 1.3 mm, W3 = 250 μm, W4 = 2.4 mm, W5 = 228 μm, L1 = 600 μm, L2 = 600 μm, L_3= 400 μm, L4 = 200 μm, L5 = 3.153 mm, Substrate thickness h = 1270 μm.*The varactors (MACOM MA46580-1209) were chosen for their high capacitance tuning ratio and high quality (Q) factor. The datasheet for these varactors state that the capacitance ranges from 0.15-1.0 pF with a minimum Q of 3000 at 50MHz. However, it was observed in this study that at 10 GHz, the varactors equivalent series resistance (ESR) increases significantly when tuned to capacitances larger than 0.4 pF. Thus, operating from 0.15-0.4 pF can

greatly improve the loss performance of the varactors. The internal cross element is also loaded with a mushroom cap of width W_2 and length L_1 for minimization. The dual-resonant unit cell is placed inside an X-band waveguide (a = 22.86 mm, b = 10.16 mm) to simulate the effects of mutual coupling in an infinite array and to facilitate measurements.

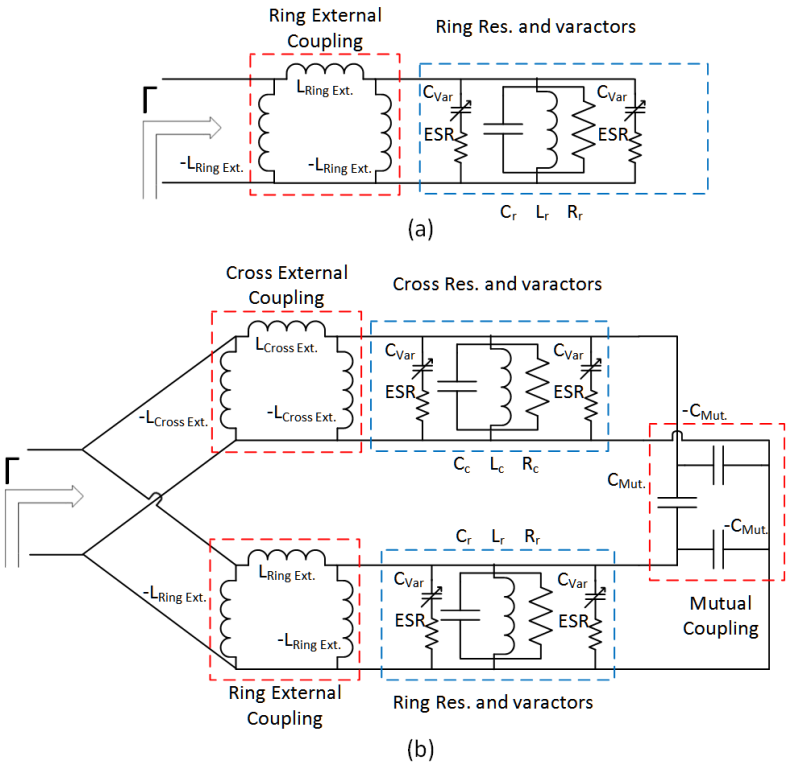

Figure 3.2: Equivalent circuit model for (a) isolated ring and (b) dual-resonant unit cell configurations.

Table 3.1: Equivalent Circuit Values as Varactors are Tuned

C_{Var}(pF)	$L_{Ring\ Ext.}$(nH)	$L_{Cross\ Ext.}$(nH)	C_{Mut}(nF)
0.15	1.208	14.743	167.3
0.2	1.241	4.783	192.9
0.25	1.300	3.301	217.8
0.3	1.365	2.497	230.5
0.35	1.416	2.204	256.7
0.4	1.469	2.030	281.1

To aid in the design of the dual-resonant unit cell, the equivalent circuits shown in Fig. 3.2 were developed using Keysight Advanced Design System (ADS). 3.2(a) shows the equivalent circuit for the ring structure when it is simulated in isolation in an *X*-band waveguide. The circuit component values are as follows: *$L_{Cross\ Ext.}$ = 2.03 nH, $L_{Ring\ Ext.}$ = 1.469 nH, C_{Mut} = 810 nF, C_c = 2.917 pF, L_c = 68.3 pH, R_c = 700 Ω, C_r = 1.65 pF, L_r = 0.1165 nH, R_r = 2.86 kΩ, C_{Var} = 0.4 pF, ESR = 1 Ω.* The inductive π -network $L_{RingExt.}$, represents the coupling between the incident TE_{10} mode from the waveguide to the ring structure. The resonating ring structure is represented as a parallel RLC resonator while the varactor loading is represented by two parallel variable capacitors, Cvar each with a given ESR. These equivalent circuits model the electrical performance of the proposed unit cell and are developed by extracting component values from HFSS simulations. First, the L, C, and C_{Var} values are found by matching the resonant frequency and frequency tuning range of the ring/cross in HFSS where the ring/cross are simulated in isolation. Then the $L_{Ext.}$ and R values are set by matching the loss and phase slope at the resonant frequency. $C_{Mut.}$ is set to match the HFSS simulation results when the antenna elements are combined. As the varactors are tuned, the electrical length of both elements change, altering the external and mutual coupling. Table 3.1 details the equivalent circuit component values for several varactor capacitances.

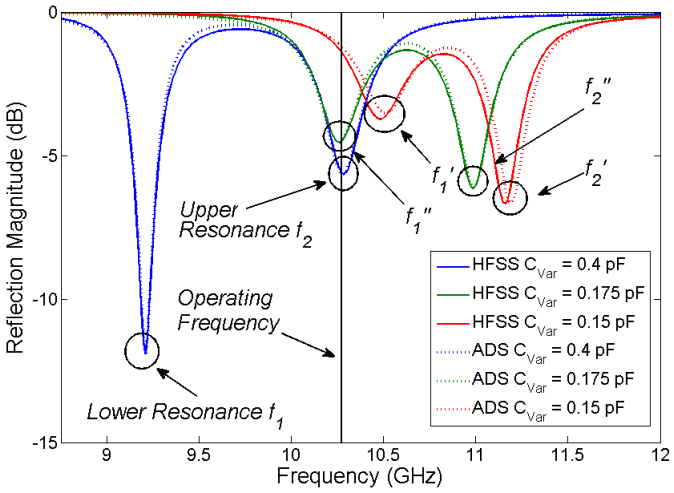

Figure 3.3: Comparison of HFSS and ADS simulations of the reflection magnitude of the dual-resonant element at three varactor capacitances.

Fig. 3.3 shows the reflection magnitude of the dual-resonant unit cell utilizing HFSS and the equivalent circuit, where f_1 and f_2 denote the frequency of the lower and upper resonances, respectively, when the varactors are set to 0.4 pF. When they are tuned to 0.15 pF, the resonant frequencies $f_1$and f_2 shift to f_1' and f_2', respectively. In the same figure, f_1'' and f_2'' correspond to the case when the varactors are tuned to 0.175 pF. There is good agreement in the simulation results between HFSS and ADS showing that the equivalent circuit can be used as a design aid.

Before discussing the operational theory behind dual-resonant reflectarray designs, the use of Q factors in analyzing the reflection properties of reflectarray unit cells needs to be understood, as reported in [41]. The reflection coefficient at the antenna element surface is expressed as

$$\Gamma(f) = \frac{\frac{1}{Q_{rad}} - \frac{1}{Q_o} - \frac{2j(f-f_r)}{f_r}}{\frac{1}{Q_{rad}} - \frac{1}{Q_o} + \frac{2j(f-f_r)}{f_r}} \tag{3.1}$$

where Q_{rad} is the radiation Q factor and Q_o is the parallel combination of metallic loss Q_c and dielectric loss Q_d of the antenna element while f_r is the resonant frequency. The reflection coefficient

at the resonant frequency can be derived from 3.1 as

$$\Gamma(f) = \frac{\frac{1}{Q_{rad}}}{\frac{1}{Q_{rad}} - \frac{1}{Q_o}} \tag{3.2}$$

It can be observed from 3.2 that there are three distinct conditions: critically-coupled ($Q_{rad} = Q_o$); under-coupled ($Q_{rad} > Q_o$); and over-coupled ($Q_{rad} < Q_o$).

3.2.1 Cricitally-coupled Condition

When the unit cell is critically-coupled, the radiation Q is equal to Q_o, and the reflection coefficient given by 3.2 is zero. In this condition, all of the incident energy is dissipated inside the unit cell.

3.2.2 Under-coupled Condition

If the unit cell is under-coupled, the radiation Q is larger than Q_o. The reflection phase at resonance is always $180^o$and the unit cell exhibits an anomalous phase phenomenon as previously observed in [93] and [94]. This phase response provides no phase range and is not desirable for reflectarray applications.

3.2.3 Over-coupled Condition

When $Q_{rad} < Q_o$, the unit cell is considered to be over-coupled, and the reflection phase around the resonant frequency is continuous. This phase behavior makes the over-coupled condition necessary for reflectarray applications. If the ring resonator of the equivalent circuit shown in 3.2 is under-coupled, it is necessary to decrease Q_{rad} of the ring to reach the over-coupled condition by reducing the value of $L_{RingExt.}$

3.2.4 *Phase Range Optimization*

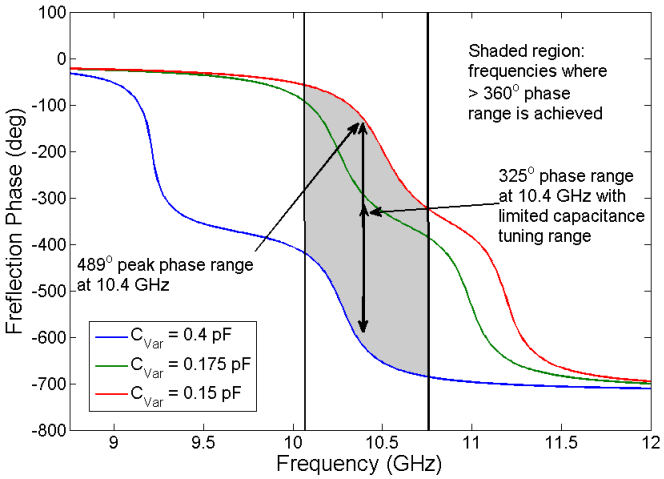

Figure 3.4: Reflection phase of dual-resonant unit cell at three different varactor capacitances with both resonances over-coupled.

There are two main reasons to utilize dual-resonant unit cells in reflectarray design: to increase the available phase range to greater than 360^o, and to provide a more linear phase slope to improve bandwidth. The core principle of dual-resonant reflectarray designs is to couple two over-coupled resonating structures together so that the phase shift induced by each resonance can be combined, increasing the total phase range of the array element. Fig. 3.4 shows the phase response of the equivalent circuit in Fig. 3.2(b). When the varactors are tuned to 0.15 pF, the maximum phase is $489^o$and at least 360^ophase range is available from 10.1 – 10.7 GHz. It is observed in Fig. 3.3 that $f_1' > f_2$. However, if the smallest capacitance of the varactor is limited to 0.175 pF, the peak phase range is reduced to 325^o. As shown in Fig. 3.3, $f_1'' < f_2$.

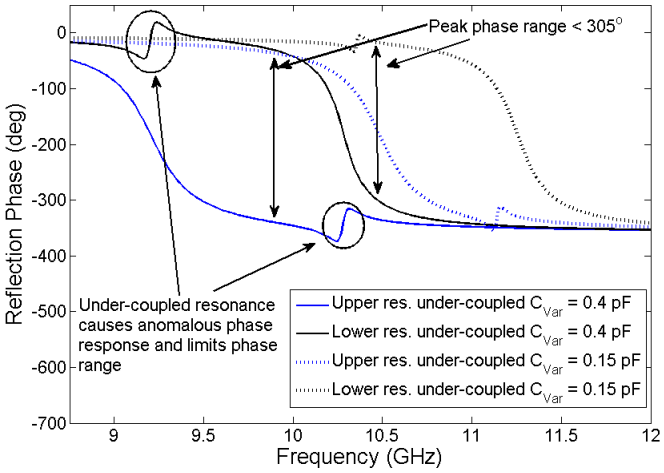

Figure 3.5: Reflection phase of dual-resonant unit cell at three different varactor capacitances with one of the two resonances under-coupled.

In Fig. 3.5 the inductive π-networks of the equivalent circuit are adjusted so either the upper or the lower resonance is under-coupled. When either the cross or the ring element is under-coupled, the peak phase range is under 305^o, as shown in Fig. 3.5. In both cases, the frequency tuning range is great enough to ensure $f_1' > f_2$. However, the anomalous phase response adds no additional phase range.

3.2.5 *Phase Slope at Resonance*

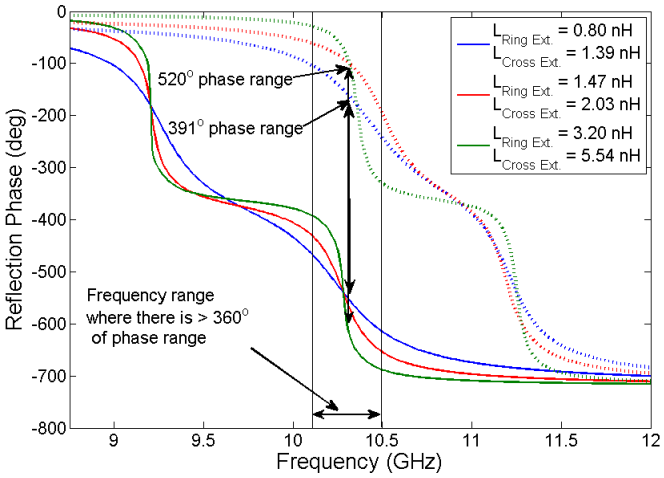

Figure 3.6: Reflection phase of the dual-resonant element with different external coupling conditions when C_{Var} is set to 0.4 and 0.15 pF.

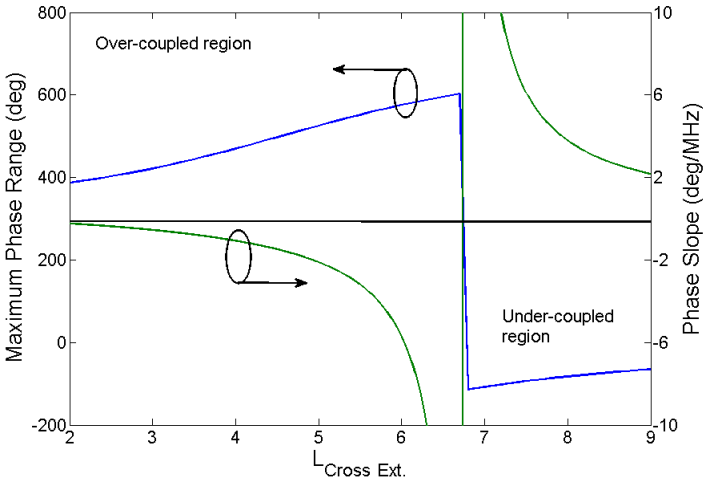

Figure 3.7: Phase range and phase slope at 10.3 GHz of the dual-resonant unit cell using the equivalent circuit where $L_{Ring\ Ext.} = 0.35\ L_{Cross\ Ext.}$.

The bandwidth of a reflectarray is limited by the sensitivity of the reflection phase vs. frequency [38], [37]. To reduce this sensitivity, the phase response can be made more linear by reducing the phase slope around the resonant frequency. Fig. 3.6 demonstrates the effects of varying the Q_{rad} of

each resonance using the equivalent circuit model. The solid and dashed traces denote the varactors being tuned to 0.4 and 0.15 pF, respectively. From Fig. 3.6, it can be seen that decreasing Q_{rad} will reduce the phase slope of each resonance and improve the bandwidth performance. However, Q_{rad} also affects the phase tuning range. Fig. 3.7 shows the maximum phase range and phase slope at 10.3 GHz for several values of $L_{CrossExt.}$ and $L_{RingExt.}$ where $L_{RingExt.}$ = 0.35$\times L_{CrossExt.}$. The discontinuous phase slope when $L_{CrossExt.}$ is 6.74 nH is due to both resonances being critically coupled. Decreasing $L_{CrossExt.}$ from 6.65 to 2 nH causes the phase range and phase slope to reduce from 600^{o}and -53.68^o/MHz to 387.2^{o}and -0.237^o/MHz, respectively. In general, there is a tradeoff between phase range and phase slope.

3.2.6 Mutual-coupling

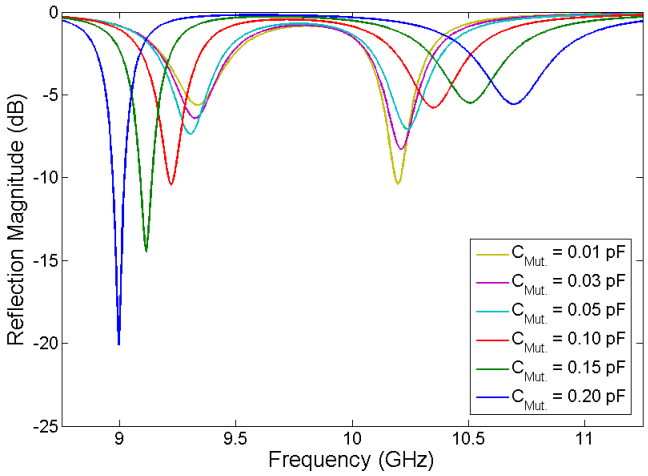

Figure 3.8: Reflection magnitude of the dual-resonant unit cell equivalent circuit as the capacitive π-network representing the mutual coupling between the resonators is tuned.

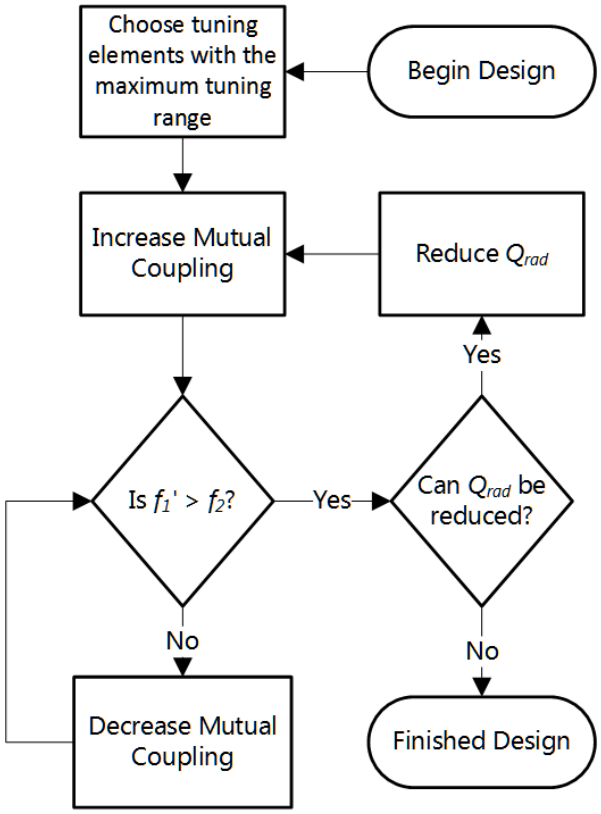

Figure 3.9: Algorithm used to design dual resonant reflectarray unit cells.

The equivalent circuit is used to demonstrate the effects of both strong and weak mutual coupling in Fig. 3.8, where both resonances are over-coupled. As the mutual coupling level increases, the loss of the upper resonance decreases and the frequency separation between the two resonances increases. As previously demonstrated, to achieve greater than 360^ophase range, the condition $f_1' > f_2$ must be satisfied. However, this condition may not be met for a strong mutual coupling case due to the limited tuning range of the varactors, resulting in less than 360^ophase range. The design flow of any dual-resonant phase-agile array element is shown in figure Fig. 3.9.

3.3 Design Procedure and Simulations

3.3.1 Substrate Thickness

The choice of substrate thickness is critical for the dual-resonant unit cell, as it affects the loss and phase sensitivity of both ring and cross elements, as well as the mutual coupling between them.

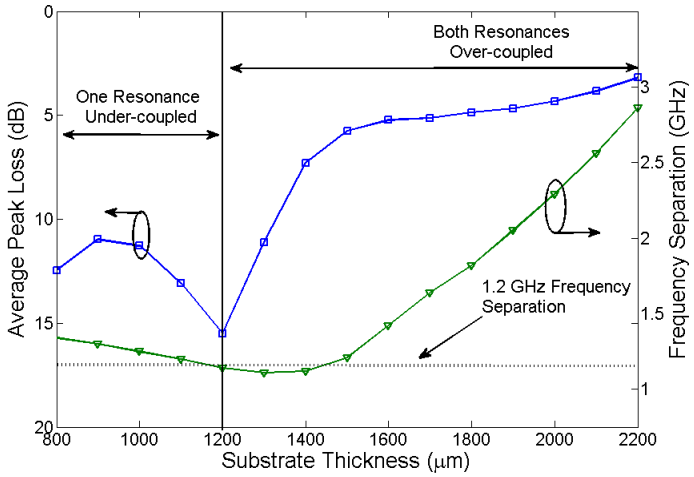

Figure 3.10: The average peak loss and frequency separation between the two resonances of the dual-resonant unit cell as a function of the substrate thickness in HFSS. The varactors are adjusted to 0.4 pF.

Fig. 3.10 shows the average peak loss and the frequency separation between the two resonances of a dual-resonant unit cell as the substrate thickness is adjusted. The average peak loss is the average loss at the resonant frequencies of lower and higher resonances. As the substrate thickness increases, the average peak loss decreases. This is due to a reduction in the Q_{rad} of each resonance which has been shown to be inversely related to substrate thickness [41]. Under 1200 μm the loss decreases, however, this is due to one of the resonances becoming under-coupled.

The substrate thickness greatly affects the mutual coupling between the two resonating structures. Fig. 3.10 shows that when the substrate thickness is increased, the frequency separation between

the two resonances also increases, indicating an increase in the mutual coupling strength. The substrate thickness is designed to be as thick as possible while maintaining a frequency separation that is less than the frequency tuning range of the antenna element. In this design, the dual-resonant unit cell has a frequency tuning range of 1.2 GHz which makes 1450 μm the ideal substrate thickness marked by the horizontal line in Fig. 3.10. However, this substrate thickness is not an industry standard and therefore a substrate thickness of 1270 μm was chosen instead.

3.3.2 Frequency Tuning Range Optimization

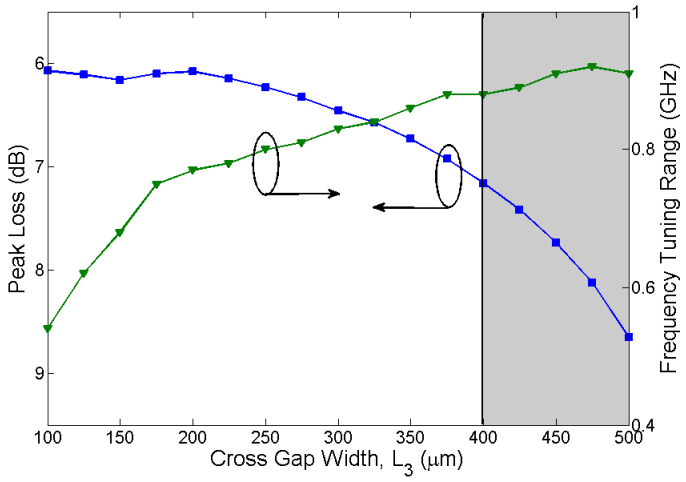

Figure 3.11: The average peak loss and frequency tuning range of the isolated cross element in HFSS as the cross gap width L_3 is varied and the varactors are tuned between 0.15 – 0.4 pF.

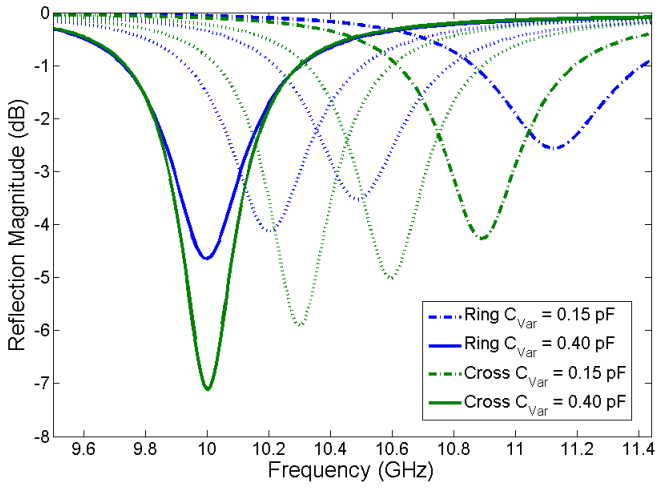

Figure 3.12: Reflection magnitude of the isolated ring and cross structure from HFSS as the varactor capacitance is varied from 0.15 to 0.4 pF.

To simplify the design of the biasing network, both ring and cross elements are biased with the same voltage. Thus, the frequency tuning range of both elements must be similar. Otherwise the mutual coupling between them will change significantly as the varactors are tuned. Additionally, to satisfy the $f_1' > f_2$ condition while using a large substrate thickness, the frequency tuning range of both elements should be maximized. The frequency tuning range of the cross element is not only dependent on the varactor but also on the gap L_3. Fig. 3.11 shows that larger L_3dimensions can enhance the frequency tuning range of the cross, however, at the expenses of higher peak losses. Therefore, the optimal value of L_3, for the trade-off between loss and frequency tuning range, is 400 μm as shown in Fig. 3.11.

Fig. 3.12 shows the reflection magnitude of the ring and cross elements when simulated individually; both elements are over-coupled over the entire varactor tuning range. The frequency tuning range of the cross is similar to that of the ring element. The loss of the cross element is 2.5 dB higher than the ring element when the varactors are set to 0.4 pF. However, the loss of the ring and cross elements are reduced by 2.1 and 2.9 dB, respectively, as the varactors are tuned to 0.15

pF. When the dual-resonant unit cell is formed by combining the two resonating structures, the frequency separation between the two resonances is larger than what is allowed by the substrate thickness. Therefore, the natural resonant frequency of ring is adjusted to 9.43 GHz in order to achieve 1.1 GHz frequency separation.

3.3.3 Loss Optimization

The operating frequency of the dual-resonant reflectarray unit cell will be chosen as f_2. As long as both resonances are over-coupled and $f_1' > f_2$, it will have greater than 360^o phase range. When the varactors are tuned to 0.4 pF, the lower resonance resonates at 9.2 GHz, well below the frequency of operation. Thus, in this configuration, the loss of this resonance does not affect the loss performance of the dual-resonant unit cell. However, the loss of the upper resonance does, as it resonates at the operating frequency. Additionally, the loss of both resonances is expected to decrease as the capacitance of the varactors is reduced. This makes it important to minimize the loss of the upper resonance at 0.4 pF even if it increases the loss of the lower resonance.

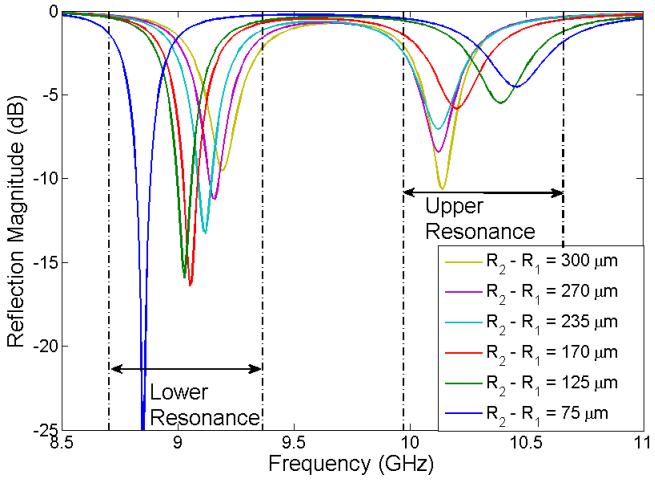

Figure 3.13: Reflection magnitude of the dual-resonant element as the physical spacing between the two elements is varied in HFSS. The varactors are adjusted to 0.4 pF.

From Fig. 3.8, it is observed that changes to the mutual coupling level will affect the loss of the upper resonance. The substrate thickness has been shown to affect the mutual coupling. However, it also affects many other parameters and therefore is not suited to fine tune the mutual coupling. Another method to control the mutual coupling is to adjust the physical separation between both elements. The cross element was designed with a mushroom cap structure consisting of W_2 and L_1 as shown in Fig. 3.1. When L_1 is increased, the resonant frequency of the cross is reduced. If the resonant length of the cross element R1 is simultaneously decreased, the resonant frequency remains the same. This allows for the physical spacing between the ring and cross elements to be controlled without changing the resonant frequency of either one. The effect of changing R2 – R1 is illustrated in Fig. 3.13, which is very similar to Fig. 3.8. As demonstrated in Section II, the mutual coupling should be increased to reduce the loss of the upper resonance, while ensuring the frequency separation is less than the frequency tuning range. Thus, the physical spacing was set to 170 μm as the frequency separation is 1.1 GHz.

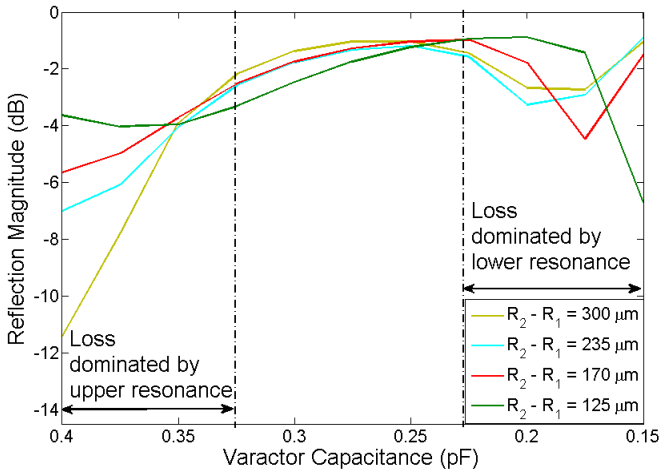

Figure 3.14: Reflection magnitude of the dual-resonant element at 10.3 GHz for several physical spacing as the varactors are tuned in HFSS. L_1 is varied inversely to R1 such that the cross resonates at the same frequency and R_2 is held constant.

In Fig. 3.3, the lower and upper resonances resonate at 10.3 GHz when the varactors are tuned

to 0.175 and 0.4 pF, respectively. Thus, the loss at the operating frequency is the loss of each resonance at these capacitance values. When the varactor capacitance is between these values, neither is at 10.3 GHz, reducing the loss. Fig. 3.14 shows the loss at 10.3 GHz as the varactors are tuned and the physical spacing is varied. When the physical spacing is increased to be greater than 170 μm, the loss at the operating frequency at the low capacitance values does not vary significantly but the loss at 0.4 pF increases from 5.6 to 11.4 dB. While decreasing R2 – R1 to 125 μm will reduce the loss at 0.4 pF, the loss at 0.15 pF increases significantly and the frequency separation is larger than the frequency tuning range.

3.3.4 Simulation Results

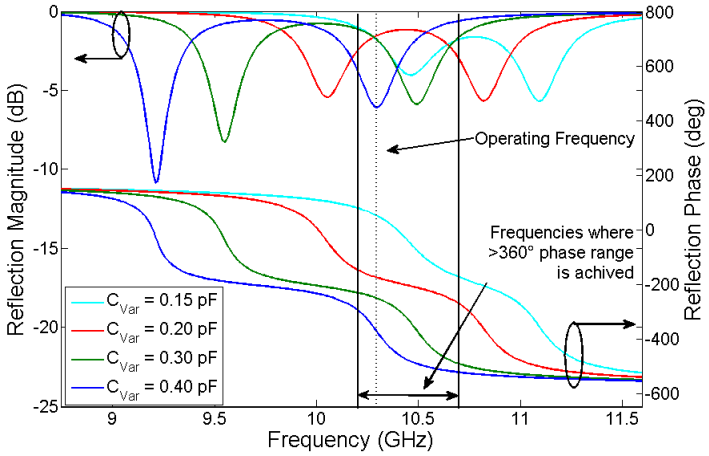

Figure 3.15: Reflection magnitude and phase of the complete dual-resonant unit cell shown in Fig. 3.1 simulated in HFSS as the varactor capacitance is tuned.

Fig. 3.15 shows the reflection magnitude and phase of the optimized dual-resonant unit cell versus frequency, as the varactors are tuned. Due to the X-band waveguide used to simulate the mutual coupling of an infinite array, the waves both incident on and transmitted by the unit cell are TE_{10} mode waves. From Fig. 3.15, it is shown that both resonances are over-coupled throughout the

entire tuning range. There is a region from 10.2-10.7 GHz in which greater than 360^{o}continuous phase range is observed. It is also shown that the loss of the lower resonance decreases from 12 to 4.5 dB over the varactor tuning range while the loss of the upper resonance slightly increases. The increase of the loss of the upper resonance when the varactor is set to 0.15 pF is mainly due to the fact that the frequency separation is reduced from 1.1 GHz (0.4pF) to 0.67 GHz (0.15 pF).

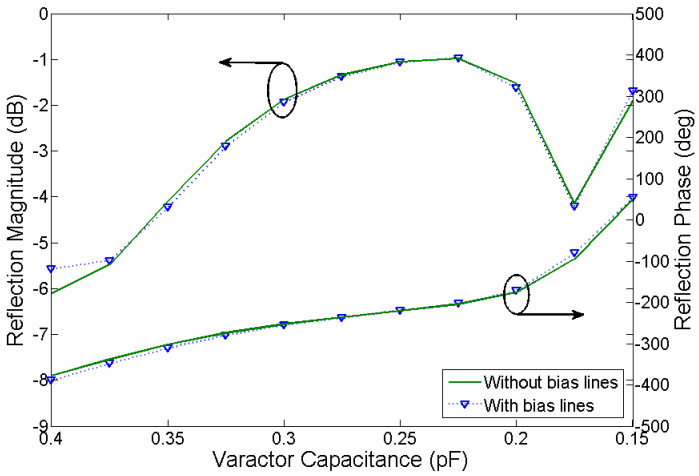

Figure 3.16: Simulated reflection magnitude and phase of the final design, versus varactor capacitance with and without the biasing network at 10.3 GHz.

The loss and phase response of the dual-resonant unit cell at 10.3 GHz versus the varactor capacitance are shown in Fig. 3.16. It is observed that the dual-resonant element has a phase range greater than 440^{o}while the peak loss is 5.57 dB and the average loss across the tuning range is only 2.81 dB. In this design, it is found that $f_1' > f_2$ even when the varactor tuning range is limited to 0.15 – 0.35 pF. From Fig. 3.16, when the varactors are tuned between 0.15 – 0.35 pF, the unit cell demonstrates a phase range of 365^o, while the peak and average loss are reduced to 4.2 dB and 2.22 dB, respectively.

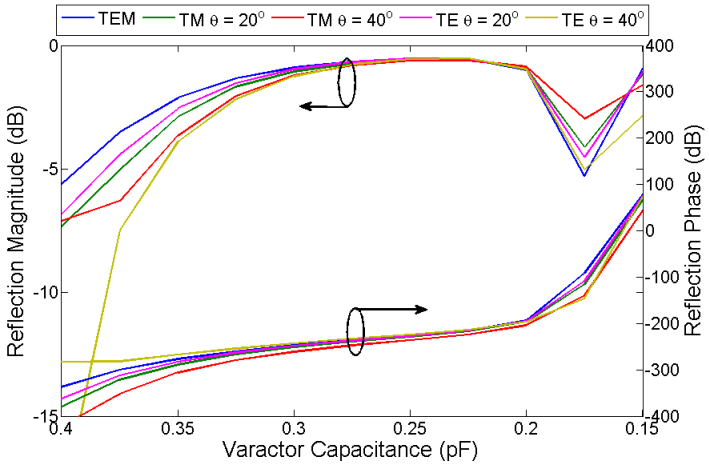

Figure 3.17: Reflection magnitude and phase versus varactor capacitance at 10.3 GHz for varying incident angles using Floquet analysis in HFSS.

To understand the effects of incidence angles on the reflection properties of the unit cell, Floquet analysis is used. HFSS simulations employing master-slave boundaries are used to extract the reflection properties from incidence angles up to $40^o$for both TE and TM polarizations which are then compared to normal incidence. Fig. 3.17 shows the reflection magnitude and phase at 10.3 GHz versus the varactor capacitance. It is observed that the loss of the cross element when excited by either TE or TM waves increases as the angle of incidence increases. However, the loss of the ring element does not change significantly for TE waves and decreases when excited by TM waves. The reflection phase is less sensitive to the angle of incidence than the reflection magnitude, and changes very little except for when the varactors are tuned to 0.4 pF. Similar to the results shown in Fig. 3.16, 360^ophase range is available between 0.15 – 0.35 pF for all cases except the TE polarization with 40^oincidence, which only shows 341^owithin this capacitance range.

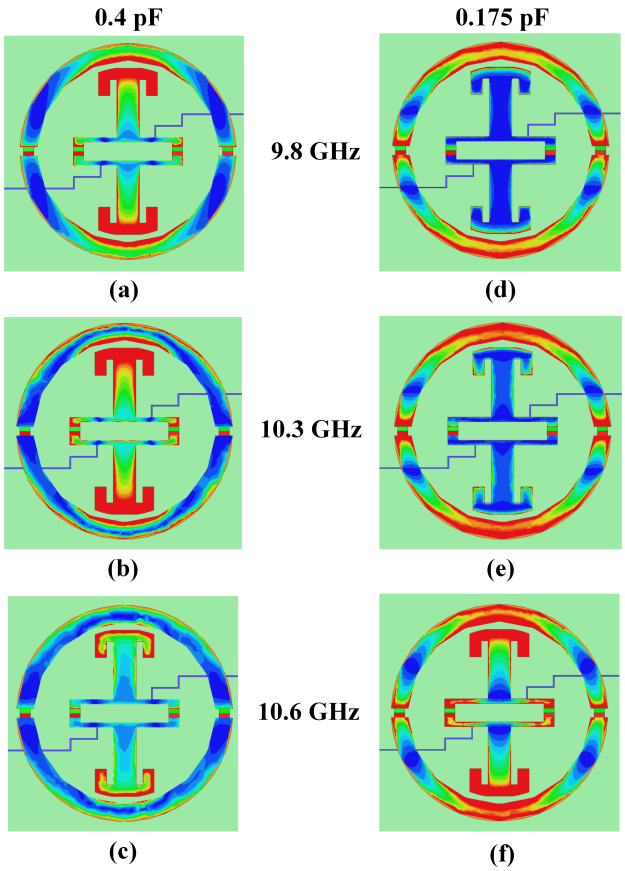

Figure 3.18: The E-field of both ring and cross elements at (a) 9.8 GHz, (b) 10.3 GHz, (c) 10.6 GHz when the varactors are tuned to 0.4 pF; at (d) 9.8 GHz, (e) 10.3 GHz, (f) 10.6 GHz when the varactors are tuned to 0.175 pF.

The DC biasing network for the varactors should exhibit minimal effects on the performance of the reflectarray element. In this design, 50-μm-wide copper lines are placed at the E_{min}, of both ring and cross elements. It should be noted that copper lines are used instead of highly-resistive chromium in order to reduce the fabrication complexity. The biasing lines connect to vias that are drilled through the substrate, moving the biasing network behind the ground plane, which makes large array designs convenient.

The E_{min}, points on both ring and cross elements shift versus the resonant frequency. In order to optmize the tapping locations of bias lines, the E-field magnitudes at the extremes of the varactor tuning range, 0.175 and 0.4 pF, and each at three frequencies, 9.8, 10.3, and 10.6 GHz, are plotted in Fig. 3.18. From the studies shown in Section III (d), the E_{min}, tapping points at 0.4 pF are the most important as the peak loss of the upper resonance occurs at this capacitance. From Fig. 3.18, the biasing lines are accuratley placed at the E_{min}, of both ring and cross elements at all three frequencies when the varactors are tuned to 0.4 pF. When the varactors are tuned to 0.175 pF, the biasing lines on the ring are still accuratly placed at its E_{min}, points for all three frequencies. Though the E_{min}, points of the cross element shift slightly at 10.6 GHz, the upper resonace is much higher than the operating frequency of the reflectarray unit cell. Therefore, its effect on the unit cell performance is minimal.

Using a straight biasing line from the E_{min}, of the cross to that of the ring might interfere with the mushroom structure when using large values of L_1or W2. Thus the biasing line is meandered in the H-plane to the edge of the cross element before moving to the E_{min}, of the ring element. Additionally, the biasing network was found to have an undesirable resonance near the operating frequency when a straight segment was used to connect ring and cross elements. Meandering the biasing line removed this resonance.

Fig. 3.16 shows the phase and loss response with and without the biasing network at 10.3 GHz when the varactors are tuned. The most significant deviation between the two cases is at 0.4 pF where the biasing network introduces 0.52 dB loss. However, for all other capacitance values, the biasing network adds less than 0.1 dB loss. On average, the biasing network only adds 0.12 dB loss and introduces 5.8^{o}phase deviation. The cross polarization levels at 10.3 GHz for all varactor capacitances are better than -20 dB and are not shown in Fig. 3.16 for the sake of brevity. Furthermore, the dual-resonant unit cell was used to simulate a 7$\times$7 reflectarray to verify its cross-pol. level. Though the biasing network is asymetric in the E- and H-planes, it was found that the

7×7 reflectarray has a cross-pol level of -23 dB when the beam is pointed to the boresight.

3.5 Fabrication and Measurement Results

3.5.1 Fabrication and Measurement Methodology

The dual-resonant reflectarray element is fabricated on a 1.27-mm-thick Rogers Duroid 6010 (ε_r =10.2, tanδ = 0.0023) substrate. This substrate is chosen for its high dielectric constant, tight thickness tolerance, and good thermal mechanical stability. First, one side of the substrate is etched to remove the original copper cladding. Then a copper seed layer is deposited using electron beam deposition. After defining the features using photolithography, the sample is placed in an electroplating solution and 10 μm of copper is grown. The seed layer is then etched away, the substrate is diced, and the biasing wires and varactors are soldered on.

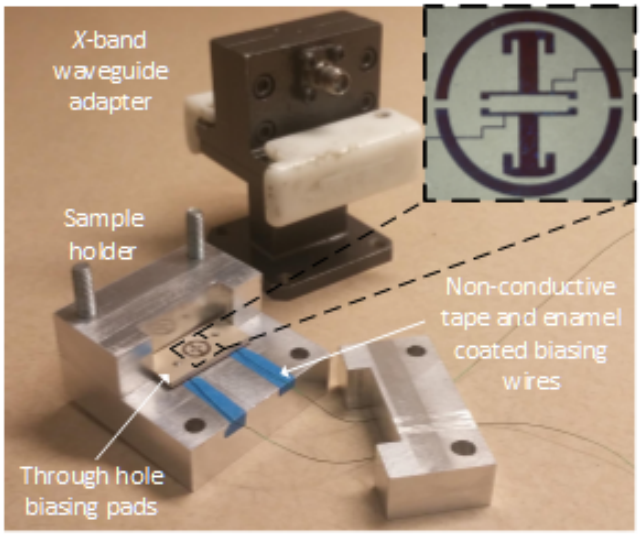

Figure 3.19: Measurement setup showing the fabricated dual-resonant unit cell with biasing wires, sample holder, and the waveguide adapter

The dual-resonant element is measured using an X-band waveguide mounted to a substrate holder

as shown in Fig. 3.19 where the reference plane is calibrated to the surface of the sample. Even though the bias wires are coated in enamel, small strips of non-conductive tape are used to isolate the biasing wires between the ground plane and the waveguide wall section.

3.5.2 Measurement Results

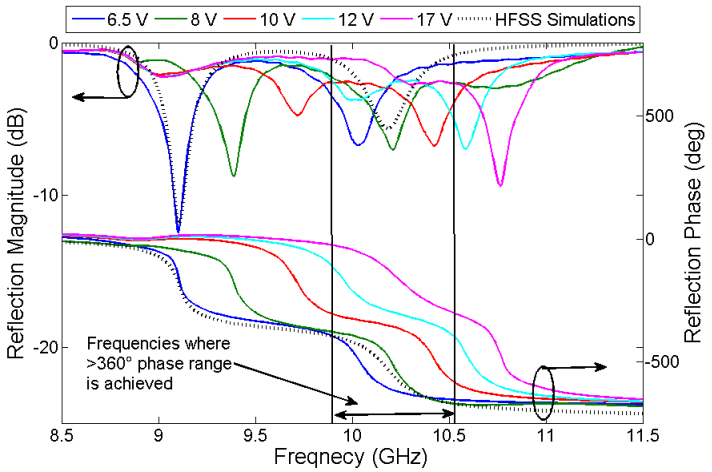

Figure 3.20: Measured reflection magnitude and phase versus frequency for various bias voltages and compared to HFSS simulations when the varactor are tuned to 0.4 pF.

The measured and simulated loss and phase responses when the varactors are set to 0.4 pF are shown in Fig. 3.20. The agreement between simulation and measurement for the lower resonance is excellent. There is a slight frequency deviation (2.5%) for the upper resonance. The measured loss at the upper resonance is 0.9 dB greater than the simulated value. The measured phase slopes of both resonances are well matched with simulations even with the frequency shift at the upper resonance.

Fig. 3.20 shows the measured loss and phase responses as the biasing voltage is increased from 6.5 to 16 V, corresponding to a capacitance range of 0.4-0.15 pF. As shown in Fig. 3.20, the loss of the upper resonance is held constant for most of the tuning range and increases at the upper tuning

limit, while the loss of the lower resonance is greatly reduced as the biasing voltage is increased. This measurement result is consistent with the simulation results in Fig. 3.15. From the phase response, both resonances are clearly over-coupled for the entire tuning range.

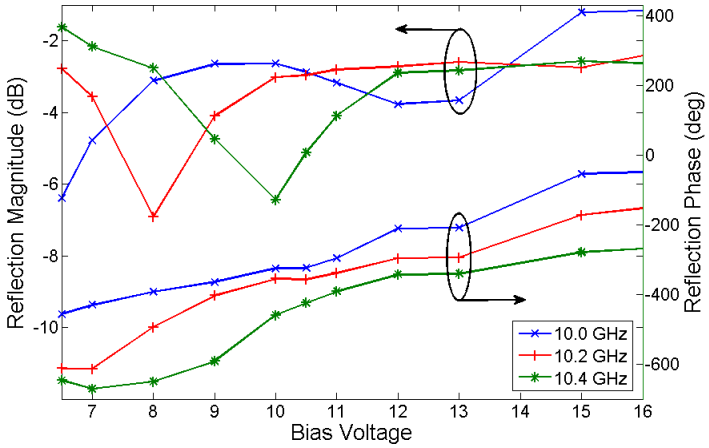

Figure 3.21: Measured reflection magnitude and phase at 10.0, 10.2 and 10.4 GHz as the bias voltage is adjusted.

3.21 shows the measured loss and phase responses at three frequencies, 10.0, 10.2, and 10.4 GHz, as the biasing voltage is varied. The phase range at 10.0, 10.2, and 10.4 GHz is 402^o, 440.2^o, and 367.6^o, while the peak loss is 6.39, 6.91, and 6.43 dB and the average loss is 3.22, 3.29, and 3.62 dB, respectively. When the bias voltage is varied from 7 (0.35pF) to 16 V (0.15 pF), the phase range at 10.0 GHz is reduced to 375^owhile the phase range at 10.2 and 10.4 GHz is increased to $440.6^o$and 391.8^orespectively. With this biasing range, the peak loss at 10.0, 10.2, and 10.4 GHz is 4.78, 6.91, and 6.43 dB, while the average loss is 3.09, 3.49, and 3.73 dB, respectively.

The frequency dependency of the phase of the reflection coefficient (Ψ) varies at each biasing voltage. By taking the absolute difference between Ψ at a given frequency and Ψ at the operating frequency for each biasing voltage, a phase variation curve as a function of the biasing voltage is defined. The difference between the maximum and minimum of this curve gives the maximum

relative phase variation, e_{max} 3.3 between two reflectarray elements.

$$e_{max} = \max_{V_R} |\Psi(f) - \Psi(f_o)| - \min_{V_R} |\Psi(f) - \Psi(f_o)| \tag{3.3}$$

This measurement can be used to evaluate the bandwidth performance of the dual-resonant reflectarray unit cell [78] and is shown in 3.22 for the simulated and measured unit cells at their respective operating frequencies. The simulated and measured bandwidth where emax $\leq 22.5^o$is 175 (1.7%) and 162 MHz (1.62%), respectively.

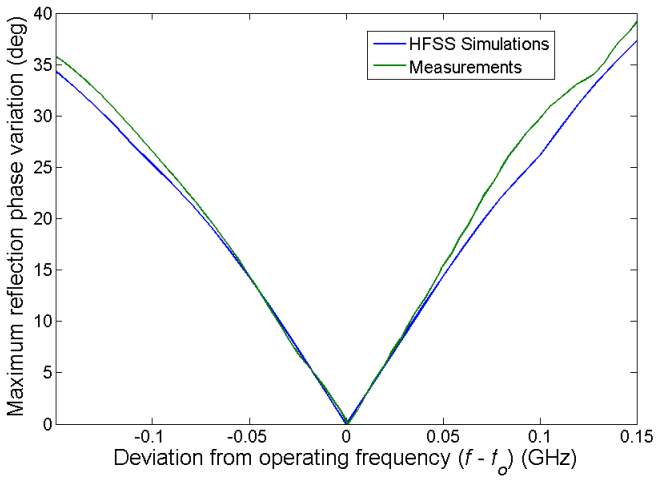

Figure 3.22: Comparison of measured and simulated element phase bandwidth

Table 3.2: Comparison of Reconfigurable Recflectarray Unit Cell Designs

	This work	[64]	[90]	[77]	[82]	[84]
Tuning Technology	Varactor	LC	Varactor	Varactors	BST	MEMS
# of Tuning Elements	4	1 dist.	6	2	1 dist.	4
Phase Tuning type	Cont.	N/A	Cont.	Cont.	Cont.	Discrete
Phase Range	375°	400°	380°	320.2°	250°	1°/180°
Tuning voltage	7-16V	N/A	2-20V	0-30V	0-400V	0/80V
Operating Frequency	10 GHz	10 GHz	5.5 GHz	5.5 GHz	10.3 GHz	11.2
Peak Loss	4.78 dB	4.7 dB	3.5 dB	3.5 dB	5.8 dB	1.4
Average Loss	3.09 dB	N/A	N/A	N/A	N/A	0.6 dB

Table 3.2 shows the comparison to five other reconfigurable reflectarray unit cell designs, utilizing LC [64], varactor [77], [90], BST [82], and MEMS [84] tuners. The unit cell presented in this chapter compares favorably in most categories with those listed in Table 3.2. It should be noted that the unit cell presented in [64] uses three non-tunable unit cells to emulate reconfigurability. Therefore, the loss performance is expected to degrade with actual tuners in place.

The presented unit cell is designed for a single linear polarization. However, the design was recently extended to support dual polarization using simulations [95]. In that chapter, special care was taken to ensure symmetry in the horizontal and vertical planes to reduce the cross-polarization response. While limited to simulations, the design showed cross polarization levels lower than -30 dB while maintaining 360^ophase range and similar losses to the design presented in this work.

3.6 Discussion

A tunable dual-resonant reflectarray unit cell has been designed, simulated and fabricated at X band. An equivalent circuit was developed and verified by full-wave simulations. The operational theory and design procedure are described showing how to minimize loss and phase sensitivity while achieving a continuous phase range in excess of 360^o. A dual-resonant unit cell composed of a ring and cross element demonstrated a phase range of $375^o$with an average loss of 3.09 dB at 10.0 GHz.

This research on tunable antenna elements is necessary to realize high-performance electronically beamsteerable reflectarrays with low loss, small phase error, and higher gain. However, the array performance hasn't been evaluated. Additionally the waveguide inter-element spacing required the use of a non-ideal substrate, causing the loss performance to suffer. In the next chapter the unit cell is re-designed for proper array spacing, the loss performance is enhanced and a novel genetic algorithm is developed to enable accurate biasing voltages across the entire aperture.

CHAPTER 4: DUAL-RESONANCE CONTINUOUSLY BEAM-SCANNING *X*-BAND REFLECTARRAY

In this chapter, a 7×7 reconfigurable reflectarray operating at *X* band is proposed and experimentally verified. This chapter re-designs the previously presented unit cell to optimize its performance for array dimensions. The reflectarray consists of linearly-polarized, dual-resonance, tunable unit cells fabricated on a single layer. Reconfigurability is achieved by loading each dual-resonance unit cell with four varactors; the two resonances provide a phase range greater than 360^o. The unit cell design utilized in this reflectarray is analyzed using full-wave floquet simulations. A biasing network supporting individual biasing of each array element is designed, allowing beamsteering in E-, H-, and diagonal planes. The proposed reflectarray is evaluated using both full-wave simulations and measurements. To facilitate measurements, a fused filament deposition 3-D printer is used to fabricate an antenna mounting fixture using micrometer stages to make fine adjustments for the final alignment. A measured gain of 15.03 dBi, 3-dB gain fractional bandwidth of 7.81%, and continuous beam scanning are demonstrated in multiple planes from -50^o to +50^o at 10.1 GHz.

4.1 Introduction

Reconfigurable reflectarrays have become a source of significant interest as viable replacements for reflector antennas and phased-arrays in both wireless communications and radar applications [86]. Reflectarrays consist of a planar array illuminated by a separate feed. Each array element scatters the incident waves with a specific phase shift to compensate for different spatial lengths from the feed to create coherent radiation in a desired direction. Reflectarrays tend to be lighter, less expensive, and have lower profiles than parabolic reflectors but suffer from narrow bandwidths [9], [96]. Several techniques have been used to improve the bandwidth of reflectarrays such as the

use of true-time delay array elements [21], [97] or by using multiple resonators that are stacked on separate layers [98] or arranged concentrically on a single layer [46].

Significant work has been undertaken to enable phase reconfigurability in the array elements. Compared to phased arrays, reconfigurable reflectarrays avoid the need for discrete phase shifters and expensive transmit/receive (T/R) modules by loading the array elements with tuning devices. Additionally, the cost of development and the low efficiency due to the losses of the feeding network of traditional phased arrays are avoided through the use of spatial feeding. Furthermore, the low weight and ease of deployability inherent to the reflectarray design makes it ideal for space applications [99].

Several methods to enable reconfigurability in reflectarray elements have been investigated. In [100], beam scanning was achieved by mechanically moving the feed, resulting in very limited scan angles. Another approach involves mechanically rotating or linearly displacing the array elements to achieve the desired reflection phase [62], [63]. This method greatly reduces the loss of the array element while providing large phase ranges but exhibits slow scanning speed and significantly complicates the fabrication of the array.

Alternatively, beamsteering can be realized through the use of electronically reconfigurable array elements and many techniques and technologies to design the elements have been investigated [86]. The technologies used to realize beam scanning can be broadly categorized as either discrete or analog. In practical designs, discrete tuning is desirable for several reasons: discrete devices such as micro-electro-mechanical systems (MEMS) [80] and PIN diodes [79] typically have lower losses, stable phase states, and simple biasing networks. However, discrete tuning introduces quantization errors which increase sidelobe levels (SLL) [79], [47] and reduce reflectarray directivity [79], [23]. In [22], a 10×10 beam switching reflectarray was demonstrated utilizing MEMS tuning devices. While this array was not capable of continuous beam scanning, it demonstrated beam

switching in the H-plane between broadside and 40°. Multi-bit designs can significantly reduce quantization error but they complicate the biasing network and introduce additional loss.

Analog phase control is capable of avoiding quantization errors but accurate control of biasing voltages is difficult. Barium Strontium Titanate (BST) [82] is continuously tunable, demonstrates very quick tuning speeds, and is capable of high power handling. However, BST exhibits a high loss tangent and its limited tuning range introduces additional loss in reflectarray antennas [83]. Graphene [101] and liquid crystal (LC) [102], [103] have been used to design continuously tunable reconfigurable reflectarrays at millimeter and sub-millimeter wavelengths but are not suited to designs at lower frequencies due to high losses [88], [89]. The array presented in [104] was tuned by varactors and demonstrated continuous beam scanning up to 40^o but suffered from poor aperture efficiency.

The aperture efficiency of practical reconfigurable reflectarrays is typically very low. The arrays presented in [79], [22], [89], and [104] demonstrated efficiencies of 17.9%, 7.85%, 18.5%, and 3.1%, respectively. The efficiencies of these arrays are low due to either the quantization loss or high array element loss. The loss and phase performance of the chosen array element are the most critical parameters for the overall array performance when utilizing analog phase control. Ideally, the array element should exhibit a phase range of at least 360^o with low loss and proper phase slope. A limited phase range will reduce beam-scanning performance and a large phase slope will degrade bandwidth performance. In [105], a phase-agile, dual-resonant unit cell and its equivalent circuit were recently demonstrated. A dual-polarized version of this array element was investigated in [95] with simulations results only.

In this chapter, a reflectarray antenna with improved electrical performance and aperture efficiency over previously-reported varactor-based reflectarrays is designed, fabricated and measured at X band. Although a similar array element was presented in [105], its performance was only evaluated

at the unit cell level and was not integrated into an array. Additionally, the loss performance was limited by the constraints of the X-band waveguide dimensions; the research presented herein improves upon the loss and phase slope performance of such array element. Furthermore, a unique genetic algorithm is developed to optimize individual biasing voltages for radiation in the desired scan angle and the biasing network required to facilitate full array measurements is demonstrated.

4.2 Reflectarray Element Analysis

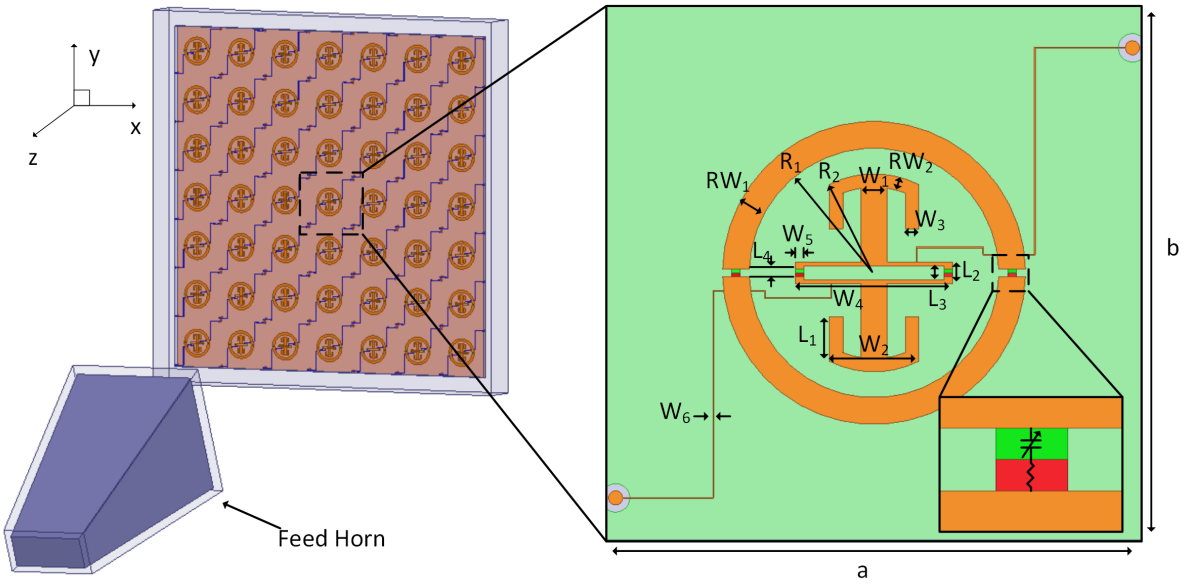

Figure 4.1: Schematic of the 7×7 reflectarray and its cross/ring dual-resonant array element.

In this section, the design of the dual-resonance array element is presented. The varactor-loaded dual-resonant unit cell developed in [105] is chosen as the array element and is depicted in Fig. 4.1. The dimensions shown in 4.1 are as follows: *($a = b = 13.35$ mm, $RW_1 = 750$ μm, $RW_2 = 375$ μm, $R_1 = 3.5$ mm, $R_2 = 2.78$ mm, $W_1 = 750$ μm, $W_2 = 2.5$ mm, $W_3 = 375$ μm, $W_4 = 4.4$ mm, $W_5 = 228$ μm, $W_6 = 25$ μm, $L_1 = 1.25$ mm, $L_2 = 600$ μm, $L_3 = 400$ μm, $L_4 = 200$ μm, Substrate thickness $h = 1524$ μm).* The unit cell consists of an outer ring element with a central cross element,

each loaded with two varactors. The varactors (MACOM MA46580-1209) were chosen for their high capacitance tuning ratio and high quality (Q) factor. The cross element has been loaded with a mushroom structure as shown in Fig. 4.1. This mushroom structure allows for the physical spacing between the ring and cross, $R_1 - R_2$, to be controlled without changing the resonant frequency of the cross element. This enables control of the mutual coupling between the two elements which is critical for the performance of the dual-resonant array element. It is important to note that the measurements reported in [105] were based on simulations using an X-band waveguide (a = 22.86 mm, b = 10.16 mm). As such, in this work, the array element is re-designed using the inter-element spacing in the 7×7 array.

4.2.1 Initial Design Analysis

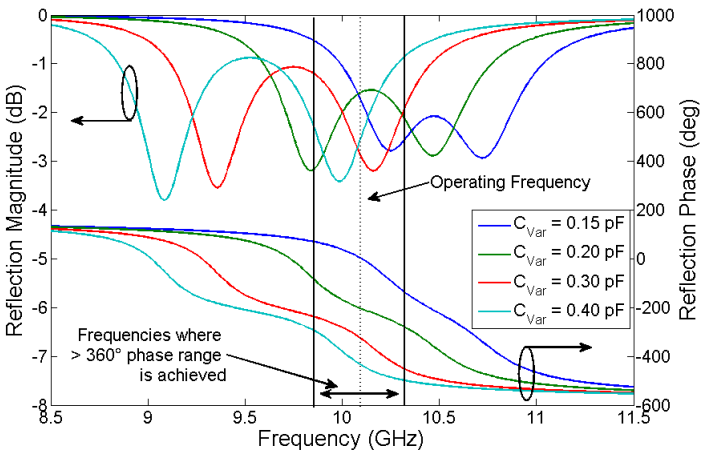

Figure 4.2: Reflection magnitude and phase of dual-resonant unit cell shown in Fig. 4.1 when excited at normal incidence and simulated in HFSS as the varactor capacitance is tuned.

The initial design of the array element is performed for a normal incidence angle using a parallel-plate TEM waveguide with a fixed inter-element spacing of a = b = 13.35 mm ($0.45\lambda_o$) in ANSYS High-Frequency Structure Simulator (HFSS). Rogers Duroid 6002 (ϵ_r = 2.94, tanδ = 0.0012) is

chosen as the substrate. The array element is designed following the procedure laid out in [105] with an operating frequency of 10.1 GHz. The reflection magnitude and phase due to excitation from a normal incidence are shown in Fig. 4.2 for several varactor capacitances. Both resonances are over-coupled over the entire varactor tuning range and the mutual coupling between each resonance remains mostly constant. The element shows greater than 360^o continuous phase range from 9.85 to 10.35 GHz with 437^o phase range at the operating frequency of 10.1 GHz.

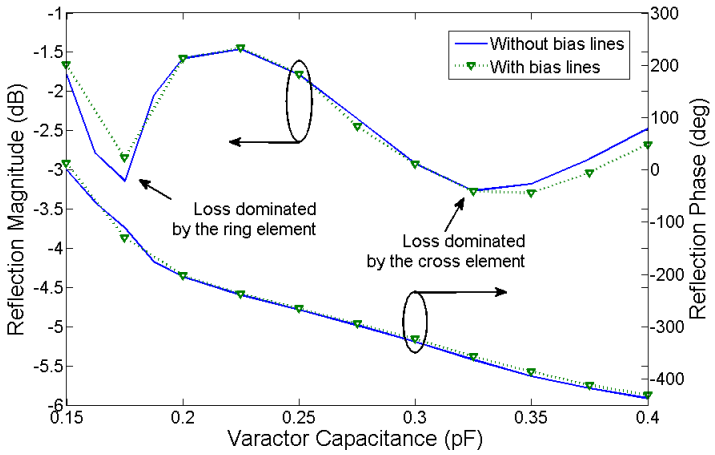

Figure 4.3: Simulated reflection magnitude and phase of the dual-resonant unit cell when excited at normal incidence versus varactor capacitance with and without the biasing network at 10.1 GHz.

The resulting S-curves showing the variation of reflection magnitude and phase versus varactor capacitance at 10.1 GHz are shown in Fig. 4.3. The array element loss varies from 1.45 to 3.28 dB with an average loss of 2.41 dB. This represents a 1.5- and 0.68-dB improvement in the peak and average loss performance, respectively, as compared to the array element presented in [105]. This improvement is due in large part to the reduced dielectric constant of the substrate from 10.2 [105] to 2.94, which allows for the use of thicker substrate to achieve the same mutual coupling level. Therefore, both ring/cross elements exhibit smaller Q_{rad} and lower loss [105], [41]. The higher dielectric constant in [105] was necessary due to the smaller inter-element spacing set by the X-band waveguide. The two peaks in loss at 0.175 and 0.325 pF occur due to the ring and cross

elements respectively, resonating at 10.1 GHz. While the maximum phase range is well over 360°, the phase response shown in Fig. 4.3 is also very linear from 0.2 to 0.4 pF, which will improve the bandwidth performance.

4.2.2 Angle of Incidence

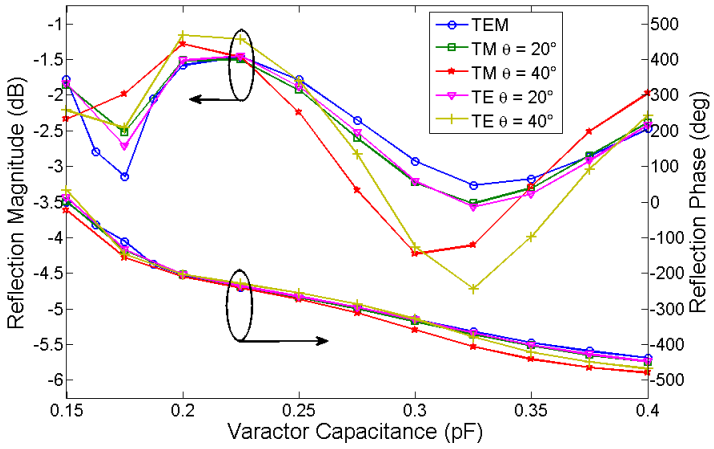

Figure 4.4: Simulated reflection magnitude and phase of the dual-resonant unit cell versus varactor capacitance at 10.1 GHz for varying incident angles using Floquet analysis.

In practical designs, reflectarray elements are not always excited by normal incident waves. Thus, it is necessary to evaluate the performance of the array element when illuminated by oblique angles of incidence. To quantify these effects, Floquet analysis is used with HFSS simulations employing master-slave boundaries. Angles of incidence up to 40^o for both TM and TE polarizations are simulated and compared to normal incidence in Fig. 4.4. The TM and TE polarizations simulate array elements that lie on the E- and H-planes respectively. Similar to Fig. 4.3, the increased losses at 0.175 and 0.325 pF are due to the ring and cross elements respectively. From Fig. 4.4, the array element performs similarly whether excited by either TM or TE waves. When the angle of incidence is increased, the loss of the cross element increases; this increase is less than 0.3 dB

at angles under 20°. However, when the angle of incidence increases to 40°, the loss of the cross increases by 1.5 and 1 dB when excited by TE and TM waves respectively. Conversely, the loss of the ring resonance for both TE and TM waves is less than that for TEM waves and decreases as the angle of incidence increases. The variation of the phase response is also shown in Fig. 4.4. The reflected phase varies very little for either illumination. Overall, incident angles up to 40^o in the H- and E-planes increase the average loss by less than 0.28 and 0.18 dB, respectively, while causing less than 25^o phase variation on average.

4.2.3 Biasing Network

The DC biasing network required by each array element must exhibit minimal effects on its reflection properties. While it would be desirable to design the biasing network with a quarter-wavelength-long bias tee, the available space, especially between the ring and cross elements, is limited. Instead, 25-μm-wide copper lines are placed at the electric field minimum (E_{min}) point on both ring and cross elements. The biasing lines then connect to vias as shown in Fig. 4.1. This allows for all biasing wires used in the array to be placed behind the ground plane, making large array designs with individual element biasing convenient.

The E_{min}, points for both elements slightly change as the varactors are tuned. However, an optimum choice of the E_{min}, points can be made to ensure minimal adverse effects from the feeding lines [105]. The biasing lines between the ring and cross elements are meandered to move the biasing line away from the horizontal arm of the cross denoted by W_4 to avoid significantly affecting the loss of the cross resonance. The biasing structure also introduces a third undesired, under-coupled resonance. However, by moving the vias to the edge of the inter-element spacing, thus making the biasing arms longer, the third resonance is moved out of band.

From Fig. 4.3, the worst case performance occurs at 0.4 pF where the biasing network adds 0.2-dB

loss and causes a phase deviation of 6°. However, on average, the biasing network introduces less than 0.02 dB of loss and less than 4^o of phase deviation.

4.3 Array Design and Dimulations

To demonstrate the effectiveness of the proposed array element, a 7×7 array is designed. The inter-element spacing is set to 0.45 λ_o × 0.45 λ_o at the operating frequency 10.1 GHz and the aperture is illuminated by a pyramidal X-band standard gain horn antenna with a 46 × 46 mm aperture. In this section, the aperture efficiency and feed location will be discussed and then the reflectarray simulation setup and results will be presented.

4.3.1 Apeture Efficiency

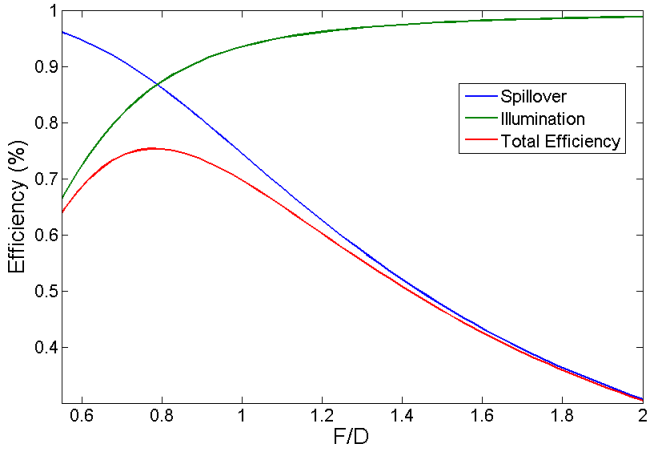

Figure 4.5: Calculated aperture efficiencies for varying feed horn distances with a 15-dBi gain horn offset by 25°.

In conventional reflectarray designs, the aperture efficiency can be optimized by choosing the feed location relative to the dimension of the aperture f/D to balance the spillover efficiency,

illumination efficiency, and feed blockage [106]. Compared to large reflectarrays, the effects of feed blockage is much more pronounced on smaller designs. The small size of the array presented here (3.15 $\times$ 3.15 $\lambda_o{}^2$) necessitates a large offset feed angle to minimize these effects. While offsetting the feed by less than 30^odoes not significantly reduce the aperture efficiency [106], it increases the angle of incidence especially for the edge elements. Fig. 4.5 shows the illumination and spillover efficiencies for an aperture fed by a 15-dBi horn antenna with 25^ooffset angle in the E-plane. As the feed is moved away from the aperture, each element is equally illuminated, increasing the illumination efficiency. However, increasing the f/D decreases the spillover efficiency, which is the ratio between the energy emitted by the feed and the energy incident on the array. The total aperture efficiency is the product of both illumination and spillover efficiencies. To maximize the aperture efficiency, the feed distance is chosen as f/D = 0.85. It should be noted that moving the feed horn closer also increases the angle of incidence. The chosen feed position produces an aperture efficiency of 74% with a maximum incidence angle of 35°.

4.3.2 Array Analysis Using Full-Wave Simulations

The simulated 7×7 reflectarray is shown in Fig. 4.1. From array theory, the phase shift required for each element with coordinates (m, n) to achieve a beam scan angle of (θ_b , ϕ_b) can be calculated as **Ineq3**. For the simulation and analysis of the array, the required capacitances are extracted from the phase curves shown in Fig. 4.3 using **Ineq3**. The array simulation setup in HFSS is shown in Fig. 4.1 where finite element boundary integral (FEBI) boundary conditions are used. The use of FEBI boundaries allows for a radiation boundary to be defined around the feed and array separately. The structures inside the FEBI boundaries are analyzed using the Finite Element Method (FEM) while the interactions between the boundaries are analyzed using boundary integrals. This significantly reduces the simulation complexity and computer memory requirements compared to standard radiation boundaries.

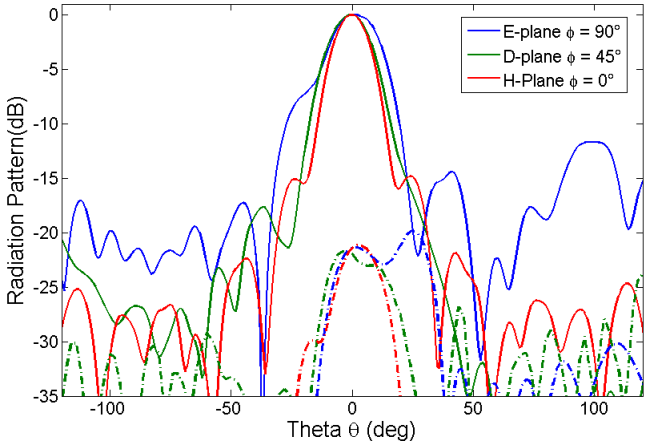

Figure 4.6: Normalized radiation patterns in three planes simulated in HFSS. The co- and cross-polarization patterns are represented by solid and dashed lines respectively.

Fig. 4.6 shows the normalized radiation patterns for the boresight case in three planes: the E-, H-, and a diagonal plane where $\phi = 45°$. The sidelobes in all three planes are below -15 dB with the exception of a peak in the E-plane at 90°. The cross-polarization patterns peak at boresight in all three planes with similarly-shaped lobes. All cross-polarization levels are below -21 dB relative to the main beams. Figs. 4.7, 4.8 and 4.9 show the normalized radiation patterns for H-plane, diagonal plane, and E-plane, respectively, when the beam is scanned up to +50°. Scanning to negative angles in the H-plane is not shown as the array is symmetric in this plane. The beam cannot be scanned to negative angles in the E-plane due to the feed blockage.

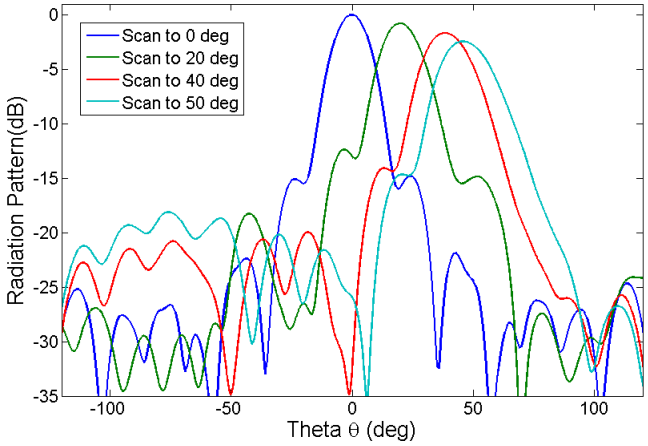

Figure 4.7: Normalized H-Plane radiation patterns for different scan angles using HFSS simulations.

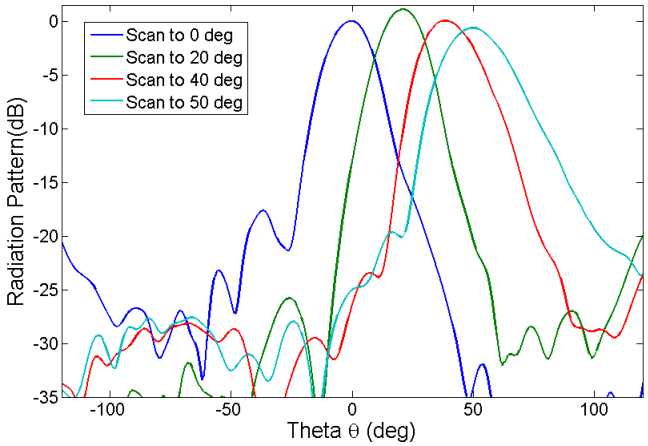

Figure 4.8: Normalized Diagonal ($\phi = 45°$) plane radiation patterns for different scan angles using HFSS simulations.

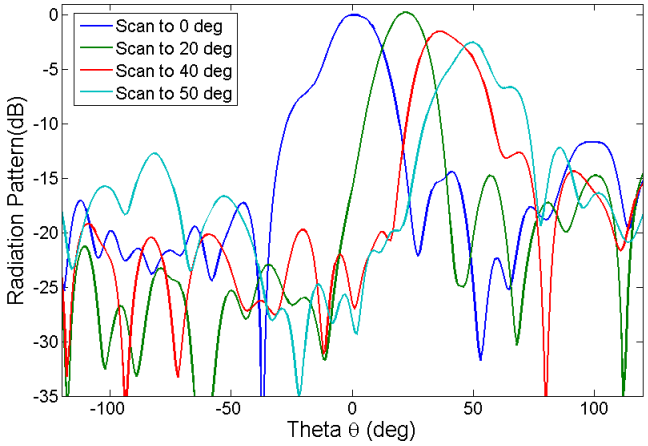

Figure 4.9: Normalized E-plane radiation patterns for different scan angles using HFSS simulations.

In Fig. 4.7, SLLs are more than 12 dB below the main beam in all scan cases while the SSLs slightly increase as the beam is scanned to large angles. As the beam is scanned to large angles, the half power beam width (HPBW) increases and the main beam suffers from scan loss. For the maximum scan angle of 50°, the scan loss is 2.46 dB. In Fig. 4.8, the effects of the feed image lobe from the ground plane can be observed when the beam is scanned to 20°. The HPBW is wider when scanned to 50^oin the diagonal plane than when scanned to 50^oin the H-plane. While the sidelobes of the radiation pattern in the E-plane are all more than 12 dB below the main beam, they are also higher on average than in either H- or diagonal planes.

4.4 Fabrication and Measurements

4.4.1 Fabrication Procedure and Measurement Setup

Due to the limited size of the photolithography equipment, the 7×7 reflectarray is fabricated in several 3×3 sub-arrays. First, the original copper cladding on one side of the substrate is etched away

before using electron-beam (E-Beam) deposition to evaporate a copper seed layer. Photolithography is then used to define the array element and its biasing network on one layer. Then pulsed electroplating is used to grow 10 μm of copper. The seed layer is then etched away; the substrate is diced; and the varactors and biasing wires are soldered on. Once the biasing wires are soldered, the array is mounted on a test fixture.

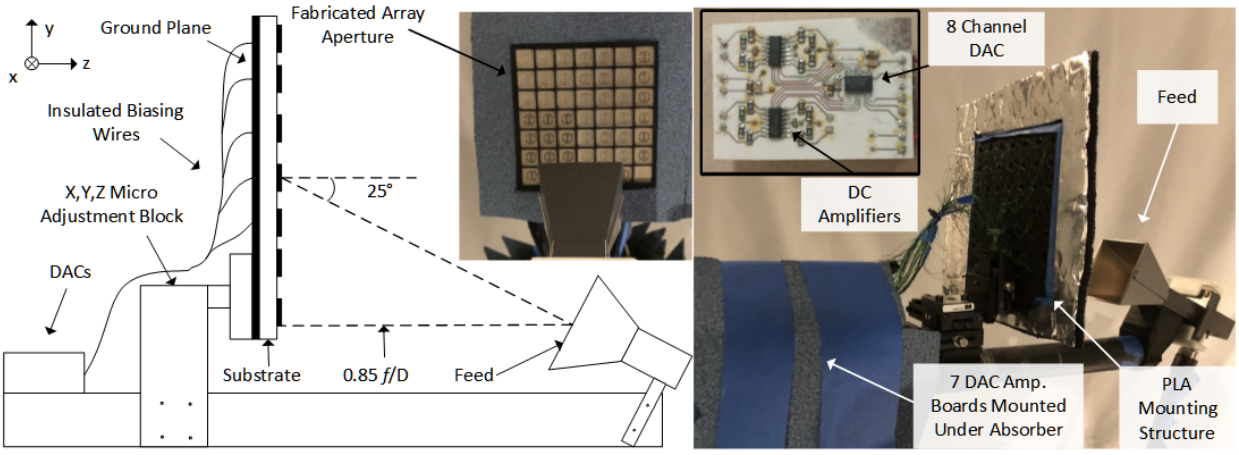

Figure 4.10: Fabricated 7×7 reflectarray and measurement setup showing the feed, supporting structures and biasing

The measurement setup including the array, feed, biasing lines, and the support structures are shown in Fig. 4.10. All the supporting structures used in the measurement setup are fabricated by a 3D printer using polylactic acid (PLA). Solid PLA has been reported to possess a dielectric constant of 2.3 [107]. However, the dielectric constant of structures made of PLA will heavily depend on the density of the structure as most 3D printed parts are partially hollow. As shown in Fig. 4.10, the feed horn is rigidly fixed to the measurement structure to ensure a consistent offset angle. To enable the accurate positioning of the reflectarray aperture relative to the feed, the array mounting structure is attached to three linear micrometers. These micrometers allow for ±13 mm travel with a 400 μm/turn resolution. The biasing voltages are provided by seven 10-bit,

8-channel DAC modules mounted behind the reflectarray as shown in Fig. 4.10. Each module uses a MAX5592 DAC in conjunction with a DC amplifier to generate up to 20 volts to bias each array element. A standard anechoic chamber using a far-field setup is used to measure the reflectarray.

4.4.2 Genetic Algorithm

One of the major challenges to use array elements with analog phase control is finding the optimal voltages to achieve maximum gain in the desired direction. Using the extracted reflection phase from Fig. 4.3 and the required phases calculated from **Ineq3**, it is possible to calculate the required capacitances and therefore voltages for each array element. However, due to fabrication tolerances, non-uniform varactors and potential alignment issues, the calculated voltages might not be the exact optimal values. A custom genetic algorithm (GA) was used to solve for the optimal bias voltages that result in maximum gain in any desired direction.

The genetic algorithm uses a population of individuals where each individual consists of 49 voltages. In each generation, all of the individuals in the population are tested and evaluated by measuring the gain. The lowest scoring 40% of the population is replaced by a random set of voltages; the highest scoring 2% of the population are directly copied over to the next generation; the remaining 58% of the population reproduce and combine in a controlled manner as shown in Fig. 4.11. When two individuals breed, some of the voltages from each individual will be directly transferred to each child while some voltages will crossover between the two parents. In addition, there is a chance for random mutation of any of the voltages. This algorithm is only capable of searching for a voltage set which results in the peak gain at a single direction, and a single frequency due to the time it would take to mechanically measure multiple scan angles. However, it was found that this resulted in maximum gain and good radiation patterns.

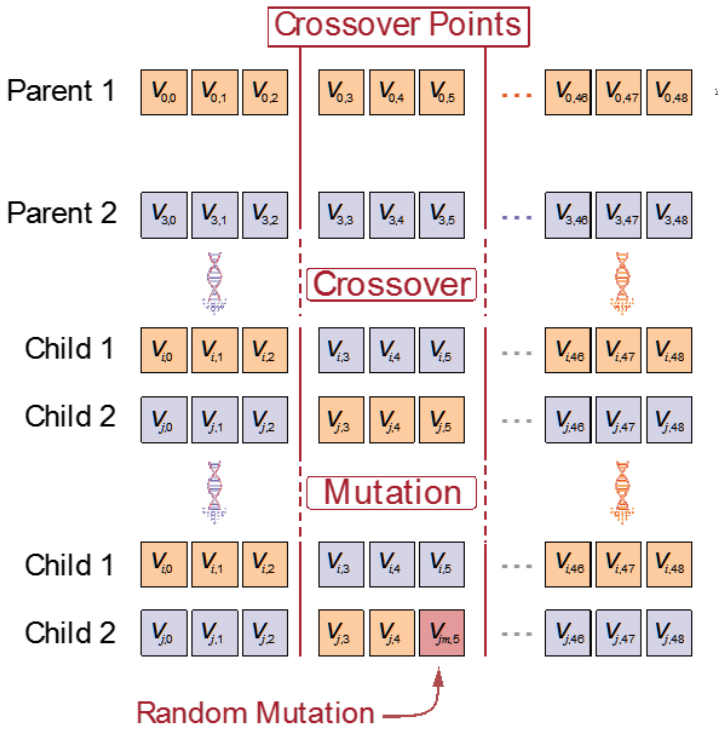

Figure 4.11: Breeding between individuals in each generation of the genetic algorithm.

4.4.3 Measurement Results

Figs. 4.12, 4.13 and 4.14 show the measured radiation patterns for multiple scan angles in the H-, $\phi = 45°$, and E-planes, respectively.

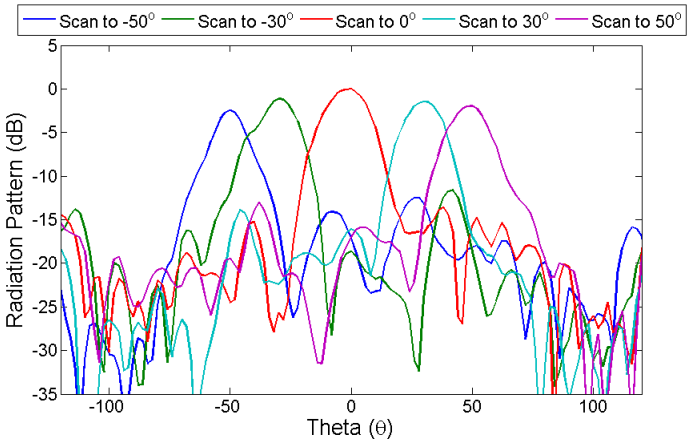

Figure 4.12: Measured H-Plane radiation patterns for different scan angles.

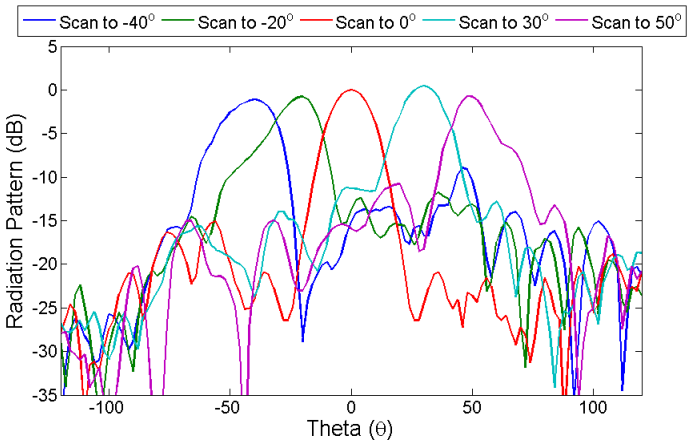

Figure 4.13: Measured Diagonal ($\phi = 45°$) plane radiation patterns for different scan angles.

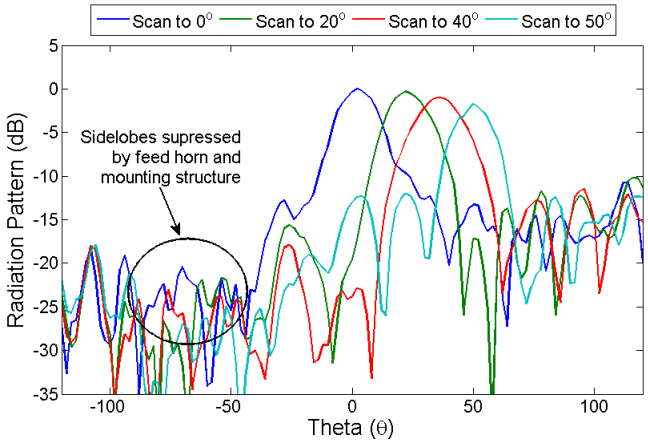

Figure 4.14: Measured E-plane radiation patterns for different scan angles

From Fig. 4.12 it can be seen that the array is capable of beamsteering in the H-plane from -50^o to +50^o where the scan loss is 2.44 and 2.15 dB, respectively. The worst-case SLL is -10.1 dB and occurs when the beam is pointed to -50°. When scanning in the ϕ = 45^o plane, the SLLs are better than -15 dB. Due to a slight occlusion caused by the feed horn in the negative theta, the beamsteering range in the ϕ = 45^o plane is slightly lower than in the H-plane and is scanned from -40^o to +50°. Similar to the H-plane case, the worst-case SLL occurs when the beam is scanned to extreme angles and is -7.9 dB when scanned to -40°. However, for all other scan cases the SLLs are better than -10 dB. In Fig. 4.14 the beam is scanned from 0^o to +50°. The beam cannot be scanned to negative angles due to the feed blockage. The scan loss and worst-case SLL at +50^o is 1.73 and -10.3 dB respectively. In all other scan cases, the SLL is less than -11 dB relative to the main beam.

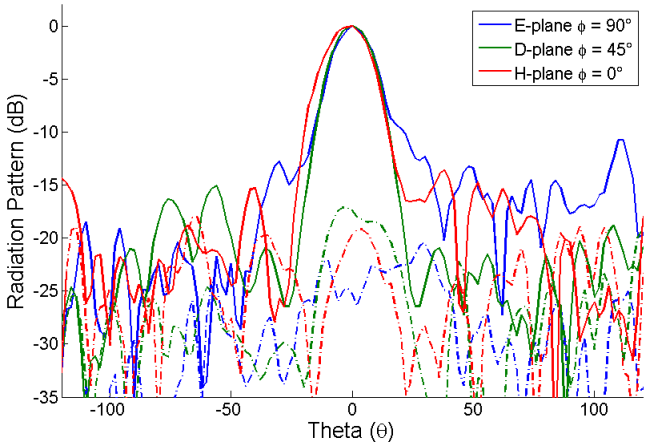

Figure 4.15: Measured radiation patterns in three planes when the main beam is scanned to the boresight. The co- and cross-polarization patterns are represented by solid and dashed lines respectively.

Fig. 4.15 shows the measured co-polarization and cross-polarization radiation patterns for the boresight scan case in all three planes. As expected, a consistent beam width is observed in each plane. The worst-case SLL of -12.7 dB occurs in the E-plane. The worst-case cross-polarization levels occur in the diagonal plane and is -17.4 dB. The peak cross-polarization level in the E-plane is -20.4 dB and occurs at 30^{o}instead of boresight. The cross-polarization levels increase as the beam is scanned to large angles; the cross-polarization levels are below -16 dB for all scan cases and are not shown here for the sake of brevity.

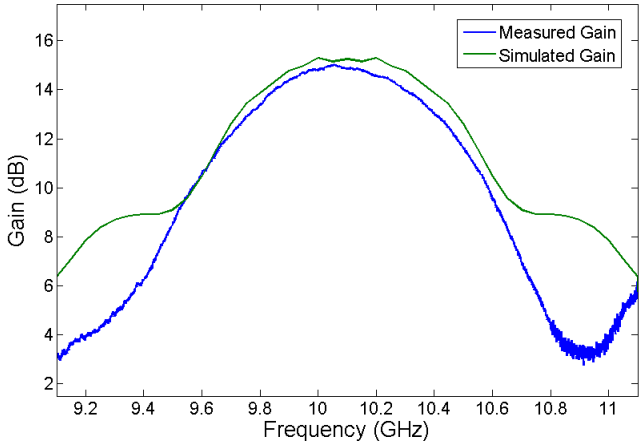

Figure 4.16: Measured radiation patterns in three planes when the main beam is scanned to the boresight. The co- and cross-polarization patterns are represented by solid and dashed lines respectively.

Fig. 4.16 shows the variation of simulated and measured array gain with frequency for the boresight scanning case. The measured gain agrees very well with simulations around the operating frequency. The simulated and measured peak gain is 15.27 and 15.03 dB at 10.1 and 10.05 GHz respectively.

$$\eta = \frac{G}{4\pi A\lambda^2} \tag{4.1}$$

Using the same definition as in [79], the maximum measured total efficiency is 25.42% calculated from 4.1 where A is the aperture area and G is the measured gain The measured 1- and 3-dB gain bandwidths are 4.4% and 7.81% respectively.

Table 4.1 lists the loss budget for the boresight beam at 10.1 GHz. The array element loss varies as the varactors are tuned, as such the average element loss will vary when the beam is scanned. The average element loss in Table 4.1 is calculated based on the reflected phases calculated by **Ineq3** for the boresight case. The relationship between the loss and phase is shown in Fig. 4.3. It should be noted that the difference between measured and calculated losses is due to a few factors: (1) the

Table 4.1: Loss Budget of the Array for the Boresight Case

Directivity (Calculated)	20.96 dBi
Aperture Efficiency (Calculated)	74% (-1.31 dB)
Average Element Loss (Calculated)	2.62 dB
Total Calculated Losses	3.93 dB
Gain (Measured)	15.03 dBi
Measured Losses (Directivity - Gain)	5.96 dB
Total Efficiency	25.42%
Measured - Calculated Losses	2.03 dB

calculated loss does not consider feed blockage; (2) the calculated loss uses the average element loss while the measurement/HFSS exhibits different losses in each element; (3) the calculated loss does not take into account the effect from angle of incidence.

Table 4.2: Comparison of Relevant Designs

	This Design	[82]	[84]	[72]	[93]
Tuning Technology	Varactor	PIN Diode	MEMS	Varactor	Varactor
Beamsteering Type	Continuous	Continuous	Digital	Continuous	Continuous
Beamsteering Capabilities	2-D	1-D	1-D	1-D	1-D
Center frequency.	10.1 GHz	12.5 GHz	26.5 GHz	11.25 GHz	5.8 GHz
Gain	15.01 dBi	17.5 dBi	11.42 dBi	9.30 dBi	12.9
Aperture Size (λ_o^2)	3.15×3.15	5×5	5×5	2.1×10.5	5.8×4.06
Total Efficiency	25.42%	17.9%	7.85%	3.1%	5%
Gain FBW (3-dB)	7.81%	N/A	3.77%	<7%	1.3%
First SLL	-10.1 dB	-5.9 dB	-10 dB	-7 dB	-10 dB
Beamsteering Range	±50°	±50°	0°or 40°	±40°	±50°

The measured performance of the array presented in this work is compared to other reconfigurable reflectarray designs in Table 4.2. The total efficiency and SLL of this design compare favorably with the discretely-tuned arrays [79], [22]. The beamsteering range demonstrated in this work is comparable or better than both designs which is impressive considering that they are larger. While the significantly-lower aperture efficiency in [104] and [61] is mainly due to non-ideal feed placement, the array elements used in both designs exhibit higher losses and have a phase range less than 360°, causing phase errors and higher SLLs.

4.5 Discussion

A 7×7 reconfigurable reflectarray antenna has been designed, simulated, fabricated and measured at X band. The reflectarray was configured to enable continuous scanning in any desired plane utilizing array elements capable of a phase range in excess of 360^o with independent biasing. A genetic algorithm capable of finding the optimal biasing voltages to obtain maximum gain in any arbitrary direction was developed. Continuous beamsteering was demonstrated from -50^o to +50^o in the H-plane while beamsteering was -40^o to +50^oin the $\phi = 45^o$ plane. Beamsteering was limited 0^o to +50^o in the E-plane due to feed blockage. A broadside gain of 15.03 dBi, a 4.41% 1-dB and a 7.81% 3-dB gain bandwidth was measured.

This reflectarray demonstrates the advantages of dual-resonant microstrip array elements in both reducing the element loss and improving the bandwidth of reconfigurable reflectarrays while providing full phase range. Future work includes studying and the fabrication sensitivities, increasing the speed of the DACs used in the biasing network and optimizing the genetic algorithm to reduce the time required to converge on the optimal biasing voltages. While the current biasing scheme works well in this case, when the size of the array increases the time required to optimize the biasing voltages will increase exponentially. In the next chapter the realization of a dual-polarization array element will be presented. Additionally, the equivalent circuit will be used to optimize the loss performance using circuit analysis.

CHAPTER 5: LOSS OPTIMIZATION AND DUAL-POLARIZATION STUDIES

In the previous chapter a reconfigurable array was designed, fabricated, and measured. In this chapter the equivalent circuit of the dual-resonance unit cell is used to evaluate loss mechanisms and to optimize the loss performance. To further extend this design, a dual-resonance dual-polarized array element is presented. Enabling two linear polarizations to operate simultaneously in the reflectarray not only adds polarization diversity but also increases the reflectarray's data capacity.

5.1 Dual Resonant Array Element Loss Optimization

Reconfigurable reflectarrays combine the advantages of traditional phased arrays and reflector antennas: spatial feeding, planar design, low fabrication costs, and high gain. Reflectarrays avoid the lossy and costly beamforming networks required to feed phased arrays and their planar design makes the fabrication much more cost effective than non-planar antennas.

Ideally, reflectarray elements should have low loss and be capable of at least 360°phase range to avoid phase errors. A dual-resonant design is required in order to achieve a phase range greater than 360°and offers shallower phase slopes which improve bandwidth performance. In this section a phase-agile dual-resonance array element is presented and an equivalent circuit is used to optimize the loss performance of the array element while maintaining a phase range greater than 360°.

5.1.1 Base Dual-Resonance Design

In Fig. 3.1, the proposed dual-resonance reflectarray element operating at *X* band is presented. The dimensions of the element are as follows: *RW = 325 μm, R_1 = 1.83 mm, R_2 = 2 mm, W_1 = 500 μm, W_2 = 1.3 mm, W_3 = 250 μm, W_4 = 2.4 mm, W_5 = 228 μm, L_1= 600 μm, L_2 = 600 μm, L_3= 400 μm, L4 = 200 μm, L_5 = 3.153 mm, Substrate thickness h = 1270 μm*. The element consists of two resonating bodies: an internal cross and an external ring element, both of which are loaded with two varactors (MACOM MA46580-1209); the varactors were chosen for their high capacitance tuning ratio and high quality (Q) factor. Rogers Duroid 6010 (ϵ_r =10.2, $tan\delta$ = 0.0023) was chosen for the substrate for its low loss tangent. The element is designed in an X-band waveguide (a = 22.86 mm, b = 10.16 mm) to simulate the effects of mutual coupling in an infinite array.

The design procedure for the dual-resonant array element is similar to the procedure presented in [108]. First, the cross and ring elements are designed separately. Both elements are designed to operate at approximately 10 GHz when simulated in isolation and have similar frequency tuning ranges when the varactors are tuned from 0.15 to 0.4 pF. Both elements are tuned such that their resonances are over-coupled for the entire frequency tuning range. The array element operates at 10.3 GHz, with a peak and average loss of 5.51 and 2.44 dB respectively, with a phase range of 428°in both cases.

5.1.2 *Loss Optimization Procedure*

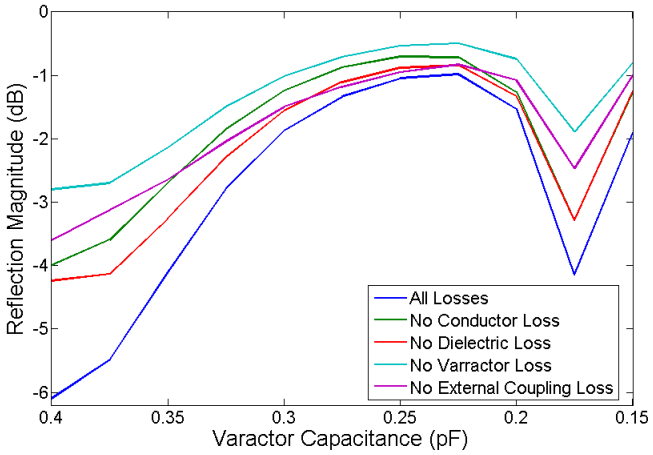

Figure 5.1: Analysis of the sources of loss in the Dual-Resonance unit cell

To aid in the optimization of the loss of the array element, an equivalent circuit was developed and is shown in Fig. 3.2. Both the ring and cross elements are represented by parallel RLC networks loaded with two varactors. The inductive π-networks $L_{RingExt.}$ and $L_{CrossExt.}$ represent the external coupling corresponding to incident waves from the waveguide into the ring and cross elements, respectively. The mutual coupling between the two elements is represented by a capacitive π-network. This equivalent circuit models the electrical performance of the unit cell in Fig. 3.1 and does not represent the physical model. First, the L, C, and C_{Var} values are found by matching the resonant frequency and frequency tuning range of the ring/cross in ANSYS High Frequency Structure Simulator (HFSS) where the ring/cross are simulated in isolation. Then the L_{Ext} and R values are set by matching the loss and phase slope at the resonant frequency. C_{Mut} is set to match the HFSS simulation results when the antenna elements are combined.

To optimize the loss of the unit cell, the sources of loss need to be considered. Fig. 5.1 demonstrates the major sources of loss. It can be seen that the varactor loss dominates the unit cell due to the intrinsic quality factor of the varactor and cannot be improved. The second major source of

loss comes from the external coupling levels but the greatest effect of the mutual coupling is on the frequency separation between the ring and cross resonances. As demonstrated in [108] this separation must be less than the frequency tuning range which is primarily limited by the tuning range of the varactors. From the equivalent circuit, R_c and R_r represent the loss due to the conductor and dielectric for the cross and ring elements, respectively. As can be seen in Fig. 5.1 these losses are a small portion of the overall loss. Copper is used for the conductor and the dielectric has a very low loss tangent. The loss and phase performance is evaluated at the center frequency 10.3 GHz as the varactors are tuned.

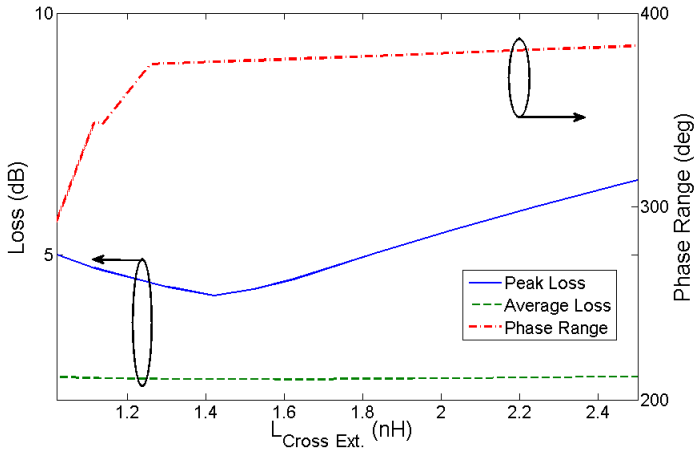

Figure 5.2: Phase range, average, and peak loss at 10.3 GHz as the cross element's external coupling is varied.

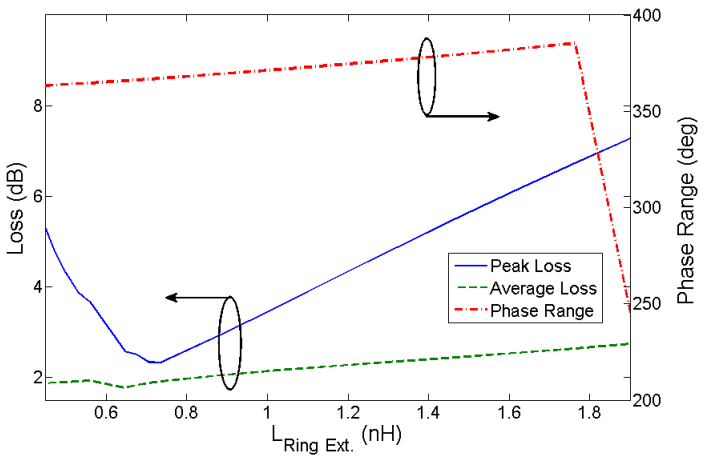

Figure 5.3: Phase range, average, and peak loss at 10.3 GHz as the ring element's external coupling is varied.

Fig. 5.2 shows that the external coupling of the cross has little effect on the average loss of the array element. However, reducing $L_{Cross\ Ext.}$ bellow 1.2 nH under-couples one of the resonances, reducing the phase range below 360°. From Fig. 5.3 it is seen that the loss performance of the array element is much more sensitive to the external-coupling of the ring than the cross element. When $L_{RingExt.}$ is increased to 1.8 nH, one of the resonances becomes under-coupled, causing a significant decrease in phase range. Tuning both $L_{RingExt.}$ and $L_{CrossExt.}$, to 0.764 and 1.83 nH, the peak and average loss are optimized and reduced to 2.29 and 1.96 dB, respectively, while maintaining a 360.6°phase range.

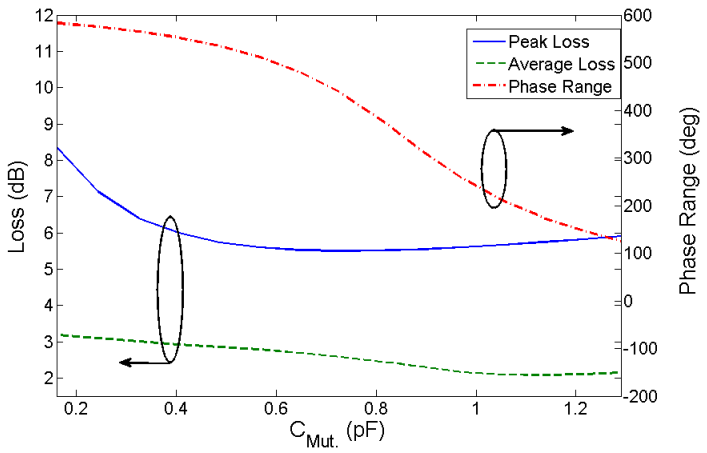

Figure 5.4: Phase range, average, and peak loss at 10.3 GHz as the mutual coupling is varied.

The design of a phase-agile dual-resonant reflectarray element was presented and an equivalent circuit was used to design an array element operating at 10.3 GHz with 360.6°phase range while reducing the peak and average loss by 3.22 and 0.48 dB, respectively. The equivalent circuit component values for both ring and cross elements provide guidelines for the design of a physical unit cell in HFSS.

5.2 Dual-Polarization In Reflectarrays

Reflectarray elements should ideally have low loss, at least 360°phase range to avoid phase errors, and a low phase slope with respect to frequency to improve antenna bandwidth. In the design presented in this section the previously presented dual resonant array element is redesigned to support two linear polarizations.

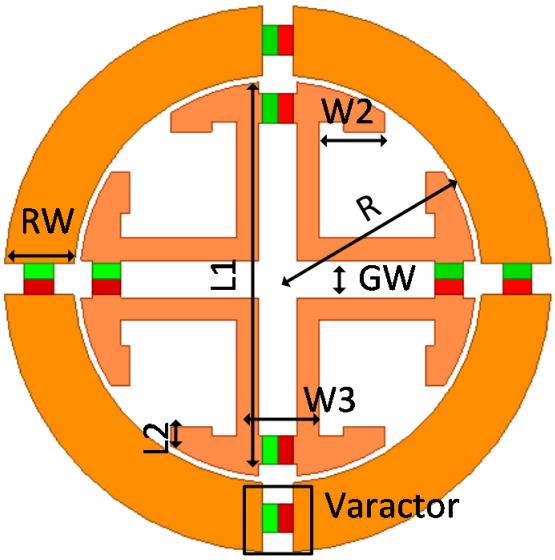

Figure 5.5: Dual polarized, dual resonant element with varactors.

In Fig. 5.5, the proposed dual-resonance reflectarray element operating at X band is presented. The element consists of two resonating bodies that are reconfigurable and symmetric to enable dual linear polarizations. The dimensions are as follows L_1 = *3.14 mm,* W_1 = *650* μ*m,* L_2 = *400* μ*m,* W_2 = *200* μ*m,* W_3 = *300* μ*m,* RW = *550* μ*m,* R = *1.63 mm.*

5.2.1 Enabling Dual-Polarization in Dual-Resonant Array Element

In the design of the proposed dual-polarized, dual-resonance reflectarray element, the interior cross element and the exterior ring element were first designed separately. Each element was designed to operate at approximately 10 GHz and support vertical and horizontal polarizations with better than 30 dB cross-polarization levels. To minimize the complexity of the biasing network, all eight varactors are biased with the same DC voltage. However, both resonating elements need to have similar frequency tuning ranges. If the resonant frequency of one of the elements changes more

than the other element with the same change in capacitance, the mutual coupling between them will change, affecting loss and phase performance.

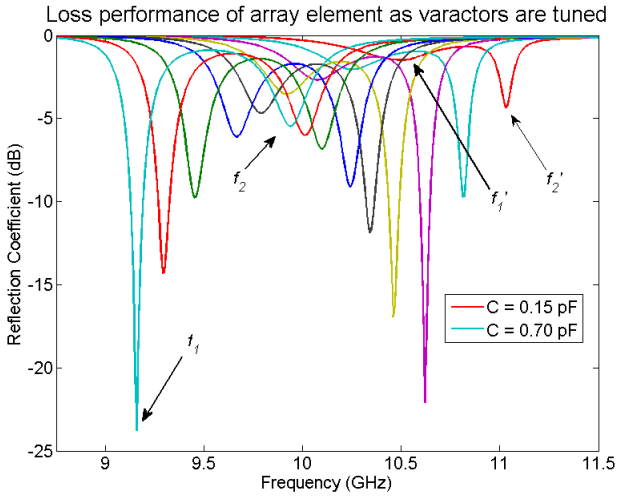

Figure 5.6: Phase range, average, and peak loss at 10.3 GHz as the mutual coupling is varied.

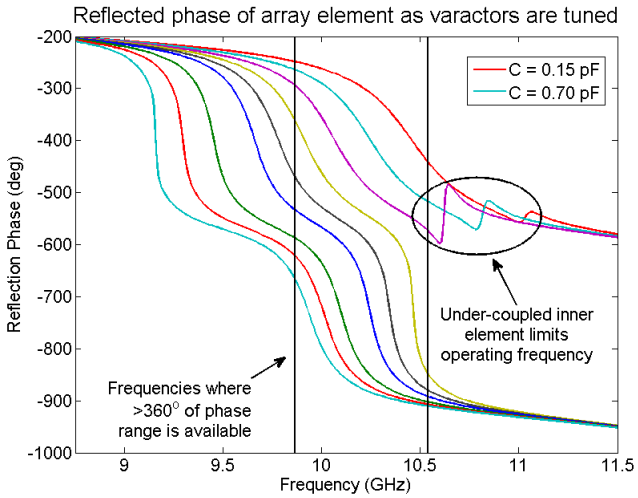

Figure 5.7: Phase range, average, and peak loss at 10.3 GHz as the mutual coupling is varied.

As discussed in [91], for dual-resonance reflectarray elements to have a phase range greater than 360°, two main conditions must be met: (1) both resonances must be over-coupled at and below the operational frequency, and (2) the frequency tuning range of the element must be greater than

or equal to the frequency separation between the two resonances. For this discussion, the initial resonant frequencies are labeled f_1 and f_2 while the tuned frequencies are labeled f_1' and f_2' as shown in Fig. 5.6. When both resonances are over-coupled, they each demonstrate a 360°phase range. If f_1' is greater than f_2, the region between f_2 and f_1' will have a phase range in excess of 360°. However, if either resonance is under-coupled, it will demonstrate an irregular phase response and the overall phase contribution of that resonance will be 0°as shown in Fig. 5.7. The under-coupled response demonstrated in Fig. 5.7 limits the frequencies in which the desired phase response can be achieved. However, because this irregular phase response is present above f_1', the frequencies between f_1' and f_2 still provide a continuous phase response greater than 360°.

Fig. 5.5 shows dimensions W2 and L2 which are used in conjunction with L_1 to adjust the physical length of the inner resonating body while maintaining its resonant frequency. By adjusting the physical length of the cross element, the mutual coupling between the two elements can be controlled, which is critical to control the loss and phase characteristics.

5.2.2 Simulation Results

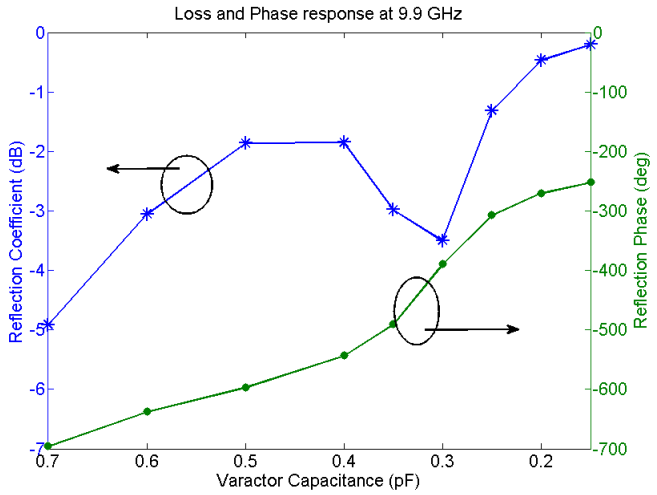

Figure 5.8: Phase range, average, and peak loss at 10.3 GHz as the mutual coupling is varied.

Fig. 5.6 shows the reflection coefficient for the proposed unit cell as the varactors are tuned from 0.7–0.15 pF. The loss and phase performance of the array element is identical for both vertical and horizontal polarizations. When the varactor capacitance loading is maximum, f_2 is more over-coupled than f1. However, as the capacitance decreases, this relationship is inverted. The element operating frequency is coincident with f2, and as such the mutual coupling is increased until the ring resonance f_1 reaches critical coupling. This is done to make the upper resonance more over-coupled, reducing the un-tuned initial loss and phase sensitivity. As the varactors are tuned, f_2 becomes more under-coupled and its loss increases; this is caused by the unequal frequency tuning range of the two resonating elements. As the capacitance is decreased, the unloaded resonant frequency of the ring begins to increase past that of the cross element, which leads to a reduction in the mutual coupling between the two resonances.

Fig. 5.8 shows the loss and phase response at the operating frequency of 9.9 GHz. The large losses at 0.7 pF and 0.3 pF are caused by the resonance of the cross and ring elements, respectively. Due to the reduction in the coupling between the elements, the loss of the ring element loss is reduced from 24 to 3.5 dB when resonant frequency of the ring element is tuned to 9.9 GHz. The peak loss of 4.9 dB arises from the cross element resonance, however the average loss across the varactor tuning range is only 2.7 dB. The phase response is smooth and linear from 0.7 pF to 0.4 pF and the phase range is 445°; since only 360°of phase tuning is required, the peak loss can be reduced to 3.5 dB if the element is operated from 0.6 to 0.15 pF.

The design of a phase-agile, dual resonant reflectarray element supporting both vertical and horizontal polarizations with better than 30 dB cross polarization levels is presented. The array element operates at 9.9 GHz and provides 445°of continuous phase range with a peak and average element loss of 4.9 dB and 2.7 dB, respectively. If the utilized phase range is reduced to 360°the peak loss can be reduced to 3.5 dB.

CHAPTER 6: SUMMARY AND FUTURE WORK

6.1 Summary

This dissertation covers the design concepts of reconfigurable reflectarrays based on dual-resonance array elements and their advantages over single resonance array elements. The array performance of the dual-resonant element and its suitability for integration into large arrays is also covered. The optimization of this design via an equivalent circuit and the extension to dual-polarized applications is also presented.

In chapter 2 a single resonant reflectarray loaded with BST is used to design fabricate, and measure a reconfigurable reflectarray at K_a band. The reflectarray demonstrated continuous beam-scanning from boresight to $+25^o$ in the E-plane. However the use of column biasing and the limited phase range increased the side-lobe levels and introduced a feed-image lobe. This design was extended to V band were and interdigitaged gap structure was used to optimize the phase range of the array element. However the phase range was still less than 360^o. A BST-integrated dual-resonant design was then introduced. The use of two resonances allowed the element to achieve a phase range greater than 360^o. However, due to the limited tuning range of BST the losses were still high.

In chapter 3 an equivalent circuit was developed to describe dual-resonant reflectarray elements, then the operational theory behind them was fully explained. Next the design procedure for a cross/ring dual resonant array element was presented. A novel biasing structure was developed to operate in the minimal space between the two resonant structures without significantly affecting their performance. The array element was designed for waveguide measurements, fabricated and measured. The array element demonstrated 375^o of phase range. Furthermore the loss and bandwidth performance of the array element was also significantly improved as compared to the

designs presented in chapter 2.

In chapter 4 the dual-resonant unit cell was redesigned for array spacing and the loss performance was further improved. The peak loss was reduced by 1.5 dB as compared to the element presented in chapter 3 while maintaining a phase range significantly larger than 360 ^{o}. Additionally, a novel genetic algorithm is developed to optimize array biasing voltages.

In chapter 5 a theoretical method of optimizing the loss performance of dual-resonant elements is presented using an equivalent circuit. After this the dual-resonant element is extended to support two linear polarizations.

6.2 Future Work

The reconfigurable reflectarray designs presented in this work have demonstrated a significant improvement on the state of the art and with further refinement could be integrated into the next generation beam-scanning antenna systems. Potential extensions of this work include improvements and modifications to the array element to increase the frequency of operation, increase the polarization diversity, and improve the array's mechanical properties.

While the dual-resonance array element has demonstrated a significant improvement in the bandwdith performance of single-resonance reconfigurable reflectarrays previously demonstrated, it is still possible to improve the performance even further. In [102] an array element utilizing three coupled resonances was demonstrated. Unfortunatley the demonstrated bandwidth was 6%, lower than the bandwdith presented in chapter 4. However, in theory this approach can be used to further increase the range of the linear phase range, improving the bandwidth further.

Varactors were used to realize the dual-resonant array at *X* band due to the limited tuning range

of BST. However, the loss of varactors increase significantly at higher frequencies and they aren't suitable for *mm*-wave applications. However, the dual-resonant operational theory presented in chapter 3 is applicable to any dual-resonant design regardless of the tuning technology utilized. Low loss MEMS capacitors are a promising candidate for higher frequency applications. Alternatively, research into manganese doped BST has reported exciting improvements into both the tuning range of BST and its losses [109]. Due to its monolithic integration, with the improvement of its tuning range and loss performance, BST would be a viable material for use in dual-resonant designs at *mm*-wave frequencies and higher.

Deployability is a desirable property for reflectarrays, especially those used in extraterrestrial applications. However, designing deployable reconfigurable reflectarrays is very difficult as the tuning elements can be fragile, requiring special care to avoid damage. Research into realizing flexible BST-integrated varactors was presented in [87]. Copper interdigitaged capacitors were integrated with BST on a silicon wafer before being bonded to a liquid crystal polymer (LCP) substrate. After this the silicon wafer was etched away realizing flexible, tunable varactors. Applying this same technique to the reflectarray design presented in chapter 4 would be challenging, as fine control over the substrate thickness is required to achieve the correct levels of mutual and external coupling. However, with this technique an entire reflectarray aperture could be rolled up, and then later deployed.

A desirable property in antenna design is polarization flexibility. Some work has been done on reconfigurable reflectarrays to support multiple linear polarizations as well as circular polarization [110], [111]. However, such works are limited and none of them offer continuous phase ranges greater than 360^o. An extension of the dual-polarization, dual-resonance design presented in chapter 5 would be to study its suitability for circular polarization. However, it will be a design challange to achieve a large axial bandwidth.

LIST OF REFERENCES

[1] G.Maral and M. Bousquet, *Satellite Communications Systems: Systems, Techniques and Technology*, 1st ed. Hoboken, NJ, USA: John Wiley & Sons, 2011.

[2] R. Dybdal, *Communication Satellite Antennas: System Architecture, Technology, and Evaluation.* 1st ed. New York, USA: McGraw-Hill, 2009.

[3] M. Skolnik, *Introduction to Radar Systems*, 1st ed. New York, USA: McGraw-Hill, 2002.

[4] R. J. Mailloux, *Phased Array Antenna Handbook*, 1st ed. Nordwood, MA, USA: Artech House, 2005.

[5] J.W. M. Baars, *The Paraboloidal Reflector Antenna in Radio Astronomy and Communication: Theory and Practice.* 1st ed. Springer Science & BusinessMedia, 2007.

[6] M. Arrebola, L. D. Haro and J. A. Encinar, "Analysis of dual-reflector antennas with a reflectaray as subreflector," *IEEE Trans. Antennas Propagation Magazine*, vol. 50, no. 6, pp. 39–51, Dec. 2008.

[7] F. Akbar and A. Mortazawi, "A frequency tunable 360° analog cmos phase shifter with an adjustable amplitude," *IEEE Transactions on Circuits and Systems II: Express Briefs*, vol. 64, no. 12, pp. 1427–1431, Dec. 2017.

[8] D. W. Kang, J. G. Kim, B. W. Min and G. M. Rebeiz, "Single and four-element ka-band transmit/receive phased-array silicon rfics with 5-bit amplitude and phase control," *IEEE Transactions on Microwave Theory and Techniques*, vol. 57, no. 12, pp. 3534–3543, Dec. 2009.

[9] J. Huang and J. A. Encinar, *Reflectarray Antennas*, 1st ed. Hoboken, NJ, USA: Wiley, 2008.

[10] D. M. Pozar, S. D. Targonski, and H. D. Syrigos, "Design of millimeter wave microstrip reflectarrays," *IEEE Trans. Antennas Propag.*, vol. 45, pp. 287–296, 1997.

[11] ——, "A shaped-beam microstrip patch reflectarray," *IEEE Trans. Antennas Propag.*, vol. 47, pp. 1167–1173, 1999.

[12] D. Berry, R. Malech, and W. Kennedy, "The reflectarray antenna," *IEEE Trans. Antennas Propag.*, vol. AP-11, no. 6, pp. 645–651, Nov. 1963.

[13] C. S. Malagisi, "Microstrip disc element reflect array," *Electronics and Aerospace Systems Convention*, pp. 186–192, 1978.

[14] D. M. Pozar and T. A. Metzler, "Analysis of a reflectarray antenna using microstrip patches of variable size," *Electronics Letters*, vol. 29, pp. 657–658, 1993.

[15] A. Kelkar, "Flaps: Conformal phased reflecting surfaces," *Radar Conference, 1991., Proceedings of the 1991 IEEE National*, pp. 58–62, 1991.

[16] N.Misran, R. Cahill, and V. Fusco, "Reflection phase response of microstrip stacked ring elements," *Electronics Letters*, vol. 38, no. 8, pp. 356–357, Apr. 2002.

[17] R. E. Munson and H. Haddad, "Microstrip reflectarray for satellite communication and rcs enhancement and reduction," *US patent 4684 952, Aug. 1987.*,

[18] J. Huang, "Bandwidth study of microstrip reflectarray and a novel phased reflectarray concept," *Antennas and Propagation Society International Symposium*, vol. 1, pp. 582–585, Jun. 1995.

[19] J. Huang and R. Pogorzelski, "A ka-band microstrip reflectarray with elements having variable rotation angles," *IEEE Trans. Antennas Propag.*, vol. 46, no. 5, pp. 650–656, May 1998.

[20] J. Huang and J. A. Encinar, *Introduction to reflectarray antennas*, 1st ed. Hoboken, NJ, USA: Wiley, 2008.

[21] E. Carrasco, J. A. Encinar, and M. Barba, "Bandwidth improvement in large reflectarrays by using true-time delay," *IEEE Trans. Antennas Propag.*, vol. 56, no. 8, pp. 2496–2503, Aug. 2008.

[22] O. Bayraktar, O. A. Civi and T. Akin, "Beam switching reflectarray monolithically integrated with rf mems switches," *IEEE Trans. Antennas Propag.*, vol. 60, no. 2, pp. 854–862, Feb. 2012.

[23] B. Wu, A. Sutinjo, M. E. Potter and M. Okoniewski, "On the selection of the number of bits to control a dynamic digital mems reflectarray," *IEEE Antennas and Wireless Propagation Letters*, vol. 7, pp. 183–186, 2008.

[24] M. Y. Ismail, W. Hu, R. Cahill, V. F. Fusco, H. S. Gamble, D. Linton, et al., "Phase agile reflectarray cells based on liquid crystals," *Microwaves, Antennas & Propagation, IET*, vol. 1, pp. 809–814, 2007.

[25] L. Boccia, G. Amendola, and G. D. Massa, "Performance improvement for a varactor-loaded reflectarray element," *IEEE Trans. Antennas Propag.*, vol. 58, no. 2, pp. 585–589, Feb. 2010.

[26] O. Vendik and M. Parnes, "A phase shifter with one tunable component for a reflectarray antenna," *Antennas and Propagation Magazine*, vol. 50, pp. 53–65, 2008.

[27] J. A. Encinar and J. A. Zornoza, "Three-layer printed reflectarrays for contoured beam space applications," *IEEE Trans. Antennas Propag.*, vol. 52, no. 5, pp. 1138–1148, 2004.

[28] J. A. Zornoza, R. Leberer, J. A. Encinar, and W. Menzel, "Folded multilayer microstrip reflectarray with shaped pattern," *IEEE Trans. Antennas Propag.*, vol. 54, no. 2, pp. 510–518, 2006.

[29] J. A. Encinar, L. Sh, Datashvili, J. A. Zornoza, M. Arrebola, M. Sierra-Castaner, J. L. Besada-Sanmartin, H. Baier, and H. Legay, "Dual-polarization dual-coverage reflectarray for space applications," *IEEE Trans. Antennas Propag.*, vol. 54, no. 10, pp. 2827–2837, Oct. 2006.

[30] J. Encinar, L. Datashvili, H. Baier, M. Arrebola, M. Sierra-Castaner, J. Besada, H. Legay, and G. Toso, "Breadboard of a three-layer printed reflectarray for dual polarisation and dual coverage," *Proc. 28th ESA Antenna Workshop on Space Antenna Systems and Techniques, Noordwijk, The Netherlands,*, vol. 31, pp. 443–448, 2005.

[31] M.Mussetta, P.Pirinoli, R.E.Zich and M.Orefice, "Design of printed microstrip reflectarrays reducing the groundplane reflection," *Proceedings URSI General Assembly, New Delhi, India*, 2005.

[32] R.El-Hani and J.Laurin, "Phase analysis for off-specular reflectarray antennas," *IEEE International Antenna and Propagation Symposium Digest*, pp. 380–383, 2011.

[33] ——, "Specular reflection analysis for off-specular reflectarray antennas," *IEEE Transactions on Antenna and propagation*, vol. 61, no. 7, pp. 3582–3588, Jul. 2013.

[34] S.D.Targonsk and D.M.Pozar, "Minimization of beam squint in microstrip reflectarrays using an offset feed," *IEEE International Symposium on Antenna and Propagation*, vol. 2, pp. 1326–1329, Jul. 1996.

[35] K. K. Karnati, Y. Yusuf, S. Ebadi, and X. Gong, "Q factor analysis of reflectarray elements investigating the effects from angle of incidence using floquet modes," *IEEE Trans. Antennas Propag.*, vol. 61, no. 10, pp. 5017–5028, Oct. 2014.

[36] A. Yu, F. Yang, A. Z. Elsherbeni, J. Huang, and Y. Rahmat-Samii, "Aperture efficiency analysis of reflectarray antennas," *Microw. Opt. Technol. Lett*, vol. 52, pp. 364–372, 2010.

[37] H. Salti, T. Selmi and R. Gillard, "Toward a statistical understanding of reflectarrays' bandwidth," *2015 Fifth International Conference on Digital Information and Communication Technology and its Applications (DICTAP), Beirut, 2015, pp. 195-197.*,

[38] K. H. Sayidmarie and M. E. Bialkowski, "Investigation into bandwidth limitations of microstrip reflectarrays," *2008 3rd International Conference on Information and Communication Technologies: From Theory to Applications, Damascus, 2008, pp. 1-6.*,

[39] H. Hasani, M. Kamyab, and A.Mirkamali, "Broadband reflectarray antenna incorporating disk elements with attached phase-delay lines," *Antennas and Wireless Propagation Letters*, vol. 9, pp. 156–158, 2010.

[40] E. Carrasco, M. Barba, and J. A. Encinar, "Reflectarray element based on aperture-coupled patches with slots and lines of variable length," *IEEE Transaction on Antennas and Propagation*, vol. 55, pp. 820–825, Mar. 2007.

[41] K. K Karnati, Y. Yusuf, S. Ebadi and X. Gong, "Theoretical analysis on reflection properties of reflectarray unit cells using quality factors," *IEEE Trans. Antennas Propag.*, vol. 61, no. 1, pp. 201–210, Jan. 2013.

[42] J. A. Encinar, "Design of two-layer printed reflectarray using patches of variable size," *IEEE Transaction on Antennas and Propagation*, vol. 49, pp. 1403–1410, Oct. 2001.

[43] J. A. Encinar and J. A. Zornoza, "Broadband design of three-layer printed reflectarrays," *IEEE Transaction on Antennas and Propagation*, vol. 51, pp. 1662–1664, 2003.

[44] M. E. Bialkowski and K. H. Sayidmarie, "Investigations into phase characteristics of a single-layer reflectarray employing patch or ring elements of variable size," *IEEE Transaction on Antennas and Propagation*, vol. 56, pp. 3366–3372, 2008.

[45] M. R. Chaharmir, J. Shaker, and H. Legay, "Broadband design of a single layer large reflectarray using multi cross loop elements," *IEEE Transaction on Antennas and Propagation*, vol. 57, pp. 3363–3366, 2009.

[46] Q. Y. Li, Y. C. Jiao and G. Zhao, "A novel microstrip rectangular-patch/ring- combination reflectarray element and its application," *IEEE Antennas and Wireless Propagation Letters*, vol. 8, pp. 1119–1122, 2009.

[47] H. Yang et al., "A study of phase quantization effects for reconfigurable reflectarray antennas," *IEEE Antennas and Wireless Propagation Letters*, vol. 16, pp. 302–305, 2017.

[48] H. Legay, B. Pinte, M. Charrier, A. Ziaei, E. Girard, and R. Gillard, "A steerable reflectarray antenna with mems controls," *IEEE International Conference on Phased Array Systems and Technology*, pp. 494–499, 2003.

[49] S. V. Hum, G. McFeetors, and M. Okoniewski, "Integrated mems reflectarray elements," *First European Conference on Antennas and Propagation*, pp. 1–6, 2006.

[50] H. Rajagopalan, Y. Rahmat-Samii, and W. A. Imbriale, "Rf mems actuated reconfigurable reflectarray patch-slot element," *IEEE Trans. Antennas Propag.*, vol. 56, no. 12, pp. 3689–3699, Dec. 2008.

[51] P. V. Rainey, M. Bain, R. Jackson, S. N. Mitchell, D. Linton, V. F. Fusco, et al., "Design, manufacture and performance of monolithic pin diodes for beam steered reflectarray," *The Second European Conference on Antennas and Propagation*, pp. 1–5, 2007.

[52] E. Carrasco, M. Barba and J. A. Encinar, "X-band reflectarray antenna with switching-beam using pin diodes and gathered elements," *IEEE Trans. Antennas Propag.*, vol. 60, no. 12, pp. 5700–5708, Dec. 2012.

[53] H. Wenfei, R. Cahill, J. A. Encinar, R. Dickie, H. Gamble, V. Fusco, et al., "Design and measurement of reconfigurable millimeter wave reflectarray cells with nematic liquid crystal," *IEEE Trans. on Antennas Propag.*, vol. 56, pp. 3112–3117, Sep. 2008.

[54] A. Kanareykin, E. Nenasheva, S. Karmanenko, A. Dedyk, and V. Yakovlev, "Low-loss ferroelectric for accelerator applications," *Proc. of 2005 Particle Accelerator Conference*, pp. 4305–4307, May 2005.

[55] P. Scheele, A. Giere, Y. Zheng, F. Goelden, and R. Jakoby, "Modeling and applications of ferroelectric-thick film devices with resistive electrodes for linearity improvement and tuning-voltage reduction," *IEEE Trans. Microw. Theory Tech.*, vol. 55, pp. 383–390, Feb. 2007.

[56] Y. Zheng, A. Hristov, A. Giere, and R. Jakoby, "Suppression of harmonic radiation of tunable planar inverted-f antenna by ferroelectric varactor loading," *IEEE MTT-S Int. Micro. Symp. Dig.*, pp. 959–962, 2008.

[57] B. Acikel, "High performance barium strontium titanate varactor technology for low cost circuit applications," *University of California, Santa Barbara*, 2002.

[58] E. Carrasco and J. Perruisseau-Carrier, "Reflectarray antenna at terahertz using graphene," *Antennas and Wireless Propagation Letters*, vol. 12, pp. 253–256, 2013.

[59] S. A. Long and G. H. Huff, "A fluidic loading mechanism for phase reconfigurable reflectarray elements," *IEEE Antennas and Propag. Lett.*, vol. 10, pp. 876–879, 2011.

[60] M. Hajian, B. J. Kuijpers, and L. P. Ligthart, "Reflectarray design using capacitive loading on a slotted patch," *First European Conference on Antennas and Propagation*, pp. 1–7, 2006.

[61] S. V. Hum, M. Okoniewski, and R. J. Davies, "Modeling and design of electronically tunable reflectarrays," *IEEE Trans. Antennas Propag.*, vol. 55, no. 8, pp. 2200–2210, Aug. 2007.

[62] X. Yang et al., "A broadband high-efficiency reconfigurable reflectarray antenna using mechanically rotational elements," *IEEE Trans. Antennas Propag.*, vol. 65, no. 8, pp. 3959–3966, Aug. 2017.

[63] ——, "A mechanically reconfigurable reflectarray with slotted patches of tunable height," *IEEE Antennas and Wireless Propag. Lett.*, vol. 17, no. 4, pp. 555–558, Apr. 2018.

[64] G. Perez-Palomino, J. A. Encinar, M. Barba and E. Carrasco, "Design and evaluation of multi-resonant unit cells based on liquid crystals for reconfigurable reflectarrays," *IET Microwaves, Antennas & Propagation*, vol. 6, no. 3, pp. 348–354, Feb. 2012.

[65] K. K. Karnati, Y. Shen, M. Trampler, S. Ebadi, P. Wahid, and X. Gong, "A bst-integrated capacitively-loaded patch for ka- and x-band beamsteerable reflectarray antennas in satellite communications," *IEEE Trans. Antennas Propag.*, vol. 63, no. 4, pp. 1324–1333, Jan. 2015.

[66] Kumar, K. Ashok, Supriya, and G. Venkataraman, "Integration issues of barium strontium titanate thin film for tunable microwave applications," *Ceramic Integration and Joining Technologies From Macro to Nanoscale*, 2011.

[67] V. Gurumurthy, "Barium strontium titanate films for tunable microwave and acoustic wave applications. diss. university of south florida," 2007.

[68] APC International Ltd, "Peizoelectric ceramics: Principles and applications,"

[69] R. R. Romanofsky, "Advances in scanning reflectarray antennas based on ferroelectric thin-film phase shifters for deep-space communications," *Proceedings of the IEEE*, vol. 95, pp. 1968–1975, 2007.

[70] G. Perez-Palomino, P. Baine, R. Dickie, M. Bain, J. A. Encinar, R. Cahill, M. Barba, and G. Toso, "Design and experimental validation of liquid crystal-based reconfigurable reflectarray elements with improved bandwidth in f-band," *IEEE Trans. Antennas Propag.*, vol. 61, no. 4, pp. 1704–1713, Apr. 2013.

[71] R. A. Nabeel, "High-optical-isolation low-loss moderate-switching-speed nematic liquid-crystal optical switch," *Opt. Lett.*, vol. 19, pp. 1780–1782, 1994.

[72] K. K. Karnati, M. E. Trampler and X. Gong, "A monolithically bst-integrated ka -band beamsteerable reflectarray antenna," *IEEE Trans. Antennas Propag.*, vol. 65, no. 1, pp. 159–166, Jan. 2017.

[73] Li, J.F.; Chen, Q.; Yuan, Q.W.; Sawaya, K., "Reflectarray element using interdigital gap loading structure," *Electronics Letters*, vol. 47, no. 2, pp. 83–85, Jan. 2011.

[74] Karnati, K.K.; Yusuf, Y.; Ebadi, S.; Xun Gong, "Reflection coefficient analysis of a tem-excited reflectarray unit cell using quality factors," *Antennas and Propagation Society International Symposium (APSURSI)*, pp. 1–2, Jul. 2012.

[75] J. H. Yoon, Y. J. Yoon, W. s. Lee and J. h. So, "W-band microstrip reflectarray with double-cross element for bandwidth improvement," *Global Symposium on Millimeter-Waves (GSMM)*, pp. 1–3, 2015.

[76] M. E. Trampler, K. K. Karnati, and X. Gong, "Tunable ring-loaded patch element for beam-steerable reflectarray applications," *Proc. IEEE Int. Symp. Antennas Propag.*, pp. 1027–1028, Jul. 2014.

[77] S. V. Hum, M. Okoniewski, and R. J. Davies, "Modeling and design of electronically tunable reflectarrays," *IEEE Trans. Antennas Propag.*, vol. 55, no. 8, pp. 2200–2210, Aug. 2007.

[78] M. Riel and J. Laurin, "Design of an electronically beam scanning reflectarray using aperture-coupled elements," *IEEE Trans. Antennas Propag.*, vol. 55, no. 5, pp. 1260–1266, May 2007.

[79] H. Yang et al., "A 1-bit 10 x 10 reconfigurable reflectarray antenna: Design, optimization, and experiment," *IEEE Trans. Antennas Propag.*, vol. 64, no. 6, pp. 2246–2254, Jun. 2016.

[80] G. M. Rebeiz, *RF MEMS: Theory, Design, and Technology*, 1st ed. Hoboken, NJ, USA: Wiley, 2004.

[81] X. B. Li, W. B. Lu, J. Wang, B. H. Huang and H. Chen, "Dual-beam scanning using graphene-based reflectarray," *2015 Asia-Pacific Microwave Conference (APMC)*, pp. 1–3, 2015.

[82] K. K. Karnati, Y. Shen, M. E. Trampler, S. Ebadi, P. F. Wahid and X. Gong, "A bst-integrated capacitively loaded patch for ka- and x-band beamsteerable reflectarray antennas in satellite communications," *IEEE Trans. Antennas Propag.*, vol. 63, no. 4, pp. 1324–1333, Apr. 2015.

[83] P. Nayeri, F. Yang and A. Z. Elsherbeni, "Beam-scanning reflectarray antennas: A technical overview and state of the art.," *IEEE Antennas and Propagation Magazine*, vol. 57, no. 4, pp. 32–47, Aug. 2015.

[84] T. Debogovic and J. Perruisseau-Carrier, "Low loss mems-reconfigurable 1-bit reflectarray cell with dual-linear polarization," *IEEE Trans. Antennas Propag.*, vol. 62, no. 10, pp. 5055–5060, Oct. 2014.

[85] Y. Yin et al., "Research on terahertz reflectarray based on graphene surface and pet substrate," *2017 10th UK-Europe-China Workshop on Millimetre Waves and Terahertz Technologies (UCMMT)*, pp. 1–3, 2017.

[86] S. V. Hum and J. Perruisseau-Carrier, "Reconfigurable reflectarrays and array lenses for dynamic antenna beam control: A review," *IEEE Trans. Antennas Propag.*, vol. 62, no. 1, pp. 183–198, Jan. 2014.

[87] Ya Shen, S. Ebadi, P. Wahid and Xun Gong, "Tunable and flexible barium strontium titanate (bst) varactors on liquid crystal polymer (lcp) substrates," *2012 IEEE/MTT-S International Microwave Symposium Digest*, pp. 1–3, 2012.

[88] Perruisseau-Carrier, M. Tamagnone, J. S. Gomez-Diaz, and E. Carrasco, "Graphene antennas: Can integration and reconfigurability compensate for the loss?" *Proc. IEEE Eur. Conf. Microw.*, pp. 369–372, Oct. 2013.

[89] W. Hu et al., "Electronically reconfigurable monopulse reflectarray antenna with liquid crystal substrate," *The Second European Conference on Antennas and Propagation, EuCAP 2007, Edinburgh,2007*, no. 1, pp. 1–6,

[90] N. Misran, R. Cahill and V. F. Fusco, "Design optimisation of ring elements for broadband reflectarray antennas," *IEE Proceedings - Microwaves, Antennas and Propagation*, vol. 150, no. 6, pp. 440–444, 2009.

[91] M. E. Trampler and X. Gong, "Phase agile bst-loaded dual resonance reflectarray design at ka-band," *2017 IEEE International Symposium on Antennas and Propagation & USNC/URSI National Radio Science Meeting, San Diego, CA, 2017, pp. 911-912.*,

[92] C. Liu and S. V. Hum, "An electronically tunable single-layer reflectarray antenna element with improved bandwidth," *IEEE Antennas and Wireless Propagation Letters*, vol. 9, pp. 1241–1244, 2010.

[93] W. Hu et al., "Phase control of reflectarray patches using liquid crystal substrate," *2006 First European Conference on Antennas and Propagation, Nice, 2006, pp. 1-6.*,

[94] H. Rajagopalan and Y. Rahmat-Samii, "On the reflection characteristics of a reflectarray element with low-loss and high-loss substrates," *IEEE Antennas and Propagation Magazine*, vol. 52, no. 4, pp. 73–89, 2010.

[95] M. Trampler and X. Gong, "Dual polarization, dual resonant reflectarray element for beam-steering applications at x band," *Int. Symposium on Antennas and Propagation, Boston, Massachusetts, July 8-13, 2018.*,

[96] D. M. Pozar, "Bandwidth of reflectarrays," *Electron. Lett.*, vol. 39, no. 21, pp. 1490–1491, Oct. 2013.

[97] S. M. A. M. H. Abadi, K. Ghaemi, and N. Behdad, "Ultrawideband, true-time-delay reflectarray antennas using ground-planebacked, miniaturized-element frequency selective surfaces," *IEEE Trans. Antennas Propag.*, vol. 63, no. 2, pp. 534–542, Feb. 2015.

[98] P. Nayeri, F. Yang and A. Z. Elsherbeni, "Broadband reflectarray antennas using double-layer subwavelength patch elements," *IEEE Antennas and Wireless Propag. Lett.*, vol. 9, pp. 1139–1142, Nov. 2010.

[99] R. E. Hodges, N. Chahat, D. J. Hoppe and J. D. Vacchione, "A deployable high-gain antenna bound for mars: Developing a new folded-panel reflectarray for the first cubesat mission to mars," *IEEE Antennas and Propagation Mag.*, vol. 59, no. 2, pp. 39–49, Apr. 2017.

[100] S. R. Rengarajan, "Scanning and defocusing characteristics of microstrip reflectarrays," *IEEE Antennas and Wireless Propag. Lett.*, vol. 9, pp. 163–166, Mar. 2010.

[101] E. Carrasco, M. Tamagnone, and J. Perruisseau-Carrier, "Tunable graphene-based reflectarray element for reconfigurable beams," *Proc. 7th Eur. Conf. Antennas Propag. (EuCAP'13), pp. 1779–1782, April 2013*,

[102] G. Perez-Palomino et al., "Design and demonstration of an electronically scanned reflectarray antenna at 100 ghz using multiresonant cells based on liquid crystals," *IEEE Trans. Antennas Propag.*, vol. 63, no. 8, pp. 3722–3727, Aug. 2015.

[103] S. Bildik, S. Dieter, C. Fritzsch, W. Menzel and R. Jakoby, "Reconfigurable folded reflectarray antenna based upon liquid crystal technology," *IEEE Trans. Antennas Propag.*, vol. 63, no. 1, pp. 122–132, Jan. 2015.

[104] F. Venneri, S. Costanzo and G. Di Massa, "Design and validation of a reconfigurable single varactor-tuned reflectarray," *IEEE Trans. Antennas Propag.*, vol. 61, no. 2, pp. 635–645, Feb. 2013.

[105] M. E. Trampler, X. Gong, "Phase-agile dual-resonance single linearly-polarized antenna element for reconfigurable reflectarray applications," *IEEE Trans. Antennas Propag.*, vol. 67, no. 6, pp. 3752–3761, Jun. 2019.

[106] Payam Nayeri; Fan Yang; Atef Z. Elsherbeni, "System design and aperture efficiency analysis," *Reflectarray Antennas: Theory, Designs, and Applications*, 2018.

[107] N. Hirai et al., "Dielectric properties of biodegradable polylactic acid and starch ester," *Proc. IEEE Int. Conf. Solid Dielectrics (ICSD), vol. 1, pp. 87–89, Jul. 2004*,

[108] M. Trampler and X. Gong, "Dual polarization, dual resonant reflectarray element for beam-steering applications at x band," *Int. Symposium on Antennas and Propagation, Boston, Massachusetts, July 8-13, 2018.*,

[109] K. Nadaud, C. Borderon, S. Pavy, and H. W. Gundel, "Realization and characterization of manganese doped bst thin films for reflectarray applications," *IEEE Int. Symp. Applications of Ferroelectric and Workshop on the Piezoresponse Force Microscopy (ISAF/PFM)*, pp. 145–148, Jul. 2013.

[110] C. Guclu, J. Perruisseau-Carrier, and O. Civi, "Proof of concept of a dual-band circularly-polarized rf mems beam-switching reflectarray," *IEEE Trans. Antennas Propag.*, vol. 60, no. 11, pp. 5451–5455, Nov. 2012.

[111] J. Perruisseau-Carrier, "Dual-polarized and polarization-flexible reflective cells with dynamic phase contro," *IEEE Transactions on Antennas and Propagation*, vol. 58, no. 5, pp. 1494–1502, May 2010.